CHAPTER

6

EXPERIMENTAL ^{1}H NMR METHODS

Because of the high natural abundance and large magnetogyric ratio of the ^{1}H nucleus, protein NMR studies traditionally have utilized predominantly homonuclear ^{1}H spectroscopic techniques. This chapter describes the homonuclear ^{1}H NMR experiments required to obtain complete ^{1}H resonance assignments and to ascertain structural and dynamical features of proteins with molecular masses of up to 10 to 12 kDa, provided that the proteins are well-behaved in solution and display reasonable chemical shift dispersion (as a consequence of differences in chemical shift dispersion, relatively larger β-sheet proteins, compared to α-helical proteins, are amenable to investigation). Hundreds of 2D and 3D ^{1}H NMR experiments have been described in the literature; however, many of these are not generally applicable, or have been superseded by superior techniques. This chapter provides a concise compendium of useful NMR experiments from which resonance assignments and subsequent structural and dynamical investigations can be performed by using a minimum of spectrometer time. Heteronuclear NMR spectroscopy, utilizing ^{13}C and ^{15}N spins as well as ^{1}H spins is described in Chapters 7 and 9.

Throughout this chapter, phase-sensitive, rather than magnitude-mode, spectra have been presented, because resolution of the resonances is superior and analysis of the cross-peak fine structure is facilitated.

Sections of correlation spectra with antiphase lineshapes are shown with multiple contours for the positive peak components, and a single contour for negative components. Generally, spectra with in-phase lineshapes are depicted with only positive or negative levels displayed; spectra in which both sets of peaks are displayed are discussed in the appropriate figure captions.

6.1 Assessment of the 1D ^{1}H Spectrum

Although the majority of spectroscopic analyses will depend on 2D and 3D NMR spectroscopy, important preparatory work can be performed by using 1D ^{1}H NMR spectroscopy. To begin, a 1D ^{1}H NMR spectrum of the protein in H_2O solution (containing 5–10% D_2O as a lock reference) is acquired using the Hahn echo (Section 3.6.4.2), excitation sculpting (Section 3.5.3), jump–return (Section 3.5.2), or other one-dimensional NMR experiments.

The first spectral feature of interest is the signal-to-noise (S/N) ratio. This parameter obviously depends upon the concentration of protein, but also is affected by the linewidth and multiplet structure of the resonance signals. If more than the most basic correlation experiments (i.e., COSY for homonuclear spectroscopy, HSQC/HMQC for heteronuclear spectroscopy) are to be feasible, then the 1D ^{1}H spectrum must contain a reasonable amount of signal after co-adding 16 or 32 transients. The standard sample used for ^{1}H experiments in this text is a 2 m*M* ubiquitin solution (see Preface). The ^{1}H NMR spectrum shown in Fig. 6.1a was collected with 32 transients and has S/N ratios of 243, for a resolved upfield-shifted methyl group, and 46, for a resolved downfield-shifted amide group. S/N ratios are measured as the resonance peak height divided by the root-mean-square baseline noise in the spectrum. Rapid rotation narrows the resonance linewidths for methyl groups (relative to $^1H^{\alpha}$ resonances); in contrast, amide proton linewidths are broadened by amide proton solvent exchange, scalar relaxation to the ^{14}N nucleus, and partially resolved scalar coupling to the $^1H^{\alpha}$ spin. In addition, the intensity of the amide resonance is reduced by the fraction of D_2O present in the sample. Thus, the value of the S/N ratio for the amide is less than one-third of the value for the methyl group.

The second parameter of interest is the resonance linewidth, given by the full-width at half-height ($\Delta\nu_{FWHH}$) or the transverse relaxation rate constant (R_2). Beyond the contribution to the S/N ratio, $\Delta\nu_{FWHH}$ and R_2 affect the efficacy of coherence transfer by evolution under the scalar

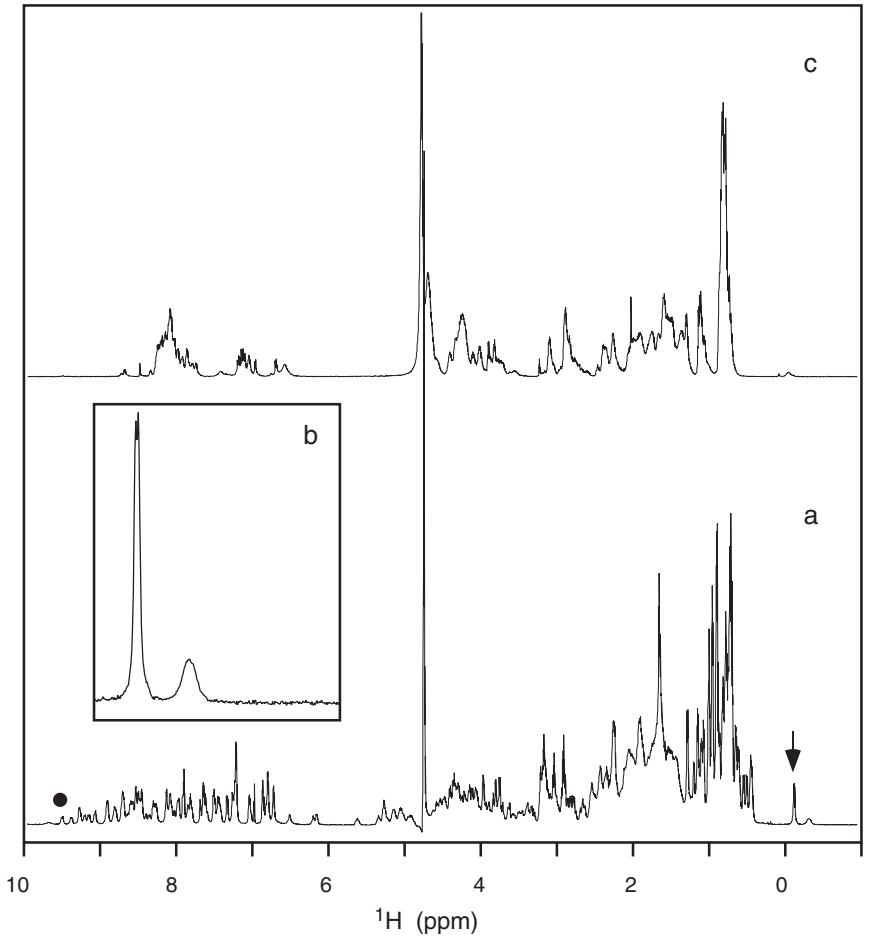

Figure 6.1 (a) 1D spectrum of a 2 m*M* ubiquitin sample in H_2O acquired at 500 MHz and 27°C. The 90° acquisition pulse was preceded by 1.5 s of solvent presaturation and followed by a Hahn echo (Section 3.6.4.2). The spectrum is the result of 32 transients collected with a spectral width of 12.5 kHz and a 30-kHz filter width. The region around the upfield-shifted methyl group of Leu50 (arrow) is enlarged in the inset (b). The RMS noise at the edges of the spectrum is 0.0023 (arbitrary units), while the Leu50 methyl ^{1}H signal has a height of 0.56, giving an S/N ratio of 243. An S/N ratio of 46 is obtained for the resolved downfield-shifted $^1H^N$ resonance of Ile13 (filled circle). (c) The 1D spectrum of a 2 m*M* ubiquitin sample in 8 *M* urea/H_2O solution. The reduced chemical shift dispersion is characteristic of unfolded or denatured proteins.

coupling Hamiltonian. Furthermore, in indirectly detected ^{1}H dimensions of multidimensional NMR experiments, the transverse relaxation rate constant, R_2, of the coherence of interest is important in deciding an appropriate value for $t_{1\max}$. Extending t_1 beyond $2/R_2$ or $3/R_2$ is undesirable because the later increments of t_1 only contribute noise to the processed spectrum. Values of $\Delta\nu_{FWHH}$ and R_2 are related to the rotational correlation time of the protein, which in turn depends on the solution viscosity and temperature (Section 1.4). Larger proteins have larger linewidths and lower apparent S/N ratios even at similar concentrations. Aggregation causes line broadening, and, in some unfortunate cases, proteins may aggregate to such an extent that no peaks are observed in the 1D ^{1}H spectrum (the linewidth becomes so large that the peaks merge into the baseline), even though other methods of detection indicate that the actual protein concentration in solution is in the millimolar range. The phenomenological ^{1}H single-quantum relaxation rate constant, $R_2^* = R_2 + R_{inhom}$, in which R_{inhom} represents the contribution from magnetic field inhomogeneity, can be estimated from the full-width-at-half-height linewidth ($\Delta\nu_{FWHH}$) of resolved peaks as $R_2^* \approx (\pi\Delta\nu_{FWHH})$. For ubiquitin ($M_r = 8565$), the full-width-at-half-height linewidth ($\Delta\nu_{FWHH}$) of a resolved upfield methyl group and downfield amide proton are 6.4 and 8.6 Hz, respectively, at 300 K. Linewidths were obtained by curve-fitting to an in-phase Lorentzian doublet because the observed lineshape of both resonances has a contribution from a partially resolved scalar coupling. Transverse relaxation rate constants for the amide ^{1}H spins also can be estimated from the one-dimensional jump–return Hahn echo experiment (Section 3.6.2.6).

The third spectral feature of interest is the resonance dispersion in the 1D spectrum. The degree of dispersion indicates the integrity of the protein under the particular experimental conditions chosen. Denatured proteins have chemical shifts close to those found in short linear peptides (the so-called random coil shifts; Section 1.5), whereas folded proteins will exhibit a range of chemical shifts due to the anisotropic magnetic fields of proximal aromatic or carbonyl groups. Thus, if very little chemical shift dispersion is observed, then the protein may be unfolded, or may have very little stable structure. As an example, a spectrum of ubiquitin denatured in 8 *M* urea is shown in Fig. 6.1c. The key resonances to examine arise from the amide protons (random coil shifts, 8.5–8.0 ppm), α-protons (random coil shifts, 4.4–4.1 ppm), and methyl groups of valine, isoleucine, and leucine (random coil shifts, 1.1–0.8 ppm). Examination of the chemical shift dispersion also indicates the ease with which resonance assignments can be made by the

sequential spin system method described in Section 9.1.1. If overlap in the important $^1H^N$ region is significant (and to a lesser extent in the $^1H^\alpha$ and methyl ^1H regions), sequential assignments will be hard won, and the number of NOEs that can be assigned unambiguously will be low (leading to poor structural definition). Schemes have been proposed that use the observed dependence of $^1H^N$ and $^1H^\alpha$ chemical shift on secondary structure to estimate the number of residues in different types of regular secondary structure (*1*, *2*).

Finally, the purity of the sample can be gauged from the 1D spectrum. Low molecular weight impurities are apparent as sharp peaks amid the broader envelope of protein resonances. Of course, a pure protein sample also can exhibit linewidth variations due to differential internal mobility, particularly at side chain termini, or in flexible loop regions, so sharp lines are not necessarily proof of contamination. Observation of variations in the relative peak heights of resolved resonances may indicate inhomogeneous protein preparations, although such information usually is better gauged from COSY (Section 6.2.1) or HSQC/HMQC spectra (Section 7.1.1). Low molecular weight impurities also can be identified from a TOCSY experiment (Section 6.5) recorded with a long (200-ms) mixing time because protein resonances are attenuated preferentially by relaxation.

If any of the basic attributes of the 1D ^1H NMR spectrum (S/N ratio, linewidth, chemical shift dispersion) are less than ideal, the 1D spectrum provides an efficient way to probe the dependence of these aspects on sample conditions, including concentration, temperature, pH, and ionic strength. As a word of caution, care should be taken when performing such studies, as extremes of temperature and pH may lead to irreversible denaturation or loss of protein integrity. Furthermore, unless spectra are recorded without presaturation of the solvent resonance (Section 3.5.3), spectra may suffer from a loss of amide proton signal intensity from saturation transfer via exchange with solvent at elevated temperature or pH.

6.2 COSY-Type Experiments

COSY and related experiments are based on coherence transfer through evolution under the scalar coupling Hamiltonian during pulse-interrupted free-precession pulse sequence elements. The basic aspects of coherence transfer are described in Section 4.2.2.1. The following sections describe in detail theoretical and practical aspects of these experiments.

6.2.1 COSY

COSY, or correlated spectroscopy, was the first 2D NMR experiment to be devised (*3*, *4*), and remains useful for NMR studies of small proteins. COSY cross-peaks arise through coherence transfer between coupled spins; in practice for protein studies, this limits transfer to protons separated by two or three bonds. The pulse sequence simply consists of two pulses separated by an incrementable delay (t_1). The recycle delay precedes the first pulse, and the acquisition period (t_2) follows the second pulse, as shown in Fig. 6.2. The basic phase cycle consists of eight steps: the phases of both pulses and the receiver are cycled together using the CYCLOPS scheme, and the phases of the first pulse and receiver are inverted to reduce axial peak intensity.

6.2.1.1 Product Operator Analysis Most of the homonuclear NMR experiments discussed in this chapter begin with a 90°_x–t_1–90°_x pulse sequence element (multiple-quantum experiments are the principal exceptions). In the following discussion, spins will be designated I_k for $k = 1, 2, \ldots, K$ (for a K-spin system). The chemical shift of the kth spin is Ω_k, and the scalar coupling constant between the jth and kth spins is J_{jk}

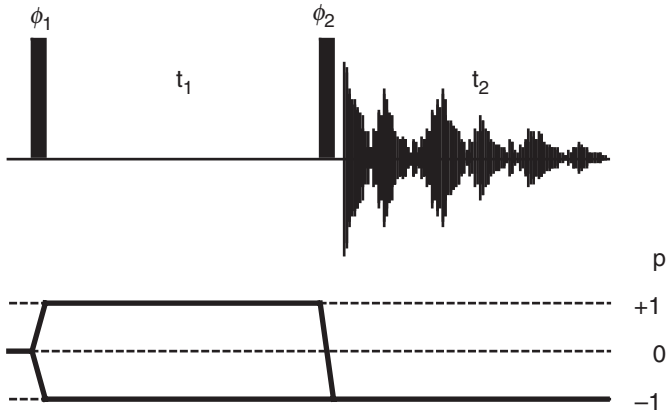

FIGURE 6.2 Pulse sequence and coherence level diagram for the COSY experiment. Narrow bars represent 90° pulses. The basic phase cycle is $\phi_1 = x$, $\phi_2 = x$, and receiver $= x$. Axial peak suppression and CYCLOPS phase cycling are performed to obtain an eight-step phase cycle. Frequency discrimination in F_1 is obtained by shifting the phase of ϕ_1 and the receiver according to the TPPI, States, or TPPI–States protocols (Section 4.3.4).

(assumed to represent a three-bond scalar interaction). For a two-spin system, initial I_{1z} magnetization evolves through the pulse sequence element as

$$I_{1z} \xrightarrow{\left(\frac{\pi}{2}\right)_x - t_1 - \left(\frac{\pi}{2}\right)_x} -I_{1z}\cos(\Omega_1 t_1)\cos(\pi J_{12} t_1) - 2I_{1x}I_{2y}\cos(\Omega_1 t_1)\sin(\pi J_{12} t_1) + I_{1x}\sin(\Omega_1 t_1)\cos(\pi J_{12} t_1) - 2I_{1z}I_{2y}\sin(\Omega_1 t_1)\sin(\pi J_{12} t_1), \quad [6.1]$$

in which $\left(\frac{\pi}{2}\right)_x$ represents a nonselective rf pulse with x-phase applied to the I spins. Parallel evolution beginning with I_{2z} magnetization is exhibited by exchanging I_1 and I_2 labels.

A product operator analysis of the COSY experiment reveals important features that must be considered while acquiring, processing, and analyzing COSY spectra. The essence of the product operator analysis for a two-spin system has already been presented (Section 4.2.1). In summary, the first two terms of [6.1] do not lead to observable magnetization and can be ignored, provided that the spin system achieves thermal equilibrium during the recycle delay (Section 6.3). The third term gives rise to a diagonal peak and the fourth term leads to a cross-peak modulated by Ω_1 in t_1 and Ω_2 in t_2. Manipulation of the trigonometric terms of [6.1] leads to a clearer understanding of the multiplet fine structure:

$$\sin(\Omega_1 t_1)\cos(\pi J_{12} t_1) = \tfrac{1}{2}[\sin(\Omega_1 t_1 - \pi J_{12} t_1) + \sin(\Omega_1 t_1 + \pi J_{12} t_1)], \quad [6.2]$$

$$\sin(\Omega_1 t_1)\sin(\pi J_{12} t_1) = \tfrac{1}{2}[\cos(\Omega_1 t_1 - \pi J_{12} t_1) - \cos(\Omega_1 t_1 + \pi J_{12} t_1)]. \quad [6.3]$$

As indicated by [6.2], the diagonal peak has an in-phase lineshape in F_1 with the two multiplet components centered at Ω_1 and separated by $2\pi J_{12}$; in contrast, [6.3] indicates that the cross-peak has an antiphase lineshape with the two components centered at Ω_1 and separated by $2\pi J_{12}$ (if Ω is given in units of angular frequency). The sinusoidal modulation of [6.2] and cosinusoidal modulation [6.3] mean that the diagonal and cross-peaks differ in phase by 90° and cannot both be phased to absorption simultaneously. Consideration of the evolution of I_{1x} and $2I_{1z}I_{2y}$ during t_2 indicates that the F_2 lineshapes of the diagonal and cross-peaks are the same as in the F_1 dimension.

The antiphase lineshapes of COSY cross-peaks have important implications for the way in which these data are collected and processed (Sections 6.2.1.2 and 6.2.1.3). In addition, the differences in the relative phase of diagonal and cross-peaks are one of the main shortcomings of

the COSY experiment: namely, when the cross-peaks are phased to absorption, the in-phase dispersive tails of the diagonal peaks obscure cross-peaks near the diagonal (arising from scalar-coupled protons close in chemical shift).

COSY cross-peaks between spins in more complex spin systems have fine structure in addition to the simple antiphase splitting of [6.3] (*5*). The product operator formalism can be used to elucidate the nature of this fine structure, although the calculations quickly become tedious to perform by hand if more than a few coupled spins are involved. For a cross-peak between spins I_1 and I_2, the component of the time-domain signal at the chemical shift of spin I_1 is proportional to (*6*)

$$\sin(\Omega_1 t)\,\sin(\pi J_{12} t)\prod_{k=3}^{K}\cos(\pi J_{1k} t)$$

$$=\frac{1}{2}[\cos(\Omega_1 t-\pi J_{12} t)-\cos(\Omega_1 t+\pi J_{12} t)]\prod_{k=3}^{K}\cos(\pi J_{1k} t), \qquad [6.4]$$

in which t represents either the t_1 or t_2 evolution period (depending upon whether the cross-peak represents $I_1 \rightarrow I_2$ or $I_2 \rightarrow I_1$ coherence transfer), J_{12} is the active scalar coupling between spin I_1 and spin I_2, and J_{1k} is the value of the passive scalar coupling between spin I_1 and spin I_k ($k > 2$). A similar equation would represent the signal at the chemical shift of the I_2 spin, except that the product would extend over the passive scalar-coupled partners of the I_2 spin. The product of the two sine terms on the left-hand side of [6.4] gives rise to the antiphase splitting by the active coupling J_{12}. Because the product of two cosine terms can be decomposed into a sum of cosine terms, after Fourier transformation, [6.4] yields in-phase absorption components for the passive scalar coupling interactions. The appearance of cross-peaks for amino acid spin systems for a variety of coupling constants and linewidths has been described (*7*). In the special case of scalar coupling between spin I_1 and an I_n group, in which n is the number of magnetically equivalent spins, the cross-peak is considered to have one active coupling and $(n-1)$ passive couplings; as a result, the relative intensities of the fine-structure components are described by the antiphase Pascal triangle (*6*).

6.2.1.2 Experimental Protocol Aside from the details of experimental protocols common to all 2D experiments (e.g., setting the rf transmitter frequency, calibrating the 90° pulse length, choosing spectral widths, and determining the recycle delay), the nature of coherence transfer and of lineshapes in a COSY experiment requires additional

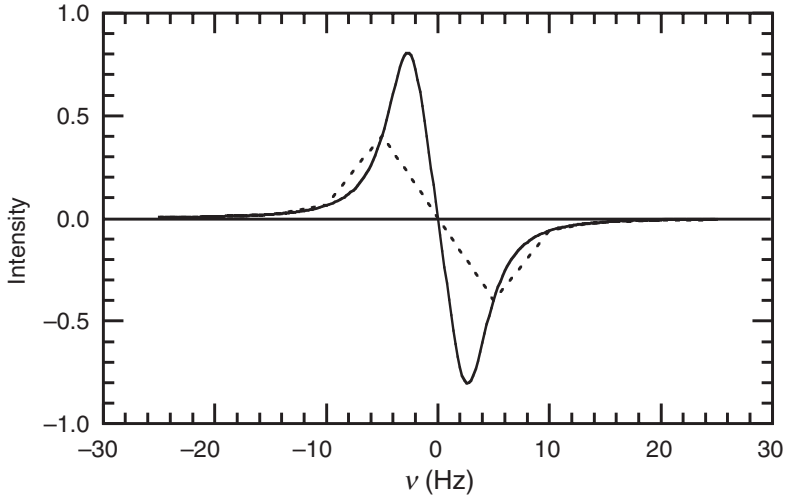

FIGURE 6.3 Variation in the peak height of an antiphase absorptive doublet as the digital resolution is decreased to approach the size of the peak splitting. Both curves represent data for an antiphase pair of Lorentzian lines with half-height width 5 Hz and a separation of 5 Hz. The solid curve has a digital resolution of 0.2 Hz/point and accurately traces the lineshape. The broken curve has a digital resolution of 5 Hz/point and clearly has a smaller vertical separation of the positive and negative extrema. Note that the exact decrease in peak height will depend on where the low digital resolution points fall on the curve.

consideration. Digital resolution in the frequency domain has a profound influence on the relative cross-peak intensity of antiphase lineshapes. If the digital resolution in F_1 or F_2 is too low, the positive and negative lobes of the cross-peak will cancel partially, and the intensity of the cross-peak will be reduced as indicated in Fig. 6.3. Equivalently, in the time domain the cross-peak product operators contain $\sin(\pi J_{IS} t_1)$ and $\sin(\pi J_{IS} t_2)$ trigonometric terms arising from the active scalar coupling interaction [6.1] that are superposed upon the terms reflecting chemical shift evolution; in this respect, the COSY experiment is said to generate sine-modulated data. Consequently, evolution in t_1 and t_2 must occur for times comparable to or greater than $1/(4J_{12})$ to $1/(2J_{12})$ (approximately 62 to 125 ms for a 4-Hz coupling constant) if observable cross-peaks are to be obtained. The parameter $t = 1/(2J_{12})$ occurs many times in discussions of scalar correlated experiments, because coherence transfer occurs via antiphase terms with magnitudes proportional to $\sin(\pi J_{12} t)$. Acquisition for a sufficient length of time in t_2 is rarely

a problem, as a greater proportion of the recycle delay can be spent recording each FID without lengthening the total acquisition time of the experiment. Commonly, each FID is collected for $t_{2\,\max} \gg 1/(2J_{12})$ and is truncated at the processing stage to achieve the desired amount of sensitivity or resolution enhancement. In contrast, increasing $t_{1\max}$ by increasing the number of data points in each interferogram adds linearly to the total acquisition time because a new FID must be collected for each additional t_1 value.

For a protein in the 8- to 10-kDa range, COSY is one of the most sensitive proton 2D experiments. A reasonable S/N ratio can be obtained in a few hours using a 500-MHz NMR spectrometer equipped with a conventional probe for a protein sample concentration of $\sim$1 mM; even less sample is required if a cryogenic probe is available. For example, assuming a 10-ppm spectral width in F_1, and a recycle delay of 2.0 s (t_2 acquisition for 0.3 s and equilibrium recovery and/or solvent presaturation for 1.7 s), a COSY experiment with eight transients for each of 512 t_1 increments could be recorded in just over 2 hours and would have a $t_{1\max}$ of 50 ms. If cross-peaks arising from small coupling constants are to be observed (e.g., $^3J_{H^NH^\alpha}$ couplings in residues adopting helical conformations), then additional t_1 increments can be recorded so as to bring $t_{1\max}$ into the 80-ms range. Alternatively, the number of t_1 increments can be kept constant and $t_{1\max}$ increased by decreasing the F_1 spectral width; however, care must be taken to avoid folding diagonal peaks on top of cross-peaks. Increasing $t_{1\max}$ beyond 100 ms is unlikely to bring significant improvements in S/N because of extensive relaxation during the longer values of t_1. For more dilute samples, the number of transients collected for each t_1 increment must be increased.

Except as noted in the figure captions in this chapter, the COSY spectra of ubiquitin were acquired with 16 transients for each of 800 t_1 values with an F_1 spectral width of 5800 Hz; TPPI was used for frequency discrimination in t_1 and $t_{1\max} = 69$ ms. The acquisition time for each FID was 330 ms (spectral width, 6250 Hz over 2048 complex points), although $t_{2\max}$ was usually reduced at the processing stage (see later). The water resonance was suppressed by presaturation for 1.5 s. The total acquisition time was just over 7 hr.

The effect of $t_{1\max}$ on COSY spectra of ubiquitin is illustrated in Fig. 6.4. As $t_{1\max}$ decreases from 69 to 17.2 ms, the cross-peaks become less intense because of self-cancellation of the antiphase multiplet components. At the shortest values of $t_{1\max}$, the cross-peak of Asp21 is not observed and the characteristic glycine fine structure of the Gly47 cross-peak disappears.

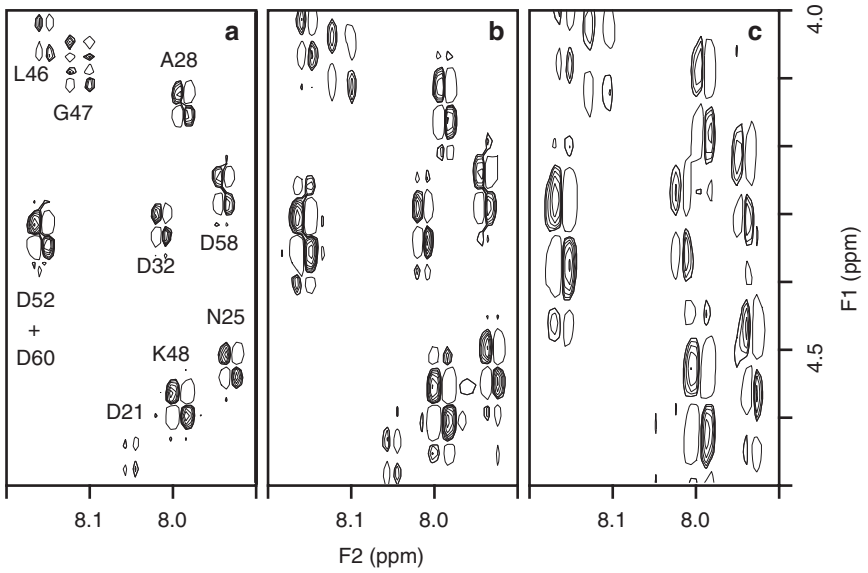

FIGURE 6.4 Sections of the $^1H^N$–$^1H^\alpha$ region of COSY spectra acquired with the same total acquisition time (8 hr) but with different values of t_{1max}: (a) 16 transients per increment, $t_{1max} = 69$ ms; (b) 32 transients per increment, $t_{1max} = 34.5$ ms; (c) 64 transients per increment, $t_{1max} = 17.2$ ms. All spectra were processed with an unshifted sine bell in t_2 and a sine bell shifted 20° over the available data and zero-filled to 1024 points in t_1. As t_{1max} decreases, many of the peaks become weaker and that of Asp21 is lost completely. Also note that the characteristic glycine fine structure is not present at the shorter values of t_{1max} (see cross-peak of Gly47), making identification of these residues difficult.

6.2.1.3 Processing As surmised from [6.1], the cross- and diagonal peaks are 90° out of phase in COSY spectra. In the normal mode of display, the cross-peaks are phased to have antiphase absorptive lineshapes in both dimensions, and the diagonal peaks are phased to have in-phase dispersive lineshapes in both dimensions. Because the tails of the diagonal peaks can obscure information-containing cross-peaks, processing procedures for COSY spectra are designed to maximize cross-peak intensity and minimize diagonal peak intensity. Because cross-peak lineshapes present in a COSY spectrum are antiphase, apodization functions emphasizing the initial parts of each FID do not improve the S/N ratio; instead, window functions must include data points up to $1/(2J_{IS})$, where J_{IS} is the magnitude of the

active coupling constant leading to the cross-peak. Strongly resolution-enhancing window functions such as unshifted or slightly phase shifted sine bells are used for COSY spectra. As an added bonus, the use of an unshifted sine bell in t_2 severely attenuates any residual H_2O peak, leading to spectra with very flat baselines and no significant ridges emanating from the F_2 water stripe. The t_1 window function is a compromise between reduction of the diagonal tails (unshifted or slightly shifted sine bell) and sensitivity (increasingly shifted sine bell).

An unshifted sine bell applied over 150 ms of the acquired data in t_2 and a 15°–30° phase-shifted sine bell applied over all data points in t_1 will usually give adequate results for cross-peaks far from the diagonal, such as those arising from $^1H^N$–$^1H^\alpha$ correlations. Enhanced resolution and a concomitant reduction in diagonal peak intensity can be achieved by increasing t_{2max} to 200–300 ms, and by shifting the F_1 sine bell by 0°–10°. Such processing is used for the observation of cross-peaks close to the diagonal, such as in those involving leucine, valine, or isoleucine methyl resonances. The exact processing parameters used for the example ubiquitin spectra are described in the figure captions in this chapter. Figure 6.5 illustrates the use of strong resolution enhancement to aid in the observation of the correlations involving the methyl groups of the leucine, isoleucine, and valine.

The choice of correct phase parameters in F_2 is not readily apparent from the Fourier transform of the row of data collected with the smallest value of t_1. In order to determine the phase parameters, a 1D pulse–acquire spectrum is acquired with the same pulse length, carrier position, and spectral width as for the 2D COSY experiment. The phase corrections determined for the 1D spectrum can then be applied during the F_2 processing of the COSY, possibly with the zero-order phase correction adjusted by 90°, depending on the exact phase cycles used in the two experiments. With the high speed of modern computer workstations, an alternative is to process the spectrum in both dimensions, determine the required phase parameters by examining several rows of the data, and then reprocess the entire spectrum with phase corrections added. The phase correction required in F_1 will result from precession of the spins during the finite pulse lengths of the pulses on either side of t_1, and during the initial value of t_1. The amount of precession can be calculated, thus the F_1 phase parameters may be calculated and applied during processing (Section 3.3.2.3).

During the extraction of coupling constants from the cross-peak fine structure (Section 6.2.1.5), analysis should be performed on F_2 sections of spectra that have been substantially zero-filled in this dimension. Obtaining a digital resolution of about 0.5 Hz/point is usually adequate.

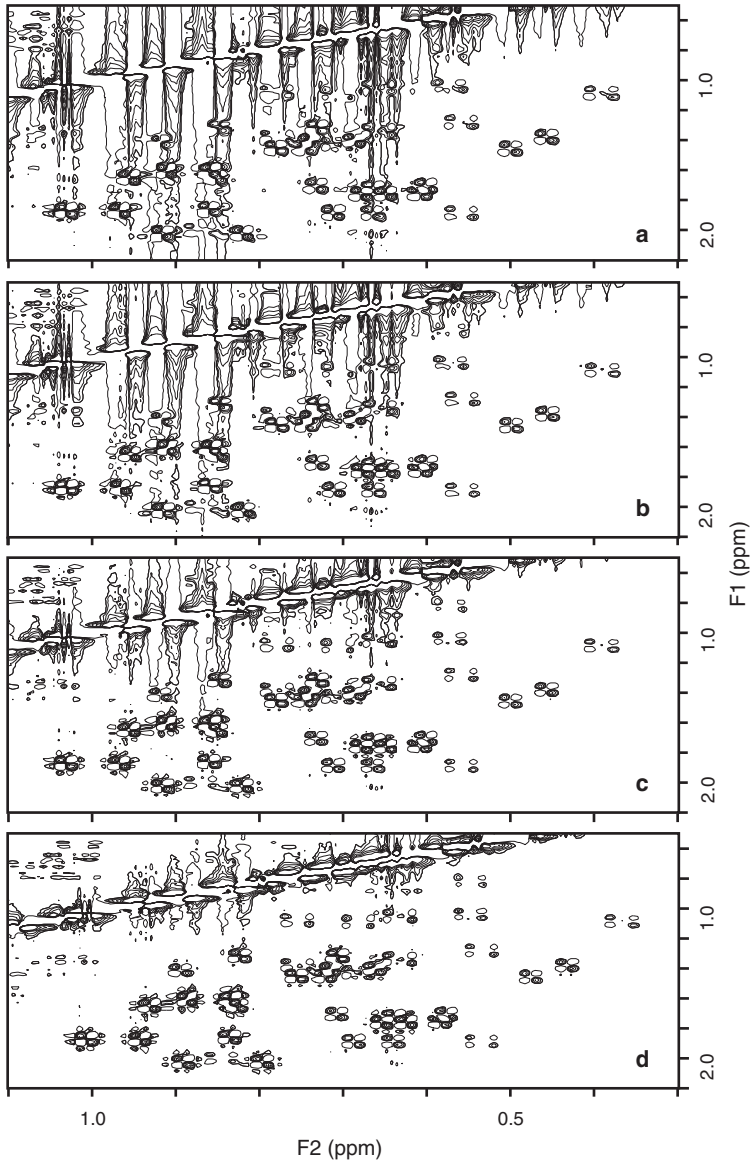

FIGURE 6.5 The effect of t_1 window functions on COSY spectra. The same data set was reprocessed with the sine bells applied in t_1 shifted by the following amounts: (a) 30°, (b) 20°, (c) 10°, (d) 5°. As the window function becomes more resolution enhancing, the peaks close to the diagonal are less obscured by the dispersive tails from the diagonal.

In order to reduce the data storage requirements and processing time of such a large spectrum, F_2 regions that do not contain the peaks of interest may be discarded after the F_2 Fourier transformation.

6.2.1.4 Information Content The power of the COSY experiment lies in the ability to provide correlations between pairs of protons separated by two or three bonds. However, assigning entire spin systems in the COSY spectrum is rarely possible because of chemical shift degeneracy in the upfield region of the spectrum. Instead, the COSY spectrum is best used to identify correlations in the so-called fingerprint regions. These regions are well separated from each other and usually contain well-resolved cross-peaks, the number of which reflect the amino acid composition of the protein. The usual regions of interest are the $^1H^N$–$^1H^\alpha$ cross-peaks (the backbone fingerprint), the $^1H^\alpha$–$^1H^\beta$ cross-peaks (this region can get very crowded and is therefore of limited usefulness), cross-peaks between the aromatic resonances of phenylalanine, tyrosine, tryptophan, and histidine side chains, cross-peaks involving the isoleucine, valine, and leucine methyl groups, and the cross-peaks involving alanine and threonine methyl groups. Other correlation experiments such as TOCSY (Section 6.5) or relayed COSY (Section 6.2.2) can then be used to connect these fragments together to form complete spin system assignments. Figure 6.6 indicates these regions of the COSY spectrum while Figs. 6.7 and 6.8 show details of the two methyl fingerprint regions of ubiquitin. COSY is a relatively sensitive experiment (with the provisos given later for resonances with large linewidths or small coupling constants), and can be used to check sample purity or homogeneity. While the absence of some expected correlations in the fingerprint regions usually is indicative of experimental shortcomings (e.g., resonance overlap), the presence of extra resonances indicates deficiencies in the purity or conformational homogeneity of the sample.

The COSY spectrum of a protein of N residues, containing P proline and G glycine residues, should display $N-P+G-1$ correlations in the $^1H^N$–$^1H^\alpha$ fingerprint region (the N-terminal residue usually is not observed). At low pH, arginine $^1H^\delta$–$^1H^\varepsilon$ cross peaks can be observed in the $^1H^N$–$^1H^\alpha$ fingerprint region. The number of observed correlations is often less than expected due to rapid amide proton exchange with solvent, coincidence of the $^1H^\alpha$ and water resonances (and therefore attenuation by the solvent presaturation process), or degeneracy of both $^1H^\alpha$ protons of a glycine residue. Double-quantum (2Q) spectroscopy (Section 6.4.1) can provide a useful means of observing correlations absent for the two latter reasons, while the pre-TOCSY COSY

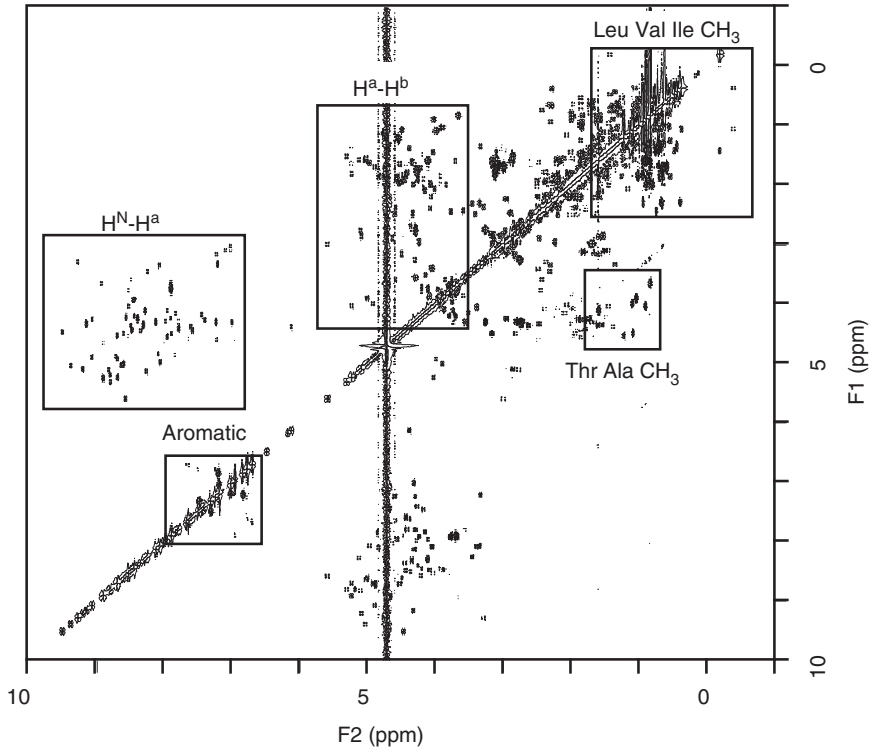

FIGURE 6.6 The five regions of the COSY spectrum containing the fingerprint cross-peaks.

(Sections 6.2.1.6 and 6.5.5) and gradient-enhanced 2Q filtered (2QF)-COSY (Section 6.3) experiments circumvent problems of $^1H^{\alpha}$ coincidence with the water resonance.

Ubiquitin contains 76 residues, including three prolines and six glycines; therefore, 78 $^1H^N$–$^1H^{\alpha}$ resonances are expected. The 70 peaks are plainly visible in Fig. 6.9. A more detailed analysis of the COSY and other spectra indicates that the other eight cross-peaks are not observed for the following reasons: (*i*) the $^1H^{\alpha}$ resonances of Val5, Leu15, and Arg54 are coincident with the H_2O signal, (*ii*) the amide protons of Glu24 and Gly53 are very broad, (*iii*) $^1H^N$ and $^1H^{\alpha}$ resonances of Asp52 and Asp60 have identical shifts, and (*iv*) $^1H^{\alpha}$ and $^1H^{\alpha'}$ of Gly75 are degenerate. Thus, the backbone resonances of all residues can be identified.

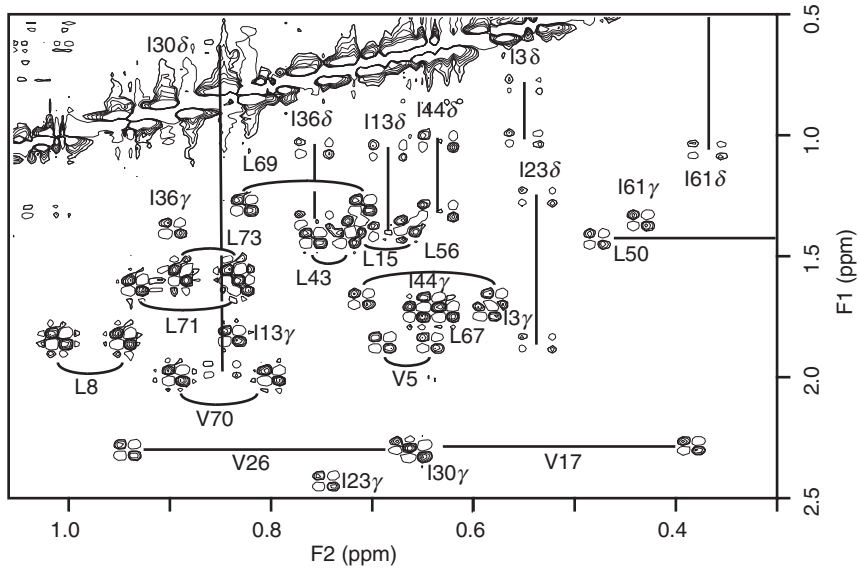

FIGURE 6.7 Section of the H_2O COSY spectrum showing the cross-peaks in the leucine, valine, and isoleucine methyl fingerprint region. The cross-peaks are labeled with the corresponding resonance assignment. This spectrum is the same as that in Fig. 6.5d.

6.2.1.5 Quantitation of Scalar Coupling Constants in COSY Spectra The value of the ^3J scalar coupling constant can be determined from the fine structure in a COSY cross-peak for spins without passive coupling partners, such as the $^3J_{H^N H^\alpha}$ of residues other than glycine in H_2O solution, and the $^3J_{H^\alpha H^\beta}$ for residues with a single $^1H^\beta$ in D_2O solution. The presence of a passive coupling in glycine $^1H^N$–$^1H^\alpha$ cross-peaks and $^1H^\alpha$–$^1H^\beta$ cross-peaks within residues with two $^1H^\beta$ protons complicates the analysis and the scalar coupling constants are more conveniently obtained from exclusive correlation spectroscopy (E.COSY) spectra (Section 6.3.3).

Although the product operator analysis of COSY indicates that the lobes of a cross-peak in a two-spin system are separated by J_{12}, the effect of the linewidth on the antiphase lineshape has not been considered. Qualitatively, as the linewidth approaches or exceeds the size of the coupling constant, cancellation of the positive and negative multiplet components reduces the intensity and increases the apparent separation

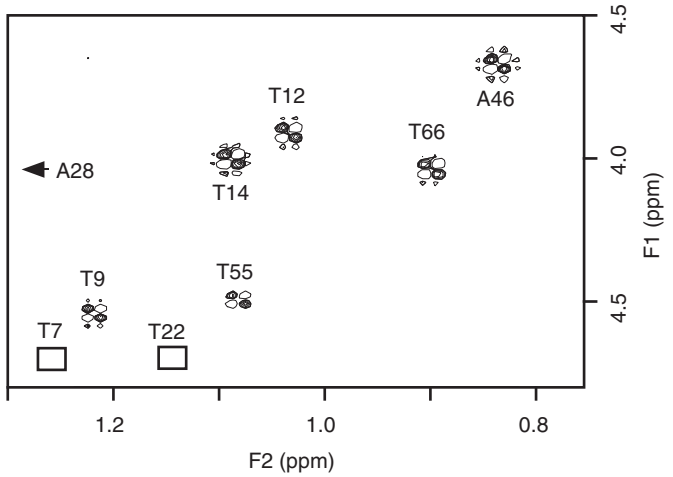

FIGURE 6.8 Section of the COSY spectrum showing the cross-peaks in the alanine and threonine methyl fingerprint region. The cross-peaks are labeled by the one-letter amino acid code and the residue number. The arrow indicates a cross-peak falling outside the spectral region shown. For Thr7 and Thr22, the $^1H^{\beta}$ protons are coincident with the water resonance and are attenuated by presaturation. These correlations are observed in D_2O solution, in a pre-TOCSY COSY (Section 6.2.1.5 and Fig. 6.15), and in a gradient-enhanced 2QF-COSY (Section 6.3.1 and Fig. 6.26).

of the multiplet as shown in Fig. 6.10. Quantitatively, the antiphase absorptive lineshape is given by [3.26]

$$\begin{aligned} A(\nu) &= \frac{1}{1+(J_{12}-2\nu)^2/\Delta\nu_{\mathrm{FWHH}}^2} - \frac{1}{1+(J_{12}+2\nu)^2/\Delta\nu_{\mathrm{FWHH}}^2} \\ &= \frac{1}{1+p^2(1-2\nu/J_{12})^2} - \frac{1}{1+p^2(1+2\nu/J_{12})^2}, \end{aligned} \qquad [6.5]$$

in which the individual multiplet components are assumed to have Lorentzian lineshapes with linewidth $\Delta\nu_{\mathrm{FWHH}}$, $p = J_{12}/\Delta\nu_{\mathrm{FWHH}}$, and the lineshape is normalized to unit amplitude. The extrema are obtained by setting the derivative of [6.5] with respect to ν equal to zero, and solving the resulting equation for ν:

$$\nu = \pm\frac{J_{12}}{2\sqrt{3}p}\left[p^2 + 2\sqrt{p^4+p^2+1} - 1\right]^{1/2}. \qquad [6.6]$$

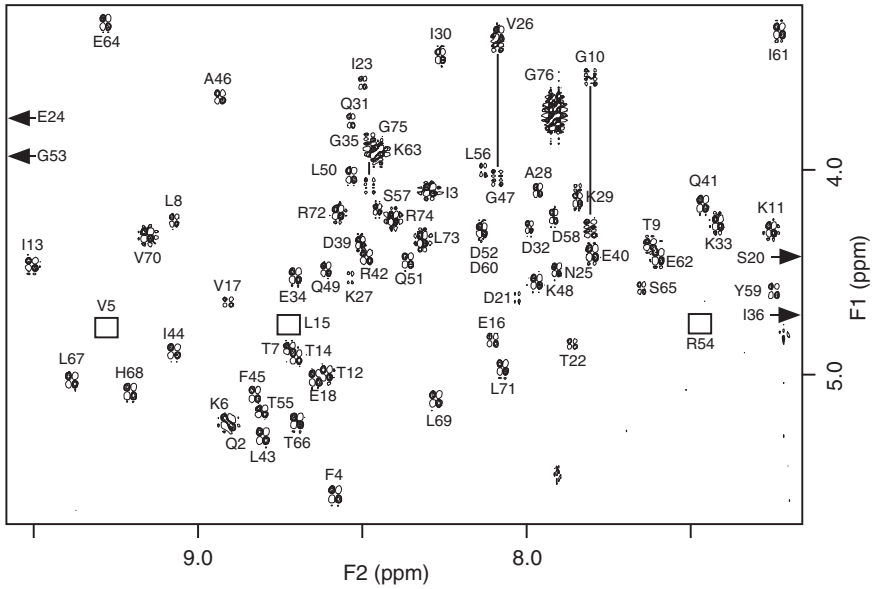

FIGURE 6.9 $^1H^N$–$^1H^\alpha$ fingerprint region of ubiquitin. The cross-peaks are labeled by the one-letter amino acid code and the residue number. The arrows indicate cross-peaks falling outside the spectral region shown. The boxes indicate residues whose H^α protons are coincident with the H_2O resonance, hence the cross-peak is suppressed by presaturation. These correlations are observed in a pre-TOCSY COSY (Section 6.2.1.5 and Fig. 6.15) or gradient-enhanced 2QF-COSY (Section 6.3.1 and Fig. 6.26). See text for a more complete account of the peaks present in this spectrum.

Because this equation provides the values of ν at the maximum and minimum amplitude of the lineshape, substitution of [6.6] back into [6.5] allows a determination of the apparent peak heights of the multiplet lines. The resulting equation is shown graphically in Fig. 6.11. This confirms the qualitative view of Fig. 6.10: as J_{12} is reduced with respect to $\Delta\nu_{FWHH}$, the intensity of a COSY cross-peak decreases. Thus, in the case of equivalent linewidth and coupling constant ($p = 1$), the resultant COSY peak intensity will be ≈80% of the value of a single Lorentzian line; linewidths in the range 6–8 Hz are expected for ubiquitin, and the intensity of many cross-peaks will be reduced by this amount or more.

The decrease in cross-peak intensity caused by broad lines can severely limit the information content of a COSY spectrum, but more insidious is the effect on the separation of the peak maxima. Because the

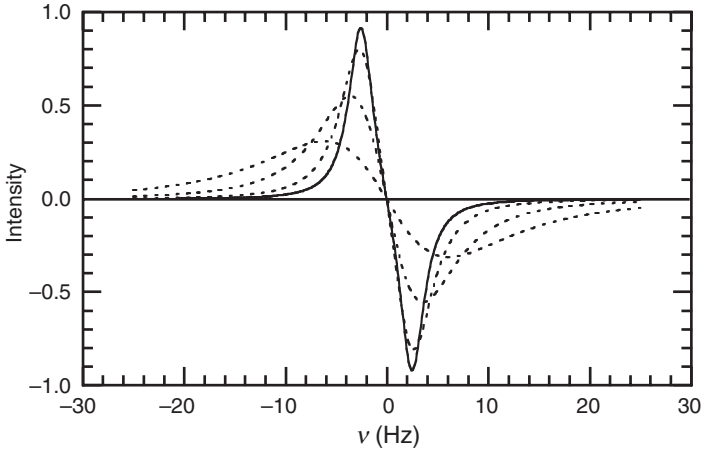

FIGURE 6.10 Changes observed for a Lorentzian antiphase absorptive doublet as the apparent peak separation varies as a function of linewidth. The Lorentzian lines are separated by 5 Hz and have a half-height width of 3 (solid curve), 5, 10, or 20 Hz. All curves are plotted such that a single Lorentzian line would have a height of unity.

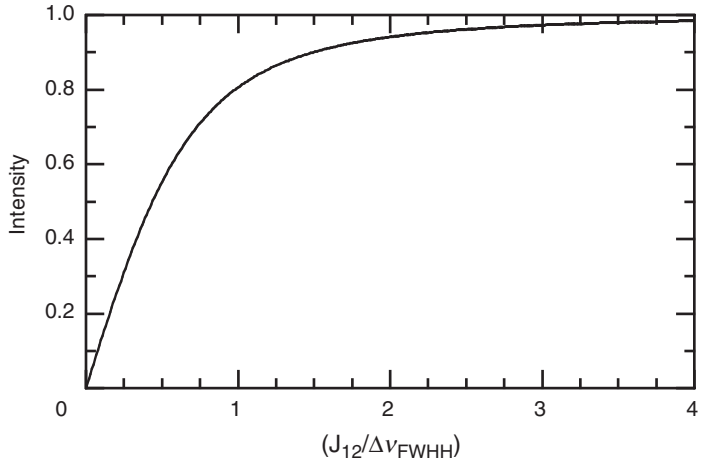

FIGURE 6.11 Peak height of a Lorentzian antiphase absorptive doublet varies as the ratio of the peak separation to the linewidth, $J_{12}/\Delta\nu_{\mathrm{FWHH}}$.

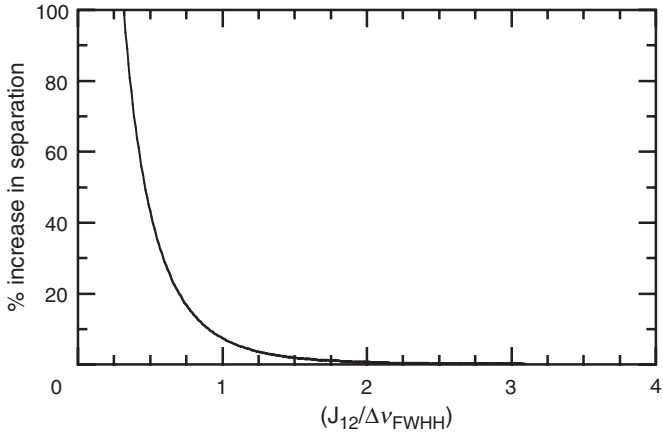

FIGURE 6.12 Apparent separation of peak maxima relative to the actual separation of a pair of absorptive antiphase Lorentzian lines as a function of linewidth. As $J_{12}/\Delta\nu_{FWHH}$ approaches infinity, the separation approaches J_{12}. As $J_{12}/\Delta\nu_{FWHH}$ approaches zero, the separation tends to a limit of $\Delta\nu_{FWHH}/3^{1/2}$.

values of ν given by [6.6] represent the frequency at which the amplitude is a maximum or a minimum (given by the "+" or "−" solutions, respectively), the total separation of the peak maxima is given by

$$\nu_a = \frac{J_{12}}{\sqrt{3}p}\left[p^2 + 2\sqrt{p^4 + p^2 + 1} - 1\right]^{1/2}. \qquad [6.7]$$

This equation was first described by Neuhaus et al. (*6*) and is most useful in the form shown in Fig. 6.12. The graph indicates that the observed separation is always larger than the actual value of J_{12}. Moreover, Fig. 6.12 indicates that the smaller the value of p (the larger the linewidth with respect to the multiplet separation), the larger the difference between the actual separation of the initial Lorentzian lines (J_{12}) and the observed separation of the peak maxima. Thus, to continue the example just described, when the linewidth is equal to the J_{12} coupling ($p = 1$), the observed separation of peak maxima will be 7% higher than J_{12}. The error in J_{12} increases rapidly as p decreases below 1. Self-cancellation is especially problematic for residues in a helical environment; the $^3J_{H^NH^\alpha}$ coupling constant calculated for an ideal helix (with $\phi = -60^\circ$ and $\theta = |\phi - 60^\circ|$) using the Karplus equation [9.2] is 4.2 Hz.

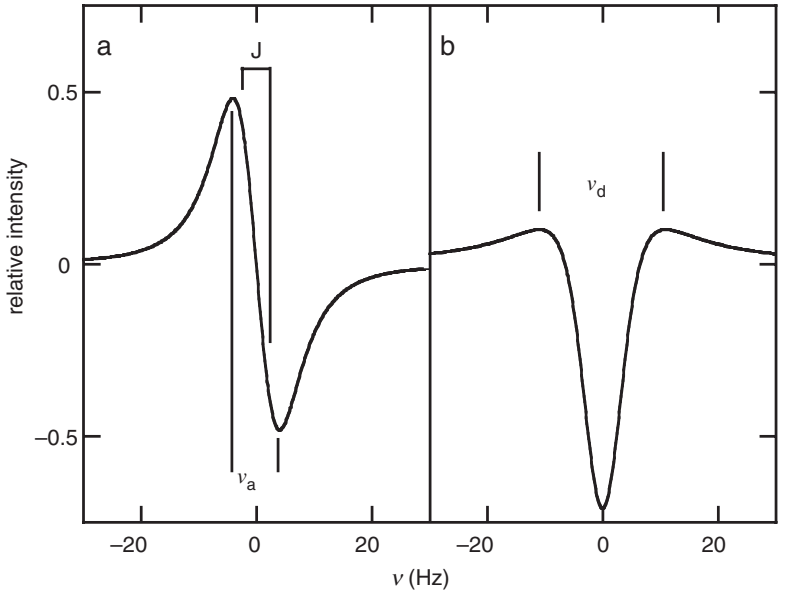

FIGURE 6.13 Measurement of the maxima separation for a pair of antiphase Lorentzian lines in absorption (ν_a) and dispersion (ν_d). In both panels, real separation is 5.0 Hz (denoted by J in the left-hand panel) and the half-height linewidth is 10 Hz ($p = 0.5$). Measurement of ν_d is difficult when $p > 1.0$ because of the low intensity of the broad positive lobes.

A method of determining scalar coupling constants that takes into account the natural properties of a Lorentzian line to overcome the problems of self-cancellation has been proposed by Kim and Prestegard (*8*). The method takes advantage of the differences in lineshapes of absorptive and dispersive antiphase Lorentzian multiplets. Analogously to [6.7], a pair of simultaneous equations describing the coupling constant and the linewidth, J_{12} and $\Delta\nu_{\mathrm{FWHH}}$, in terms of the absorptive and dispersive peak separations, ν_a and ν_d, can be solved to give (Fig. 6.13):

$$\begin{aligned} 64\nu_a^2 J_{IS}^6 - 64\nu_a^2\nu_d^2 J_{IS}^4 + \left(-144\nu_a^6 + 96\nu_a^4\nu_d^2 + 36\nu_a^2\nu_d^4\right)J_{IS}^2 \\ + 81\nu_a^8 - 36\nu_a^6\nu_d^2 - 42\nu_a^4\nu_d^4 - 4\nu_a^2\nu_d^6 + \nu_d^8 = 0. \end{aligned} \quad [6.8]$$

The real root of this cubic equation in J_{12}^2 provides the coupling constant. The method is performed most easily by processing the COSY with antiphase absorptive cross-peaks (i.e., in the normal way, although

with high digital resolution). The absorptive peak separation, ν_a, is measured from a row (F_2 cross-section) through a given cross-peak. Adding a zero-order phase correction of 90° to the row allows measurement of the dispersive peak separation, ν_d, for the same cross-peak. This method assumes that the lineshape is Lorentzian and is not applicable if window functions such as shifted sine bells or Lorentzian–Gaussian transformations have been employed in t_2. The method works reasonably well for cross-peaks with high signal-to-noise ratio; however, for noisy data, accurate measurement of ν_d is difficult because the tops of the peaks are broad.

Alternatively, [6.5] can be fit directly to the F_2 cross-section through a cross-peak (or several rows co-added to improve the S/N ratio) by a nonlinear least-squares algorithm to determine the values of the scalar coupling constant and linewidth most consistent with the lineshape (*9*, *10*). Once again, the spectrum should be processed to maintain Lorentzian lineshapes in F_2. The accuracy of this approach also is compromised as p decreases, owing to the lower S/N ratios. Several methods of analysis of ^{1}H spectra have been reported to be of use in situations where the linewidth is greater then J_{12} (*11–13*).

Practically, scalar coupling constants that are less than about half of the linewidth are difficult to measure by analysis of antiphase splittings in the COSY experiment. Even the "best" method of direct line-fitting is rarely useful for the larger proteins studied by NMR (>15 kDa) and scalar coupling constants are better obtained using heteronuclear experiments (Section 7.5).

6.2.1.6 Experimental Variants The basic COSY pulse sequence has been extensively modified since its initial conception. Four examples are briefly mentioned here: COSY-β, purged COSY (P.COSY), pre-TOCSY COSY, and COSY with SCUBA. The first of these provides a means to simplify cross-peak fine structure while the latter three address deficiencies in the basic experiment.

In the COSY-β experiment, the rotation angle of the second pulse is $\beta < 90°$. Reduction of the length of the final pulse in the COSY-β experiment has two effects on the resulting spectra. First, the diagonal peaks are more intense relative to the cross-peaks because coherence transfer scales as $\sin^2(\beta)$. Second, the fine structure of the cross-peaks changes because connected and unconnected transitions have different intensities. In spin systems with three or more mutually coupled spins, certain components of a given cross-peak arising from passive coupling will be reduced in intensity. Acquisition with $\beta = 35°$ provides reasonable sensitivity while suppressing cross-peak components arising from

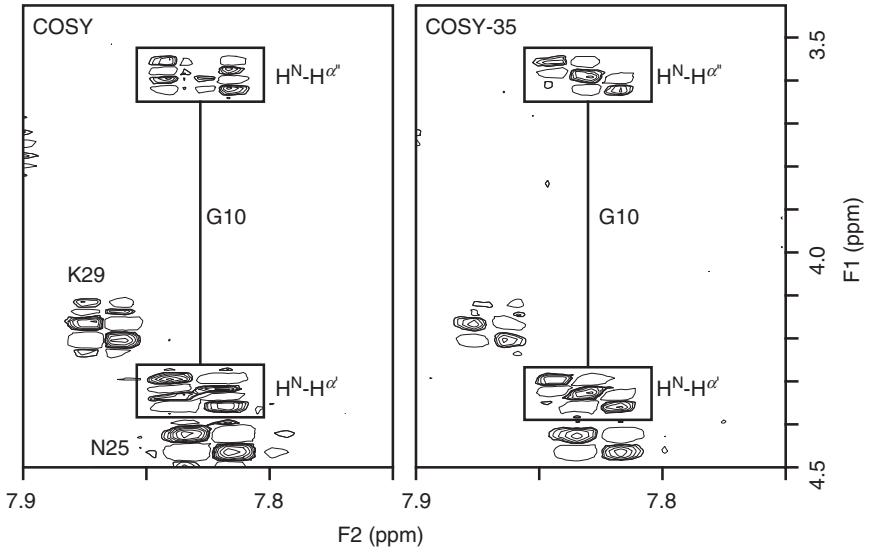

FIGURE 6.14 Cross-peaks of Gly10 in the COSY-35 experiment. Compared to the normal COSY, contributions from the passive coupling $^2J_{H^{\alpha'}H^{\alpha''}}$ are removed from the $^1H^N$–$^1H^\alpha$ cross-peaks in F_1 while the passive coupling of $^1H^N$ to the other $^1H^\alpha$ is removed in F_2. The fine structure of cross-peaks to nonglycine residues is not affected by the reduced flip angle.

unconnected transitions by tenfold, compared to those of connected transitions (*4*). An example of the simplification obtained is shown in Fig. 6.14 for the cross-peaks arising from Gly10. The multiplet fine structure in COSY-β is similar to that observed in E.COSY (*14*), and will be discussed in more detail later (Section 6.3.3). Although the removal of some elements of fine structure can facilitate identification of peaks in crowded regions of the spectrum, the COSY-β experiment offers little benefit for spin system identification and principally permits scalar coupling constants to be measured without errors of the type described in Fig. 6.12.

The P.COSY experiment provides a way to remove the dispersive diagonal tails of the COSY experiment without a significant loss in sensitivity (*15*). The central idea in the technique is similar to that of the primitive E.COSY (P.E.COSY; Section 6.3.3). In the P.E.COSY, a COSY-35 and a COSY-0 are subtracted, with the result that the diagonal is severely attenuated (*16*). This experiment suffers from a lack of sensitivity because the cross-peaks have low intensity in the COSY-35

spectrum and are not present at all in the COSY-0 spectrum. These issues are rectified in the P.COSY by generating cross-peaks in a normal COSY experiment and preparing a "diagonal-only" spectrum by repeated left shifting of a 1D spectrum acquired with high S/N (*15*). The resulting spectrum is comparable in quality to a 2QF-COSY (Section 6.3.1) but with twofold greater sensitivity.

As already described, cross-peaks in the $^1H^N$–$^1H^\alpha$ fingerprint region of COSY spectra are attenuated by presaturation of the solvent resonance. The simple expedient of including a short isotropic mixing period (Section 4.2.2) between the presaturation period and the first 90° pulse restores intensity to these cross-peaks. The mixing period transfers magnetization from $^1H^N$ to $^1H^\alpha$ via the $^3J_{H^NH^\alpha}$ scalar coupling interaction; therefore, $^1H^\alpha$ magnetization is present at the start of the COSY sequence even for the protons coincident with the water resonance. This variant is referred to as the pre-TOCSY COSY (*17*). An example of such a spectrum is shown in Fig. 6.15; the cross-peaks

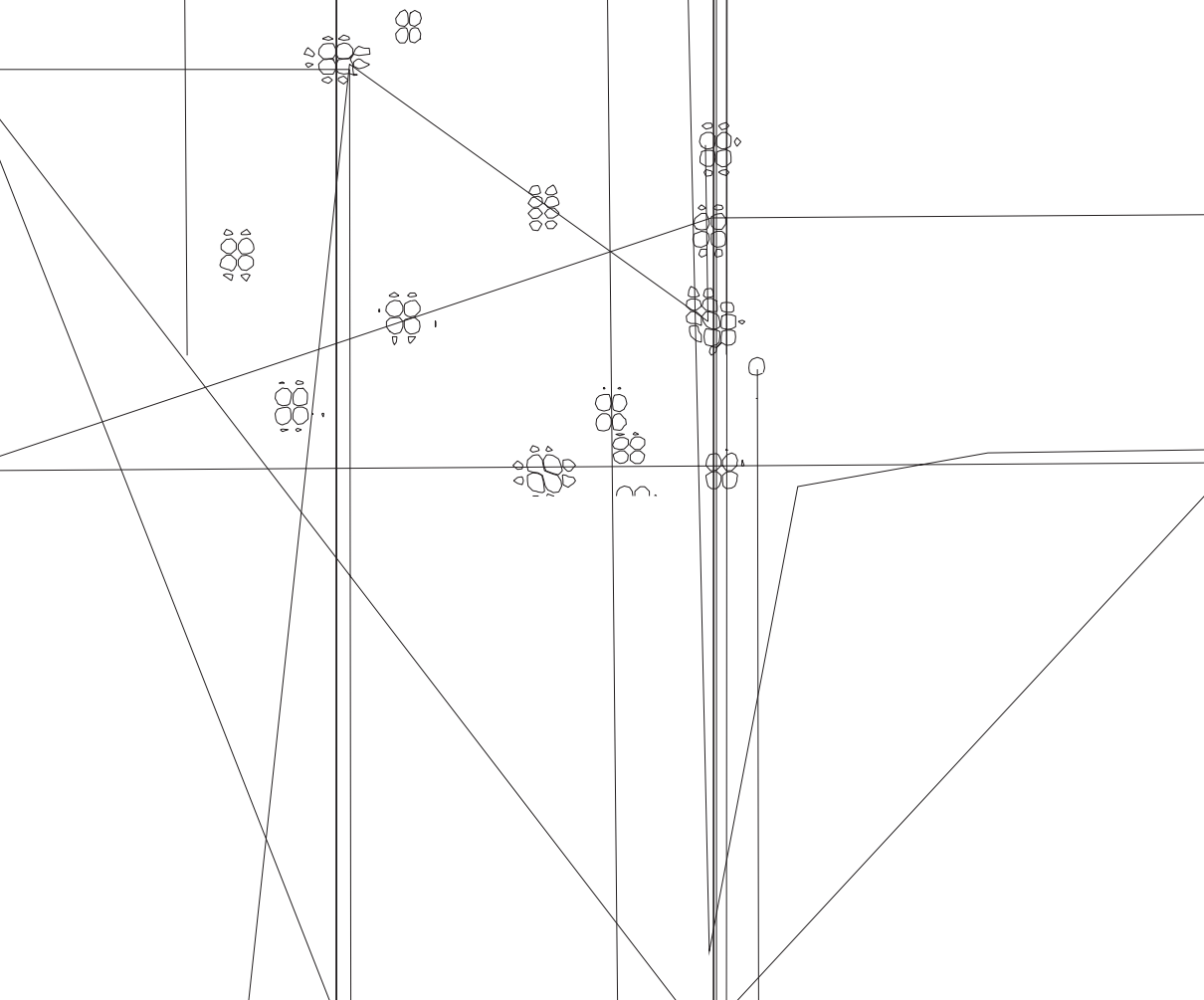

from Val5, Leu15, and Arg54 are plainly visible in this spectrum, but are missing from Fig. 6.9. Further discussion of pre-TOCSY sequences can be found in Section 6.5.5.

Cross-relaxation between spins whose resonances have been unavoidably saturated along with the water and spatially nearby unsaturated spins can be used as an alternative to the pre-TOCSY technique. This simple strategy, referred to as SCUBA (Stimulated Cross-peaks Under Bleached Alphas) (*18*), involves inserting a short period after the water presaturation sequence has ended and just prior to the initial 90° pulse of the COSY sequence. During this time period, which should be kept short relative to the ^{1}H T_1 values, equilibration occurs as a result of dipolar cross-relaxation between the saturated and unsaturated protein resonances. Thus, some magnetization will be restored to the saturated resonances prior to the start of the COSY sequence, allowing signals to be observed from the normally bleached region of the spectrum. This technique can be employed in any experiment that uses presaturation to suppress the water signal. Caution needs to be taken in using the SCUBA and pre-TOCSY techniques if peak intensities or volumes are to be quantified.

6.2.2 RELAYED COSY

Conceptually, the relayed coherence transfer experiments (RCT-COSY, relayed COSY, or R.COSY) are simple extensions of the COSY experiment (*19*). Instead of acquiring the spectrum after a single coherence transfer step from spin I_1 to spin I_2, a delay is introduced prior to acquisition to allow antiphase magnetization to develop for a second time. If spin I_2 has coupling partners other than I_1 (e.g., spin I_3), antiphase coherence will develop between I_2 and I_3 and a third 90° pulse will transfer coherence from I_2 to I_3. Because chemical shifts are only monitored during t_1 (prior to the first coherence transfer step) and t_2 (after the second coherence transfer step), the result will be a cross-peak between spin I_1 and spin I_3 even if I_1 and I_3 are not directly coupled. For simple molecules containing only a few resonances, such spin gymnastics are redundant, because in the COSY experiment both the $I_1 \rightarrow I_2$ and $I_2 \rightarrow I_3$ cross-peaks are readily observed. However, in the complex spectra of proteins, chemical shift degeneracy of spin I_2 with resonances of other spin systems can hinder the assignment of I_1 and I_3 to the same spin system. In such cases, the cross-peak between I_1 and I_3 in the R.COSY experiment places I_1 and I_3 unequivocally in the same amino acid spin system. The pulse sequence used to observe relayed coherence transfer is shown in Fig. 6.16.

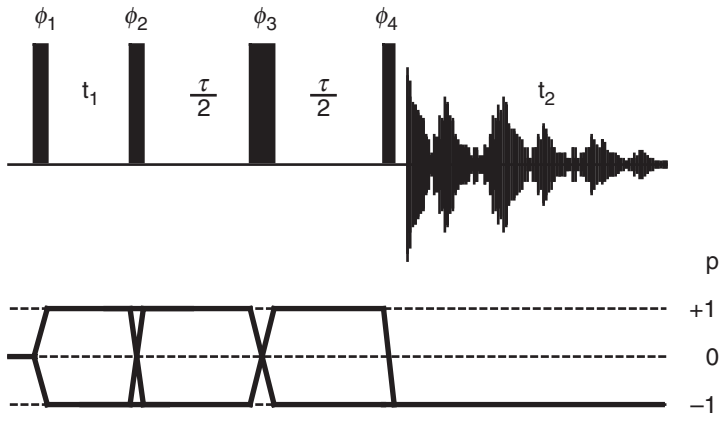

FIGURE 6.16 The pulse sequence and coherence level diagram for the R.COSY experiment. The phases are cycled as follows: $\phi_1 = 4(x, -x)$; $\phi_2 = 4(x)$, $4(-x)$; $\phi_3 = 8(x)$; $\phi_4 = 2(x, x, -x, -x)$; and receiver $= 4(x, -x)$. CYCLOPS is performed on all pulses and the receiver to produce a 32 step cycle. The 180° pulse during the mixing period can be a composite $90^\circ_{\phi 2} - 90^\circ_{\phi 2+\pi/2} - 90^\circ_{\phi 2}$ pulse. Frequency discrimination in F_1 is obtained by shifting the phase of ϕ_1 and the receiver according to the TPPI, States, or TPPI–States protocols (Section 4.3.4).

6.2.2.1 Product Operator Analysis For this analysis, the linear spin system I_1–I_2–I_3 is considered, in which J_{12} and J_{23} are resolved and $J_{13} = 0$. Considering initial I_1 magnetization, the operator terms present after the 90°_x – t_1 – 90°_x sequence are given by [6.1]. The $2I_{1z}I_{2y}$ term of this expression represents transfer of coherence from I_1 to I_2 and is the first step in the generation of an $I_1 \rightarrow I_3$ cross-peak. Appropriate phase cycling preserves this term (and also the I_{1x} single-quantum coherence) and suppresses other coherence orders. During the spin echo $\tau/2$ – 180°_x – $\tau/2$ sequence, chemical shifts are refocused and evolution under the J_{12} and J_{23} scalar coupling Hamiltonians yields the following terms:

$$
\begin{aligned}
&I_{1x}\sin(\Omega_1 t_1)\cos(\pi J_{12} t_1) - 2I_{1z}I_{2y}\sin(\Omega_1 t_1)\sin(\pi J_{12} t_1) \xrightarrow{\tau/2-\pi_x-\tau/2} \\
&\quad \left[I_{1x}\cos(\pi J_{12}\tau) + 2I_{1y}I_{2z}\sin(\pi J_{12}\tau)\right]\sin(\Omega_1 t_1)\cos(\pi J_{12} t_1) \\
&\quad + \left[-2I_{1z}I_{2y}\cos(\pi J_{23}\tau) + 4I_{1z}I_{2x}I_{3z}\sin(\pi J_{23}\tau)\right] \\
&\quad \times \sin(\Omega_1 t_1)\sin(\pi J_{12} t_1)\cos(\pi J_{12}\tau) + [I_{2x}\cos(\pi J_{23}\tau) \\
&\quad + 2I_{2y}I_{3z}\sin(\pi J_{23}\tau)\big]\sin(\Omega_1 t_1)\sin(\pi J_{12} t_1)\sin(\pi J_{12}\tau). \qquad [6.9]
\end{aligned}
$$

Application of the final 90°_x pulse creates the following terms immediately prior to t_2:

$$\begin{aligned}&\left[I_{1x}\cos(\pi J_{12}\tau) - 2I_{1z}I_{2y}\sin(\pi J_{12}\tau)\right]\sin(\Omega_1 t_1)\cos(\pi J_{12}t_1)\\&\quad+\left[2I_{1y}I_{2z}\cos(\pi J_{23}\tau) + 4I_{1y}I_{2x}I_{3y}\sin(\pi J_{23}\tau)\right]\\&\quad\times\sin(\Omega_1 t_1)\sin(\pi J_{12}t_1)\cos(\pi J_{12}\tau)\\&\quad+\left[I_{2x}\cos(\pi J_{23}\tau) - 2I_{2z}I_{3y}\sin(\pi J_{23}\tau)\right]\\&\quad\times\sin(\Omega_1 t_1)\sin(\pi J_{12}t_1)\sin(\pi J_{12}\tau).\end{aligned}\qquad[6.10]$$

Of the six components in [6.10], only the three-spin coherence $4I_{1y}I_{2x}I_{3y}$ is unobservable. The most interesting peak arises by relay from I_1 via I_2 to I_3, and is described by the $2I_{2z}I_{3y}$ term. This peak appears at the I_3 chemical shift and is antiphase with respect to spin I_2 in F_2. It appears at the chemical shift of I_1 in F_1, and the $\sin(\Omega_1 t_1)\sin(\pi J_{12}t_1)$ modulation indicates antiphase lineshape with respect to I_2. In the normal mode of display, relay peaks are phased to be absorptive in both dimensions and this will be assumed in the following discussion of the phases of other peaks.

The I_{1x} and $2I_{1y}I_{2z}$ terms contribute to the I_1 diagonal peak. The former is analogous to the diagonal peak in a normal COSY experiment and has a dispersive in-phase lineshape in both dimensions. The second diagonal component is an absorptive antiphase signal in both dimensions. Thus, as in the regular COSY experiment, the diagonal is dominated by dispersive in-phase terms that must be attenuated by severe window functions.

Finally, the R.COSY spectrum contains cross-peaks between spins that are directly coupled ("COSY"-type peaks). The $2I_{1z}I_{2y}$ and I_{2x} terms of [6.10] contribute to these peaks. The former possesses absorptive antiphase character in F_2 and dispersive in-phase character in F_1, while the latter possesses dispersive in-phase character in F_2 and absorptive antiphase character in F_1. The contribution of each component to the overall lineshape of these peaks is dependent on the length of the mixing period as described by the $\sin(\pi J_{12}\tau)$ and $\cos(\pi J_{23}\tau)\sin(\pi J_{12}\tau)$ trigonometric functions, respectively. These peaks can never be phased to pure absorption lineshapes, and dispersive tails emanate from the COSY peaks in the R.COSY spectrum.

Although the results observed in R.COSY spectra of the larger spin systems found in real amino acids are more complex than the equations just described, the general trends are similar. A more complete description of the transfer functions in particular amino acids has been presented by Bax and Drobny (*20*).

6.2.2.2 Experimental Protocol From the preceding discussion, cancellation of antiphase cross-peaks also must be avoided in R.COSY experiments. In addition to the standard COSY acquisition parameters, a value must be chosen for the mixing delay, τ, during which the second antiphase state develops. In H_2O solution, the most useful peaks appear at the chemical shift of $^1H^{\beta}$ in F_1 and at the chemical shift of $^1H^N$ in F_2 (Section 9.1.1). For such cross-peaks, coherence will be transferred from $^1H^{\beta}$ to $^1H^{\alpha}$ during t_1, and from $^1H^{\alpha}$ to $^1H^N$ during the relay period, i.e., $I_1 = {}^1H^{\beta}$, $I_2 = {}^1H^{\alpha}$, and $I_3 = {}^1H^N$.

Given the preceding discussion, t_{1max} must be long enough to allow transfer via the $^1H^{\alpha}$–$^1H^{\beta}$ coupling [i.e., $t_{1\,max} \geq 1/(2^3J_{H^{\alpha}H^{\beta}})$]. For many residues in folded proteins, at least one $^3J_{H^{\alpha}H^{\beta}}$ coupling will be in the 8- to 12-Hz range. Thus, R.COSY experiments utilize t_{1max} in the range of 40 to 60 ms. For an F_1 spectral width of 5 kHz, 400 to 600 t_1 increments are recorded (assuming quadrature detection with TPPI).

During the mixing time, τ, the antiphase coherence transferred from $^1H^{\beta}$ to $^1H^{\alpha}$ during t_1 must refocus with respect to $^1H^{\beta}$ and defocus with respect to $^1H^N$. Thus, the magnitude of the transfer from $^1H^{\beta}$ to $^1H^N$ depends on both $^3J_{H^NH^{\alpha}}$ and $^3J_{H^{\alpha}H^{\beta}}$. Analytical functions describing the transfer have been calculated for a variety of spin system types using values of coupling constants commonly found in proteins (*20*, *21*). Maxima in the transfer functions occur for $\tau = 40$–60 ms; however, relaxation during τ reduces the intensity of all peaks. Therefore, compromise values of $\tau = 20$–40 ms provide adequate coherence transfer without extensive relaxation losses. Usually, with a 2–4 m*M* sample, adequate $^1H^N$–$^1H^{\beta}$ cross-peak intensities are obtained by acquiring 32 to 64 transients per t_1 increment.

The R.COSY spectrum analyzed below was acquired from a 2 m*M* ubiquitin solution in H_2O. Thirty-two transients were collected for each of 800 increments ($t_{1max} = 69$ ms). A mixing time of 22 ms was used during the relay portion of the experiment (τ). A composite 180° pulse was used to refocus chemical shifts in the middle of τ (Section 3.4.2). The total acquisition time was 14 hr.

6.2.2.3 Processing Given the results of the product operator analysis, processing of R.COSY data is very similar to that used for COSY data. Harsh window functions (unshifted sine bells in F_2 and slightly shifted sine bells in F_1) are required to minimize the dispersive diagonal peaks and COSY-type cross-peaks.

6.2.2.4 Information Content The most interesting cross-peaks in the R.COSY experiment result from two coherence transfer steps.

As a rule, all possible $^1H^{\beta}$–$^1H^N$ cross-peaks in the R.COSY spectrum are not observed, because of the dependence on two coupling constants (either or both of which could be small). However, in side chains containing $C^{\beta}H_2$ groups, at least one of the $^1H^{\alpha}$–$^1H^{\beta}$ couplings is commonly greater than 8 Hz and provides an efficient means of generating one $^1H^{\beta}$–$^1H^N$ cross-peak.

These generalizations are exemplified by the peaks observed in the R.COSY spectrum of ubiquitin. Of the 45 side chains that have an observable backbone amide proton and a β-methylene group, six residues have no $^1H^N$–$^1H^{\beta}$ correlations, 30 (67%) have a single $^1H^N$–$^1H^{\beta}$ correlation, and in only 9 cases (20%) are both $^1H^N$–$^1H^{\beta}$ correlations observed. Also, 11 of the 18 side chains with an amide proton and a single β-proton exhibit an $^1H^N$–$^1H^{\beta}$ cross-peak. Although acquisition of R.COSY spectra with longer mixing times can permit identification of additional $^1H^N$–$^1H^{\beta}$ correlations arising from small $^3J_{H^NH^{\alpha}}$ coupling constants, double-relayed COSY (Section 6.2.3) and TOCSY (Section 6.5) experiments are better suited to detecting such correlations. The section of the R.COSY spectrum shown in Fig. 6.17a depicts several of the relayed $^1H^N$–$^1H^{\beta}$ cross-peaks. The section of the R.COSY spectrum shown in Fig. 6.17b depicts the $^1H^N$–$^1H^{\alpha}$ correlations to emphasize the dispersive nature of the COSY-type peaks in the R.COSY spectrum.

6.2.3 DOUBLE-RELAYED COSY

Additional coherence transfer steps can be obtained by inserting a second $\tau/2$–180°–$\tau/2$–90° sequence prior to t_2 in the R.COSY experiment (*22*). This variant is termed the double-relayed COSY (DR.COSY), and the pulse sequence is shown in Fig. 6.18. The DR.COSY correlates protons through a network of three scalar couplings. In principle, the COSY experiment could be extended indefinitely until correlations are observed between all spins in a particular spin system. However, inefficient coherence transfer and relaxation during the periods of free precession reduce the sensitivity to such an extent that the DR.COSY represents the practical limit of such experiments.

Set up for DR.COSY contains essentially the same considerations as for the R.COSY, except that values must be selected for both τ_2 and τ_1. The most useful peaks will be transferred through three couplings to $^1H^N$. Instead of optimizing the transfer from $^1H^{\gamma}$ to $^1H^N$, the most effective results are obtained by transfer from $^1H^{\beta'}$ to $^1H^{\beta''}$ during t_1 (via the large $^1H^{\beta'}$–$^1H^{\beta''}$ coupling), $^1H^{\beta''}$ to $^1H^{\alpha}$ during τ_1 (via the largest of the two possible $^1H^{\beta}$–$^1H^{\alpha}$ couplings), and from $^1H^{\alpha}$ to $^1H^N$ during τ_2. In this way, relatively intense cross-peaks are obtained to both $^1H^{\beta}$ protons,

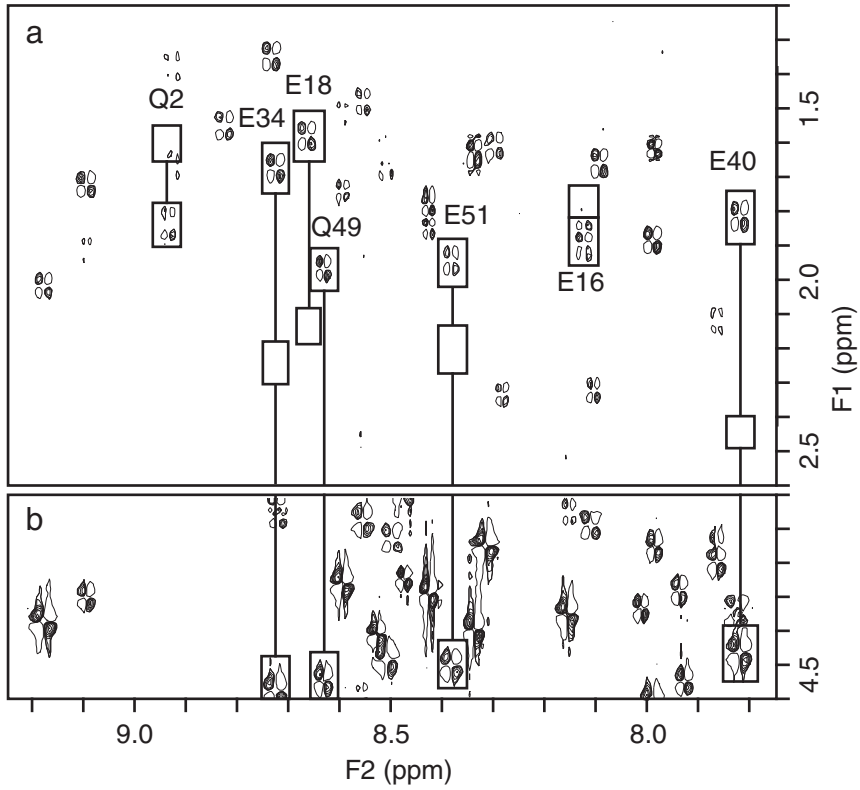

FIGURE 6.17 Two sections of an R.COSY spectrum ($\tau = 22$ ms) of ubiquitin in H_2O solution showing (a) $^1H^N$–$^1H^\beta$ and (b) $^1H^N$–$^1H^\alpha$ correlations. The glutamate and glutamine resonances in the depicted region are surrounded by rectangles. Note that only one of the possible $^1H^N$–$^1H^\beta$ correlations has appreciable intensity and that many of the $^1H^N$–$^1H^\alpha$ COSY-type peaks have distinct dispersive tails.

and DR.COSY represents a significant improvement over R.COSY, in which correlations usually are observed to only one $^1H^\beta$.

Although a product operator analysis is not explicitly presented here for the DR.COSY, important results are obtained by analogy with the R.COSY sequence. Double-relay cross-peaks are absorptive antiphase in both dimensions, whereas COSY and single-relay peaks contain some in-phase dispersive contributions. Choices of mixing time to optimize the intensity of various correlations have been determined by calculating the cross-peak intensities as a function of τ_2 and τ_1 for a variety of possible coupling constants and spin systems (*21*). Setting the delays $\tau_1 = 28$ ms

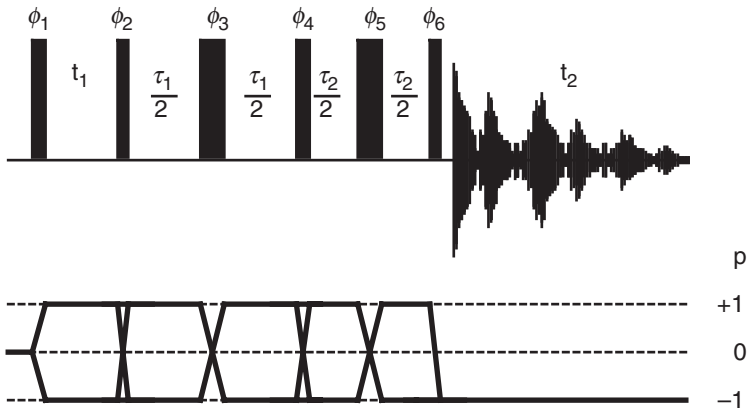

FIGURE 6.18 Pulse sequence and coherence level diagram for the DR.COSY experiment. The 180° pulses can be replaced with composite pulses as described in Fig. 6.16. The phases are cycled as follows: $\phi_1 = 8(x, -x)$; $\phi_2 = 8(x), 8(-x)$; $\phi_3 = 16(x)$; $\phi_4 = 4(x), 4(-x), 4(x), 4(-x)$; $\phi_5 = 16(x)$; $\phi_6 = 4(x, x, -x, -x)$; and receiver $= 8(x, -x)$. CYCLOPS is performed on all pulses to yield a 64-step phase cycle. Frequency discrimination in F_1 is obtained by shifting the phase of ϕ_1 and the receiver according to the TPPI, States, or TPPI–States protocols (Section 4.3.4).

and $\tau_2 = 35$ ms maximizes the $^1H^{\beta'}$–$^1H^{\beta''}$–$^1H^{\alpha}$–$^1H^N$ transfer. Transfer during t_1 is via the large 15-Hz $^1H^{\beta'}$–$^1H^{\beta''}$ coupling, so t_{1max} can be slightly shorter than in the R.COSY; however, the cross-peaks are still antiphase, and subject to self-cancellation if t_{1max} is too short. Alternatively, setting the delays $\tau_1 = 20$ ms and $\tau_2 = 31$ ms will maximize transfer from $^1H^{\gamma}$ to $^1H^N$ (*21, 23*). Total acquisition times usually need to be longer than for R.COSY because the most interesting correlations result from three transfer steps. Forty-eight-hour acquisitions are not uncommon in the literature for this experiment. Processing is analogous to that used in COSY and R.COSY experiments (Sections 6.2.1.3 and 6.3.1.3).

The spectrum depicted in Fig. 6.19 was acquired from an H_2O solution of ubiquitin. Sixty-four transients were collected for each of 576 increments in t_1, with a $t_{1max} = 50$ ms and a total acquisition time of 21 hr. The mixing times τ_1 and τ_2 were set to 28 and 35 ms, respectively, to emphasize H^{β}–H^N correlations, and composite 180° pulses were used in the middle of both delays (Section 3.4.2).

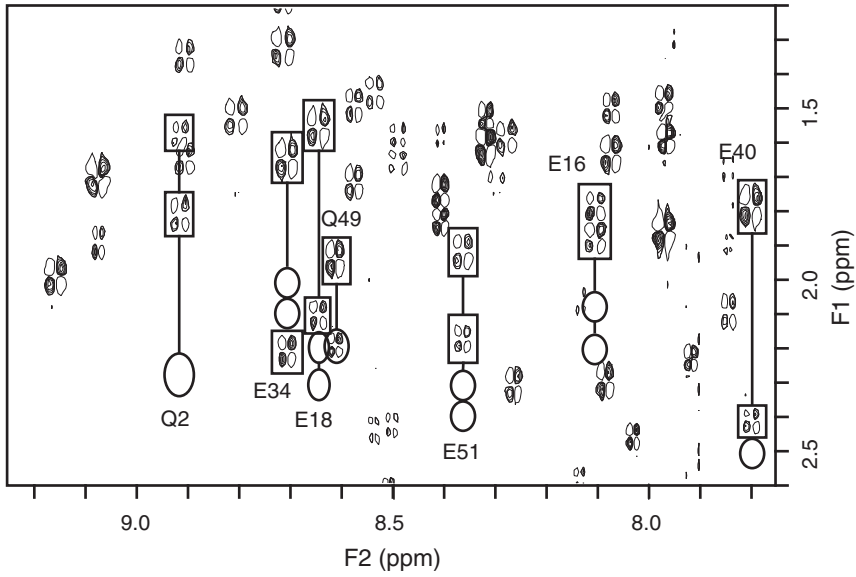

FIGURE 6.19 Section of a DR.COSY spectrum ($\tau_1 = 28$ ms, $\tau_2 = 35$ ms) of ubiquitin acquired from H_2O solution. The same spectral region as in the top of Fig. 6.17 is shown, with glutamine and glutamate $^1H^{\beta}$ and $^1H^{\gamma}$ resonance positions denoted by the rectangles and ellipses, respectively. The particular delays used during the relay periods have optimized transfer of both $^1H^{\beta}$ to $^1H^N$ at the expense of $^1H^{\gamma}$–$^1H^N$ correlations.

Figure 6.19 depicts a region of the DR.COSY in which several correlations from both protons of β-methylene groups are observed to the backbone amide proton. In the equivalent region of the R.COSY, only one of the correlations is observed (compare with Fig. 6.17). Correlations from $^1H^{\gamma}$ to $^1H^N$ are absent for the glutamine and glutamate side chains identified in Fig. 6.19. In the spectrum as a whole, with mixing times $\tau_1 = 28$ ms and $\tau_2 = 35$ ms, correlations from $^1H^{\beta''}$ and $^1H^{\beta'}$ to $^1H^N$ are observed in 39 (87%) of the 45 residues with a β-methylene group. Of these side chains, 31 also contained γ-protons, but in only three cases were $^1H^{\gamma}$–$^1H^N$ correlations observed (both $^1H^{\beta}$–$^1H^N$ correlations were also observed for these three cases). For side chains containing a single β-proton, more $^1H^N$–$^1H^{\beta}$ correlations were observed in the DR.COSY than in the R.COSY experiment (14 out of 18, compared to 11 out of 18), and 13 correlations from $^1H^N$ to at least one $^1H^{\gamma}$ were observed.

6.3 Multiple-Quantum Filtered COSY

The double-quantum filtered (2QF)-COSY experiment was developed by the Ernst and Freeman laboratories as an alternative to COSY (*24–26*). The 2QF-COSY is actually the simplest version of a family of experiments based on filtration through a p-quantum state. Not all amino acid spin systems are capable of achieving some of the higher quantum states; hence, experiments with $p > 2$ provide useful spectral simplification (*27*).

All pQF-COSY experiments that use phase cycling for coherence selection have the same basic pulse sequence consisting of three 90° pulses, with the first two separated by t_1 and the last two separated by a short delay, as shown in Fig. 6.20. As described in Section 4.3.2.1, phase cycling is used to cancel all but the particular coherence level of interest.

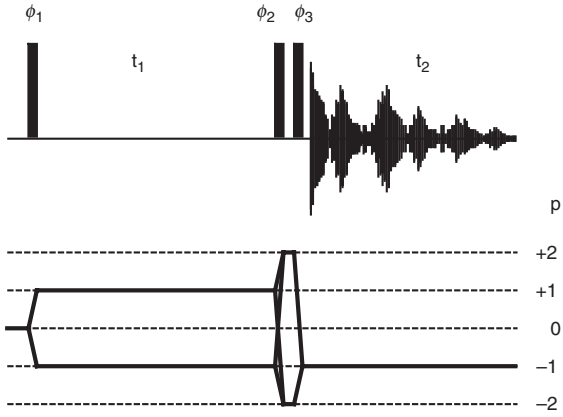

FIGURE 6.20 Pulse sequence and coherence level diagram for a 2QF-COSY experiment. The basic four-step phase cycle for 2QF-COSY is $\phi_1 = \phi_2 = x, y, -x, -y$; $\phi_3 = x$; and receiver $= 2(x, -x)$. The same pulse sequence is used for 3QF-COSY with the following basic six-step phase cycle: $\phi_1 = \phi_2 = 0°, 60°, 120°, 180°, 240°, 300°$; $\phi_3 = 0°$; and receiver $= 3(0°, 180°)$. Axial peak suppression and CYCLOPS phase cycling yields a 32-step phase cycle for 2QF-COSY and 48-step phase cycle for 3QF-COSY. An improved phase cycle for the 2QF-COSY that suppresses rapid pulsing artifacts is $\phi_1 = 4(y), 4(-y)$; $\phi_2 = 4(x), 4(-x)$; $\phi_3 = (y, -x, -y, x, -x, -y, x, y)$; and receiver $= (x, -y, -x, y, -y, -x, y, x)$ (*32, 33*). Frequency discrimination in F_1 is obtained by shifting the phase of ϕ_1 and the receiver according to the TPPI, States, or TPPI–States protocols (Section 4.3.4).

Selection of a desired order of multiple-quantum filtration is achieved by incrementing the phases of the pulses as follows:

$$\begin{array}{lll} \phi_1 \text{ and } \phi_2: & & n\pi/p \\ \phi_3: & & 0 \\ \text{receiver:} & & -n\pi \end{array} \qquad [6.11]$$

In [6.11], the integer n is incremented from 0 to $2p-1$; thus, the basic phase cycle consists of $2p$ steps. Note that for $p > 2$, appropriate selection involves phase shift increments of less than 90°, hence the $x, y, -x, -y$ notation is no longer appropriate to describe the phases. Such shifts are readily accomplished with the digital phase-shifting hardware present on modern spectrometers. Alternative cycles involving phase shifting of ϕ_3 also can be used to obtain the desired coherence selection. Formally, these phase cycles retain coherence orders kp, where $k = \pm 1, \pm 3, \pm 5, \ldots$, but the higher order coherences have low intensity (see later). In addition to the basic $2p$ cycle, artifacts in the spectra are reduced by performing CYCLOPS on all pulses and axial peak suppression on the first pulse (Section 4.3.2.3), leading to $16p$ steps in the cycle.

A number of approaches have been developed for incorporating coherence selection using pulsed field gradients into the *p*QF-COSY experiment. In the approach shown in Fig. 6.21, the basic pulse sequence incorporates short spin echo periods to allow the application of gradient pulses during the multiple-quantum filter and prior to acquisition (*28, 29*). As discussed in Section 4.3.3.1, filtration for signed coherence order p is obtained by requiring that the coherence transfer $p \rightarrow -1$ is selected by the gradient pair. Assuming that the gradient pulses have the same duration and amplitudes G1 and G2, respectively, the filter requires that

$$\text{G2} = p\text{G1}. \qquad [6.12]$$

Thus, for example, a +2 quantum filter is obtained by setting G2 = 2G1. Phase cycling is not necessary for coherence selection and the only phase cycling utilized is for artifact suppression using CYCLOPS or EXORCYCLE (Section 4.3.2.3). The gradient-selected *p*QF-COSY experiment has the principal disadvantage of being a factor of two less sensitive than the phase-cycled experiment because only the coherence order p_1 and not $-p$, can be transferred to detectable

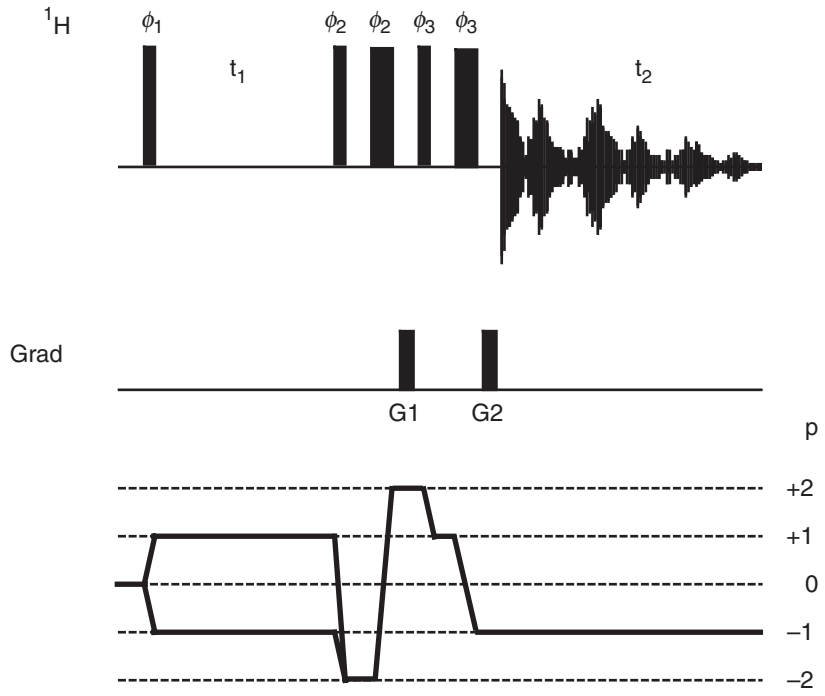

FIGURE 6.21 Pulse sequence and coherence level diagram for a gradient-enhanced 2QF-COSY experiment. The gradient pair satisfy the relationship $G2 = pG1$ to select the signed coherence level $p = +2$ The basic four-step phase cycle for 2QF-COSY is $\phi_1 = 4(y), 4(x)$; $\phi_2 = 4(x), 4(y)$; $\phi_3 = y, -x, -y, x, -x, -y, x, y$; and receiver $= x, -y, -x, y, -y, -x, y, x$. Frequency discrimination in F_1 is obtained by shifting the phase of ϕ_1 and the receiver according to the TPPI, States, or TPPI–States protocols (Section 4.3.4). A bipolar pair of gradients can be inserted into the t_1 period to prevent radiation damping (*31*).

magnetization. In addition, the gradient-selected experiment is slightly longer, allowing additional relaxation losses and unwanted evolution of scalar coupling interactions. These disadvantages are outweighed by the high degree of filtration that is obtained by gradient selection. In particular, when magic-angle field gradient pulses are utilized (Section 4.3.3), very high-quality water suppression can be obtained without presaturation of the solvent resonance (*28*, *30*).

If the water signal is not suppressed prior to the t_1 evolution period, then the full water ^{1}H magnetization is in the transverse plane at the

start of t_1. Difficulties will arise because the consequent radiation damping of the water ^1H magnetization will have the effect of a selective rf pulse coincident with the water resonance frequency. Thereby, radiation damping will result in undesirable perturbations of protein resonances that are (nearly) degenerate with the water resonance. These perturbations can have the form of phase distortion and/or signal attenuation of the affected resonances. These difficulties are avoided if significant radiation damping is prevented from occurring during t_1. An effective solution with general applicability was proposed by Sklenář and consists of the application of a pair of bipolar gradient pulses during the t_1 period (*31*). The first gradient pulse, applied at the beginning of the t_1 period, defocuses the magnetization and therefore severely attenuates the effect of radiation damping. A second gradient pulse, of equal strength but opposite polarity, is then applied at the end of the t_1 period in order to refocus the ^1H magnetization. In the event that the evolution period contains rf pulses for some purpose, the polarity and exact positioning of the defocusing/refocusing gradient pulses may need to be modified. Careful attention to the trajectory of the water magnetization is essential for the execution of any NMR experiment performed on a sample in H_2O solution.

6.3.1 2QF-COSY

As noted previously, one of the major shortcomings of the COSY experiment is the 90° phase difference between the diagonal and cross-peaks, leading to a dispersive diagonal in the usual mode of presentation. The intense, sprawling nature of the diagonal, particularly for uncoupled singlet resonances, distorts and obscures cross-peaks close to the diagonal. The double-quantum filtered COSY experiment overcomes some of the drawbacks of COSY (*24*, *2452.52)m41.i495,4a130m70*

superposition of double-quantum and zero-quantum coherence and can be expanded accordingly as (see Section 2.7.5),

$$\begin{aligned}
&-(1/2)[2I_{1x}I_{2y} + 2I_{1y}I_{2x} + 2I_{1x}I_{2y} - 2I_{1y}I_{2x}]\cos(\Omega_1 t_1)\sin(\pi J_{12} t_1) \\
&\quad = -(1/2i)[I_1^+ I_2^+ - I_1^- I_2^- - I_1^+ I_2^- + I_1^- I_2^+]\cos(\Omega_1 t_1)\sin(\pi J_{12} t_1) \\
&\quad = -[\mathrm{DQ}_y - \mathrm{ZQ}_y]\cos(\Omega_1 t_1)\sin(\pi J_{12} t_1). \qquad [6.13]
\end{aligned}$$

In the phase-cycled 2QF-COSY, the double-quantum coherence $\mathrm{DQ}_y = (1/2)(2I_{1x}I_{2y} + 2I_{1y}I_{2x})$ is selected by the phase cycle. The zero-quantum coherence $\mathrm{ZQ}_y = (1/2)(2I_{1y}I_{2x} - 2I_{1x}I_{2y})$ is rejected by the phase cycle. The final 90°_x pulse generates the following observable single-quantum coherence terms:

$$\begin{aligned}
&-(\tfrac{1}{2})[2I_{1x}I_{2y} + 2I_{1y}I_{2x}]\cos(\Omega_1 t_1)\sin(\pi J_{12} t_1) \\
&\xrightarrow{(\frac{\pi}{2})_x} -(\tfrac{1}{2})[2I_{1x}I_{2z} + 2I_{1z}I_{2x}]\cos(\Omega_1 t_1)\sin(\pi J_{12} t_1). \qquad [6.14]
\end{aligned}$$

In the gradient-selected 2QF-COSY, only the double-quantum coherence $I_1^+ I_2^+ = (1/2)[2I_{1x}I_{2x} + 2I_{1y}I_{2y} + i(2I_{1x}I_{2y} + 2I_{1y}I_{2x})]$ is selected by the gradient pair G1 and G2. Only the terms $2I_{1x}I_{2y}$ and $2I_{1y}I_{2x}$ are converted to observable single-quantum coherences by the final 90°_x pulse:

$$\begin{aligned}
&-(\tfrac{1}{4})[2I_{1x}I_{2y} + 2I_{1y}I_{2x}]\cos(\Omega_1 t_1)\sin(\pi J_{12} t_1) \\
&\xrightarrow{(\frac{\pi}{2})_x} -(\tfrac{1}{4})[2I_{1x}I_{2z} + 2I_{1z}I_{2x}]\cos(\Omega_1 t_1)\sin(\pi J_{12} t_1). \qquad [6.15]
\end{aligned}$$

The terms $2I_{1x}I_{2x}$ and $2I_{1y}I_{2y}$ result in undetectable multiple-quantum and longitudinal two-spin order after the final 90°_x pulse. As indicated by the prefactors in [6.14] and [6.15], the sensitivity of the gradient-selected experiment is reduced by a factor of two compared to the phase-cycled experiment, but otherwise, the signal obtained is identical (neglecting evolution and relaxation during the spin echo periods of the gradient-selected experiment).

Simple inspection shows that the $2I_{1x}I_{2z}$ product operator evolves at the chemical shift of the I spin and is antiphase with respect to the scalar coupling during t_2. The $2I_{1z}I_{2x}$ product operator evolves at the chemical shift of the I_2 spin and is antiphase with respect to the scalar coupling during t_2. Because both terms evolve with a frequency of Ω_1 during t_1, the former represents an I_1 spin diagonal peak, and the latter represents

an $I_1 \rightarrow I_2$ cross-peak. The diagonal and cross-peak terms have the same phase in F_2 (both terms contain x-operators) and are modulated by the same t_1 trigonometric terms; expansion of the trigonometric coefficients indicates that both the diagonal and the cross-peaks are antiphase in the F_1 dimension. Consequently, the diagonal and cross-peaks in a 2QF-COSY spectrum can be phased to pure absorption in both dimensions. Thereby, the 2QF-COSY experiment eliminates problems associated with dispersive tails emanating from the diagonal resonances in COSY spectra. This attribute influences the processing and extraction of information from 2QF-COSY spectra.

Consideration of the evolution of a three-spin system during a 2QF-COSY is useful at this point to reveal further features of the spectrum. The system now contains three spins, I_1, I_2, and I_3, with couplings J_{12}, J_{13}, and J_{23}. Evolution of initial $-I_{1y}$ magnetization under the chemical shift, J_{12} scalar coupling, and J_{13} scalar coupling Hamiltonians lead to the following antiphase terms:

$$
\begin{aligned}
I_z &\xrightarrow{(\frac{\pi}{2})_x} -I_{1y} \\
&\xrightarrow{t_1} 2I_{1x}I_{2z}\cos(\Omega_1 t_1)\sin(\pi J_{12}t_1)\cos(\pi J_{13}t_1) \\
&\quad + 2I_{1y}I_{2z}\sin(\Omega_1 t_1)\sin(\pi J_{12}t_1)\cos(\pi J_{13}t_1) \\
&\quad + 2I_{1x}I_{3z}\cos(\Omega_1 t_1)\cos(\pi J_{12}t_1)\sin(\pi J_{13}t_1) \\
&\quad + 2I_{1y}I_{3z}\sin(\Omega_1 t_1)\cos(\pi J_{12}t_1)\sin(\pi J_{13}t_1) \\
&\quad + 4I_{1y}I_{2z}I_{3z}\cos(\Omega_1 t_1)\sin(\pi J_{12}t_1)\sin(\pi J_{13}t_1) \\
&\quad - 4I_{1x}I_{2z}I_{3z}\sin(\Omega_1 t_1)\sin(\pi J_{12}t_1)\sin(\pi J_{13}t_1) \qquad [6.16] \\
&\xrightarrow{(\frac{\pi}{2})_x} -2I_{1x}I_{2y}\cos(\Omega_1 t_1)\sin(\pi J_{12}t_1)\cos(\pi J_{13}t_1). \\
&\quad - 2I_{1z}I_{2y}\sin(\Omega_1 t_1)\sin(\pi J_{12}t_1)\cos(\pi J_{13}t_1) \\
&\quad - 2I_{1x}I_{3y}\cos(\Omega_1 t_1)\cos(\pi J_{12}t_1)\sin(\pi J_{13}t_1) \\
&\quad - 2I_{1z}I_{3y}\sin(\Omega_1 t_1)\cos(\pi J_{12}t_1)\sin(\pi J_{13}t_1) \\
&\quad + 4I_{1z}I_{2y}I_{3y}\cos(\Omega_1 t_1)\sin(\pi J_{12}t_1)\sin(\pi J_{13}t_1) \\
&\quad - 4I_{1x}I_{2y}I_{3y}\sin(\Omega_1 t_1)\sin(\pi J_{12}t_1)\sin(\pi J_{13}t_1).
\end{aligned}
$$

The resulting $2I_{1z}I_{2y}$ and $2I_{1z}I_{3y}$ terms of [6.16] describe antiphase single-quantum coherence and will be rejected by the phase cycling. Similarly, the $4I_{1x}I_{2y}I_{3y}$ term describes a mixture of 3Q and three-spin single-quantum coherences and will also be rejected (this term is discussed in more detail with respect to the 3QF-COSY in Section 6.3.2.1). The other

resulting terms of [6.16] contain mixtures of ZQ and DQ coherences (Section 2.7.5) and can be rewritten as

$$\begin{aligned} -2I_{1x}I_{2y} &= -\tfrac{1}{2}\left[2I_{1x}I_{2y} + 2I_{1y}I_{2x} - 2I_{1y}I_{2x} + 2I_{1x}I_{2y}\right] \\ &= -\tfrac{1}{2i}\left[I_1^+I_2^+ - I_1^-I_2^- - I_1^+I_2^- + I_1^-I_2^+\right] \\ &= -\left[\mathrm{DQ}_y^{12} - \mathrm{ZQ}_y^{12}\right], \end{aligned} \qquad [6.17]$$

$$\begin{aligned} -2I_{1x}I_{3y} &= -\tfrac{1}{2}\left[2I_{1x}I_{3y} + 2I_{1y}I_{3x} - 2I_{1y}I_{3x} + 2I_{1x}I_{3y}\right] \\ &= -\tfrac{1}{2i}\left[I_1^+I_3^+ - I_1^-I_3^- - I_1^+I_3^- + I_1^-I_3^+\right] \\ &= -\left[\mathrm{DQ}_y^{13} - \mathrm{ZQ}_y^{13}\right], \end{aligned} \qquad [6.18]$$

$$\begin{aligned} 4I_{1z}I_{2y}I_{3y} &= I_{1z}\left[2I_{2y}I_{3y} - 2I_{2x}I_{3x} + 2I_{2x}I_{3x} + 2I_{2y}I_{3y}\right] \\ &= -I_{1z}\left[I_1^+I_2^+ + I_1^-I_2^- - I_1^+I_2^- - I_1^-I_2^+\right] \\ &= -2I_{1z}\left[\mathrm{DQ}_x^{23} - \mathrm{ZQ}_x^{23}\right], \end{aligned} \qquad [6.19]$$

in which ZQ_p^{ij} and DQ_p^{ij} indicate zero-quantum coherence and double-quantum coherence, respectively, of phase p (x or y) between spins I_i and I_j. The DQ_x^{23} operator is antiphase with respect to I_1.

In the phase-cycled 2QF-COSY, only the DQ_p^{ij} coherences in [6.17]–[6.19] are retained by the phase cycling. The final 90_x° pulse will transfer the DQ terms back to observable magnetization to yield

$$\begin{aligned} &-\tfrac{1}{2}\cos(\Omega_1 t_1)\,\sin(\pi J_{12}t_1)\,\cos(\pi J_{13}t_1)[2I_{1x}I_{2z} + 2I_{1z}I_{2x}], \\ &-\tfrac{1}{2}\cos(\Omega_1 t_1)\,\cos(\pi J_{12}t_1)\,\sin(\pi J_{13}t_1)[2I_{1x}I_{3z} + 2I_{1z}I_{3x}], \\ &+\tfrac{1}{2}\cos(\Omega_1 t_1)\,\sin(\pi J_{12}t_1)\,\sin(\pi J_{13}t_1)\left[4I_{1y}I_{2x}I_{3x} - 4I_{1y}I_{2z}I_{3z}\right]. \end{aligned} \qquad [6.20]$$

In the gradient-selected 2QF-COSY, only the double-quantum coherences $I_i^+I_j^+$ and $2I_{kz}I_i^+I_j^+$ in [6.17]–[6.19] are selected by the gradient pair G1 and G2. After the final 90_x° pulse, the observable coherences are given by [6.20] scaled, as noted previously, by a factor of two due to the gradient coherence selection.

The two terms in the first line of [6.20] describe an I_1 diagonal peak and an $I_1 \rightarrow I_2$ cross-peak; both have antiphase character and are of the same relative phase, as discussed for [6.16]. Similarly, the terms on line 2 describe an I_1 diagonal peak, and an $I_1 \rightarrow I_3$ cross-peak. The $\cos(\pi J t_1)$ trigonometric terms in the first two lines indicate additional in-phase splittings in F_1 arising from passive coupling (see also Section 6.2.1.1); similar splittings will also be present in F_2. The first term on line 3 is

unobservable, while the second term is a third I_1 diagonal component doubly antiphase with respect to I_2 and I_3. When the cross-peaks are phased to absorption, the doubly antiphase term will be in dispersion. Fortunately, the antiphase nature of this term leads to pronounced self-cancellation, hence the dispersive tails will not extend far from the diagonal. In conclusion, this analysis has demonstrated that, even in more complex spin systems, the diagonal resonances of the 2QF-COSY experiment have predominantly in-phase absorption lineshapes and do not obscure cross-peaks between protons close in chemical shift.

6.3.1.2 Experimental Protocol The cross-peaks in the COSY and 2QF-COSY experiments have similar lineshape properties. Thus, many experimental requirements for the 2QF-COSY, notably high digital resolution in F_1 and F_2, are similar to those already described for the COSY experiment. The only extra parameter required in the experimental protocol for the phase-cycled experiments is the delay between the two final 90° pulses. This delay should be on the order of a few microseconds, i.e., as short as possible, while still allowing the rf hardware to make accurate phase shifts of the pulses. In the gradient-selected experiments, the gradient durations and strengths are chosen to obtain satisfactory coherence selection and water suppression. The spin echo delays are chosen to be long enough to encompass the gradients and gradient recovery periods. If three-axis pulsed field gradients are available, then the gradient strengths are adjusted to yield a magic-angle gradient pulse (Section 4.3.3).

When 2QF-COSY experiments are acquired from D_2O solution, the digital resolution in F_1 is improved by reducing the spectral width to span only the aliphatic resonances. Because correlations between the aromatic and aliphatic portions of the spectrum are not observed, folding of the diagonal and cross-peaks of the aromatic resonances does not confuse analysis of the F_1 chemical shifts (Section 4.3.4.3). By reducing the spectral width, a high $t_{1\max}$ is obtained with fewer increments of t_1.

One artifact common in 2QF-COSY spectra results from incomplete recovery of the spins during the recycle delay and gives rise to extra diagonal peaks at $F_1 = 2F_2$ (in this case F_1 and F_2 refer to absolute frequencies from the carrier position, not chemical shifts) (*32*, *33*). Figure 6.22 depicts a region of a spectrum acquired with a short recycle delay (1.33 s) where such artifacts are particularly prominent. Due to the particular spectral widths and carrier position in this spectrum, the artifact peaks occur at $F_1\,(\text{ppm}) = 2 \times F_2\,(\text{ppm}) - 5.6$ for F_2 between 5.6 and 2.6 ppm; due to folding, above $F_2\,(\text{ppm}) = 2.6$ they occur at

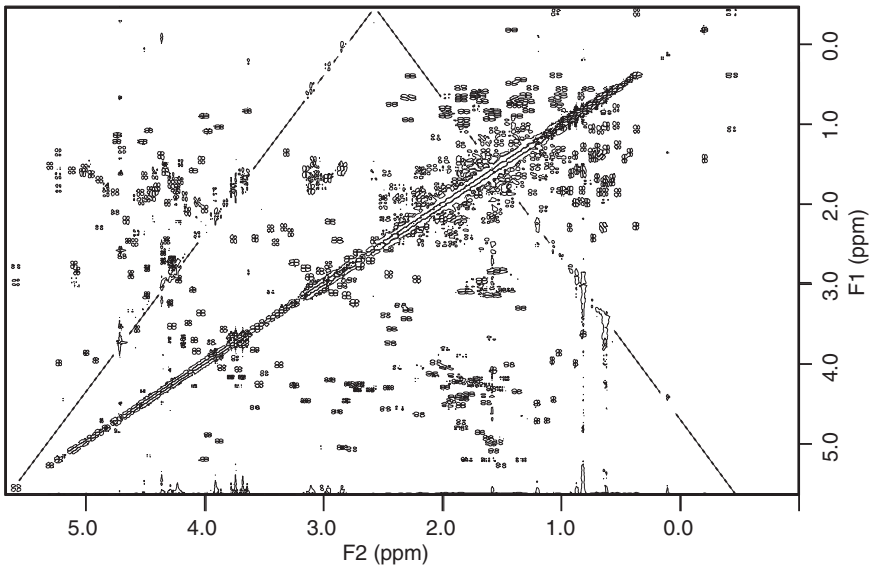

FIGURE 6.22 A 2QF-COSY spectrum acquired with a short recycle delay. The "double diagonal" artifacts lie along the dotted line. Quadrature detection in F_1 was achieved with TPPI; consequently, above 2.6 ppm, the artifact peaks fold to $F_1 = 4.8 - 2F_2$. The spectrum was acquired using the pulse sequence of Fig. 6.20 (16-step phase cycle) with 32 scans for each of 512 increments and with a total recycle delay of 1.33 s (0.33-s acquisition time and 1-s weak presaturation).

$F_1\,(\text{ppm}) = 4.8 - 2 \times F_2\,(\text{ppm})$. In particular, the artifacts obscure weak peaks in the $^1H^{\alpha}$–$^1H^{\beta}$ fingerprint region (Fig. 6.23, panel a). Lengthening the recycle delay (panel b) and the incorporation of axial peak suppression in the phase cycle (panel c) reduces the size of these artifacts and allows several weak proline $^1H^{\delta}$–$^1H^{\gamma}$ cross-peaks to be identified.

Derome and Williamson (*32*) and Turner (*33*) have provided detailed analyses of the origins of the rapid-pulsing artifacts in 2QF-COSY spectra such as that shown in Fig. 6.22, and have derived modified phase-cycling schemes that can be very effective in suppressing these artifacts. One such modified, eight-step phase cycle is given in the caption to Fig. 6.20.

6.3.1.3 Processing Although the cross-peaks of the 2QF-COSY are similar to those of the COSY experiment, processing requirements are usually quite different. Strongly resolution-enhancing window functions

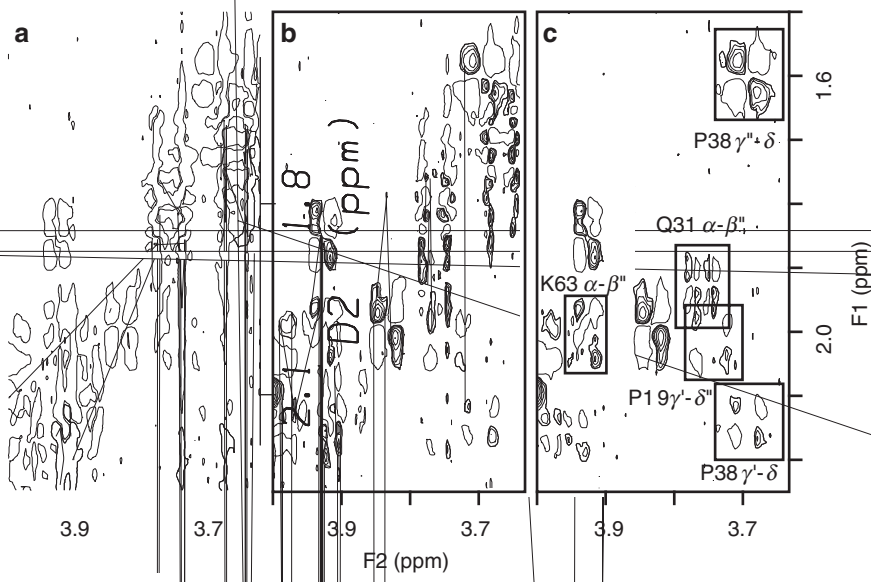

FIGURE 6.23 Cross-peaks obscured by the "double diagonal" artifacts. (a) Enlargement of the spectrum shown in Fig. 6.22. The spectra in b and c were obtained with a longer total recycle delay (2.3 s) and the phase cycle for panel c included axial peak suppression. Other acquisition and processing parameters were the same for all three spectra. Assignments for two of the obscured cross-peaks are included in panel c.

are not required to reduce the intensity of the predominantly antiphase absorptive diagonal peaks. Nonetheless, the appearance of the spectrum is improved by using mild resolution enhancement to minimize overlap of neighboring cross-peaks. Sine bells shifted by 90° to 30° in both t_1 and t_2 are appropriate window functions. The sine bells should span between 150 and 300 ms of each FID (depending on the degree of resolution required and the S/N ratio of the data) and over the entire t_1 interferogram. Phase parameters are determined by the methods already described for the COSY experiment. All of the D_2O 2QF-COSY spectra depicted in this chapter were processed with a sine bell shifted 60° in t_2 with a t_{2max} of 256 ms, and a sine bell shifted 45° over all 512 t_1 points.

6.3.1.4 Information Content The 2QF-COSY contains essentially the same information as does the normal COSY experiment. The regions of interest in the 2QF-COSY experiment are still the fingerprint regions described in Fig. 6.6.

A disadvantage of using the double-quantum filter is a decrease in signal-to-noise ratio by a theoretical factor of two for the phase-cycled 2QF-COSY and a factor of four for the gradient-selected 2QF-COSY relative to the COSY experiment (*25*). The origin of the twofold reduction in sensitivity between the phase-cycled and gradient-selected 2QF-COSY experiments is evident from [6.14] and [6.15]. The origin of the decreased sensitivity for the phase-cycled 2QF-COSY compared to the COSY experiment can be appreciated by considering the first four steps of the phase cycle:

$$\begin{array}{lrrrr} \phi_1: & x, & y, & -x, & -y \\ \phi_2: & x, & y, & -x, & -y \\ \phi_3: & x, & x, & x, & x \\ \text{receiver:} & x, & -x, & x, & -x \end{array}$$

Because the final two pulses of the experiment are contiguous, the first and third transients have a 180° pulse, or 0° pulse, respectively, after t_1; these transients suppress the in-phase dispersive diagonal components and add noise to the spectrum but do not contribute any intensity to the cross-peaks (*15*). Thus, only half of the transients in the phase-cycled 2QF-COSY experiment contribute to cross-peak intensity, leading to a twofold decrease in sensitivity relative to a COSY experiment acquired in the same amount of time. The difference in sensitivity is demonstrated in Fig. 6.24, which shows cross-sections through H_2O COSY and phase-cycled 2QF-COSY spectra at the F_1 chemical shift of the $^1H^{\alpha}$ resonance of Ile13. The absolute magnitudes of the cross-peaks are similar, as the H_2O COSY was acquired with 16 scans per t_1 increment while the 2QF-COSY spectra was acquired with 32 scans per t_1 increment; all other acquisition and processing parameters are identical, with a sine bell shifted by 20° being necessary to prevent the tails of diagonal peaks from interfering with the COSY cross-peaks. Although doubling the number of transients in the 2QF-COSY experiment equalizes the signal height, the root-mean-square (RMS) noise also increases by a factor of $2^{1/2}$, hence the actual S/N ratio is lower than for the COSY experiment.

The difference in sensitivity for 2QF-COSY and COSY experiments is observed if both spectra are recorded and processed in exactly the same way. In practice, however, the more severe window functions used for processing COSY spectra reduce the sensitivity of the experiment. Thus, in Fig. 6.24 the top trace depicts a row of data from the 2QF-COSY spectrum reprocessed with sine bells shifted 60° and 90° in t_2 and t_1, respectively. The S/N ratio is now 1.3-fold higher than in the COSY spectrum. As a caveat, the severe window functions used with COSY

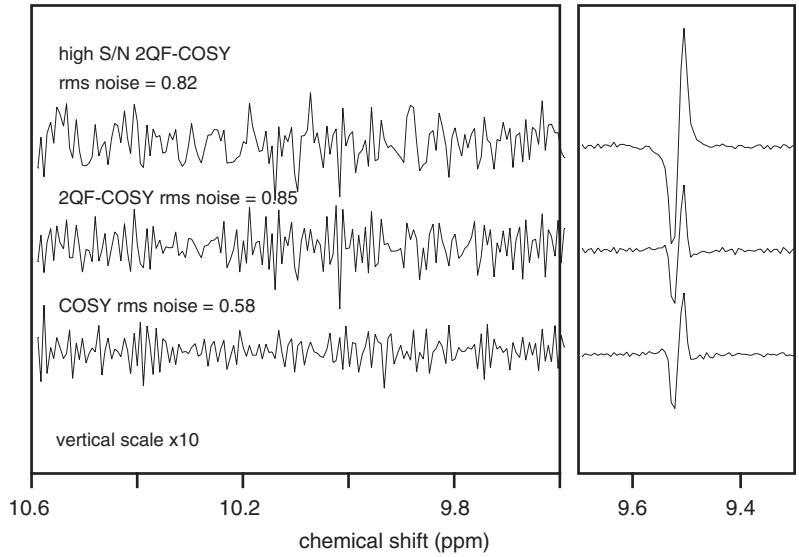

FIGURE 6.24 Comparison of the S/N ratio in COSY and 2QF-COSY spectra for the $^1H^N$–$^1H^\alpha$ cross-peak of Ile13. Except for the number of transients (COSY = 16, 2QF-COSY = 32), both spectra were acquired under identical conditions. The two lower traces were also processed identically (sine bell shifted 20° in t_1 and an unshifted sine bell in t_2), whereas the top trace was processed with less resolution-enhancing window functions (a cosine bell in t_1 and a sine bell shifted 60° in t_2). See text for a more detailed description.

spectra also are resolution enhancing, so although the final COSY and 2QF-COSY experiments can have similar signal-to-noise ratios, the resolution in the COSY will be higher.

A useful strategy for the study of proteins employs the COSY experiment in H_2O solution to observe $^1H^N$–$^1H^\alpha$ cross-peaks that are far from the diagonal, and uses the 2QF-COSY in D_2O solution to identify cross-peaks in the vicinity of the diagonal. Even though harsh window functions can be used to observe peaks close to the diagonal in COSY spectra, distortions arise and the peaks are more readily observed in the 2QF experiment (Fig. 6.25).

The gradient-selected 2QF-COSY experiment has the advantage over phase-cycled COSY and 2QF-COSY experiments that presaturation of the solvent signal is not necessary. As a consequence, cross-peaks near the water resonance can be observed. Figure 6.26 shows an identical region as shown for the pre-TOCSY COSY spectrum in Fig. 6.15.

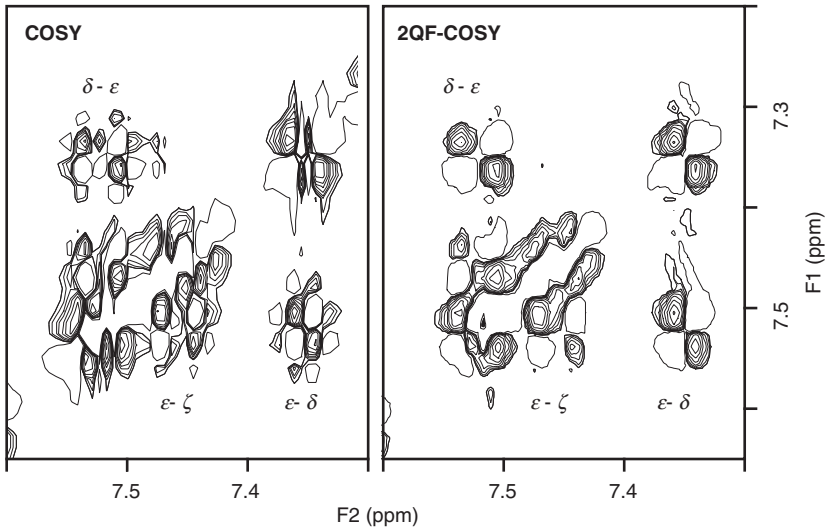

FIGURE 6.25 Comparison of cross-peaks close to the diagonal in COSY and 2QF-COSY. The COSY spectrum was acquired with 16 transients for each of 800 t_1 increments and processed with a sine bell shifted 5° in t_1 and an unshifted sine bell in t_2. The 2QF-COSY was acquired with 32 transients for 800 t_1 increments and processed with a cosine bell in t_1 and a sine bell shifted 60° in t_2. The severe window functions required to reduce the streaks emanating from the diagonal of the COSY spectrum distort the aromatic cross-peaks of Phe45, especially those between $^1H^{\varepsilon}$ and $^1H^{\zeta}$.

Thus, if a probe equipped with three-axis gradients is available, a single gradient-enhanced 2QF-COSY spectrum may substitute for the COSY, pre-TOCSY COSY, and 2QF-COSY spectra.

6.3.2 3QF-COSY

As described in Section 6.3, the 2QF-COSY is just one member of a family of experiments involving filtration through a p-quantum state; experiments with $p > 2$ offer spectral simplification because some resonances cannot participate in a p-quantum coherence (see later, discussion of selection rules). As a practical matter, pQF-COSY experiments with $p > 3$ are applied rarely to proteins.

6.3.2.1 Product Operator Analysis A product operator analysis of the 3QF-COSY experiment initially proceeds as described for the 2QF-COSY, and [6.16] describes the terms present after the second 90°

pulse in the sequence. Only the three-spin term $4I_{1x}I_{2y}I_{3y}$ can contribute to the 3QF-COSY spectrum; all other terms in [6.16] are suppressed by the phase cycle or gradient selection. Just as the product operator $2I_{1x}I_{2y}$ term in the 2QF-COSY experiment was expressed as the combination of DQ and ZQ coherences [6.17], the $4I_{1x}I_{2y}I_{3y}$ operator is expanded as the combination of 3Q coherences and three-spin single-quantum coherences. Using the single-element basis set of Section 2.7.2, and referring to the eigenstates for a three-spin system (Fig. 2.2), a $3Q_x$ coherence is:

$$\begin{aligned} 3Q_x &= \tfrac{1}{2}\left[I_1^+ I_2^+ I_3^+ + I_1^- I_2^- I_3^-\right] \\ &= \tfrac{1}{2}[(I_{1x} + iI_{1y})(I_{2x} + iI_{2y})(I_{3x} + iI_{3y}) \\ &\quad + (I_{1x} - iI_{1y})(I_{2x} - iI_{2y})(I_{3x} - iI_{3y})] \\ &= \tfrac{1}{4}\left[4I_{1x}I_{2x}I_{3x} - 4I_{1y}I_{2y}I_{3x} - 4I_{1x}I_{2y}I_{3y} - 4I_{1y}I_{2x}I_{3y}\right]. \end{aligned} \quad [6.21]$$

Three-spin single-quantum coherences connect eigenstates for which two spins change quantum number by +1 and the third changes by −1, or for which two spins change quantum number by −1 and the third changes by +1; formally, the net coherence order is +1 or −1. For example,

$$\begin{aligned}
1Q_{12\bar{3}} &= \tfrac{1}{2}[I_1^+ I_2^+ I_3^- + I_1^- I_2^- I_3^+] \\
&= \tfrac{1}{2}[(I_{1x} + iI_{1y})(I_{2x} + iI_{2y})(I_{3x} - iI_{3y}) \\
&\quad + (I_{1x} - iI_{1y})(I_{2x} - iI_{2y})(I_{3x} + iI_{3y})] \\
&= \tfrac{1}{4}[4I_{1x}I_{2x}I_{3x} - 4I_{1y}I_{2y}I_{3x} + 4I_{1x}I_{2y}I_{3y} + 4I_{1y}I_{2x}I_{3y}], \qquad [6.22]
\end{aligned}$$

in which the overbar in the subscript on Q indicates the spin changing quantum number in the opposite sense to the other two spins. Taking the appropriate combinations of the three-spin single-quantum terms and the $3Q_x$ term yields the following result:

$$4I_{1x}I_{2y}I_{3y} = -3Q_x + 1Q_{12\bar{3}} + 1Q_{1\bar{2}3} - 1Q_{\bar{1}23}. \qquad [6.23]$$

In the phase-cycled 3QF-COSY experiment, the phase cycle selects only the $3Q_x$ component of [6.23]. Thus, from [6.21], the action of the final 90° pulse acting on the $3Q_x$ term is

$$\begin{aligned}
&-3Q_x \sin(\pi\Omega_1 t_1) \sin(\pi J_{12} t_1) \sin(\pi J_{13} t_1) \\
&\quad \xrightarrow{(\frac{\pi}{2})_x} \tfrac{1}{4}[-4I_{1x}I_{2x}I_{3x} + 4I_{1z}I_{2z}I_{3x} + 4I_{1x}I_{2z}I_{3z} + 4I_{1z}I_{2x}I_{3z}] \\
&\qquad \times \sin(\pi\Omega_1 t_1) \sin(\pi J_{12} t_1) \sin(\pi J_{13} t_1). \qquad [6.24]
\end{aligned}$$

In the gradient-selected 3QF-COSY experiment, the gradient pair selects only the $I_1^+ I_2^+ I_3^+$ component of [6.23]. The resulting product operators after the final 90° pulse are described by [6.24] except that the amplitude is reduced by a factor of two. The first term of [6.24] is unobservable, while the last three correspond to an $I_1 \rightarrow I_3$ cross-peak, an I_1 diagonal peak, and an $I_1 \rightarrow I_2$ cross-peak, respectively. The three observable terms are modulated by the same trigonometric functions; hence, the resonances have the same relative phase in F_1. The combination of three sine terms indicates that all three peaks are antiphase with respect to J_{12} and J_{13}. Likewise in F_2, all three peaks have the same relative phase (x) and are in antiphase with respect to both couplings. The appearance of a double antiphase Lorentzian lineshape is discussed in more detail in Section 6.4.1.1 and Fig. 6.36.

6.3.2.2 Experimental Protocol and Processing The sensitivity of a cross-peak arising from a p-quantum coherence in a pQF-COSY

decreases by a factor of 2^{p-1} (cf. the factors of 1/2 in [6.20] and 1/4 in [6.24]) for a phase-cycled experiment (*27*) and 2^p for a gradient-selected experiment; consequently, more transients must be co-added to obtain a suitable S/N ratio. For this reason, the increased number of steps in the phase cycle to achieve *p*-quantum selection is rarely a problem. Other practical considerations in implementing 3QF-COSY experiments parallel those described above for the 2QF case (Section 6.3.1.2).

The sections of 3QF-COSY spectra shown below were acquired from D_2O solution with 48 transients for each of 512 increments; the spectral width was 3100 Hz and a t_{1max} was 82.6 ms. Phase cycling was used for coherence selection. The spectrum was folded in F_1 as described above. The complete phase cycle used in this experiment is listed in the caption to Fig. 6.20.

Considerations for processing *p*QF-COSY spectra are similar to those for the 2QF-COSY described in Section 6.3.1.3. The cross-peak fine structure is antisymmetric with respect to the chemical shift axes for even *p*, and symmetric for odd *p* (for example, see Fig. 6.27 or 6.30). This simple observation aids in determining appropriate phase corrections for higher order *p*QF-COSY spectra.

6.3.2.3 Information Content The main reason for filtration via higher coherence orders is the spectral simplification achieved. The following selection rules provide the basis for this simplification: (*i*) diagonal peaks will be observed when the active spin has *resolved scalar couplings* to $p-1$ spins; (*ii*) a cross-peak between two spins will be observed when the two active spins have $p-2$ *mutual* resolved coupling partners (*27*). A resolved scalar coupling is a scalar interaction that would give rise to an observable multiplet splitting in the 1D spectrum (assuming no overlap with resonances of other spin systems); thus, degenerate protons can never have a mutual resolved coupling. The cross-peaks expected from these definitions are strictly valid only in the weak coupling limit and are summarized in Fig. 2 of Müller et al. (*27*). Experiments with $p > 3$ have been reported in the literature (*27*, *34*), but the lack of sensitivity and modest gains in spectral simplification preclude their common application to proteins.

Some of the specific advantages of D_2O 3QF-COSY over the 2QF counterpart are (*i*) a removal of $^1H^{\alpha}$ diagonal peaks and $^1H^{\alpha}$–$^1H^{\beta}$ cross-peaks of threonine, alanine, valine, and isoleucine residues, (*ii*) complete removal of all glycine peaks, (*iii*) removal of all diagonal and cross-peaks involving methyl groups except $^1H^{\gamma}$–$^1H^{\delta}$ of isoleucine, and (*iv*) removal of tyrosine aromatic ring resonances (unless the four bond $^1H^{\delta 1}$–$^1H^{\delta 2}$ or

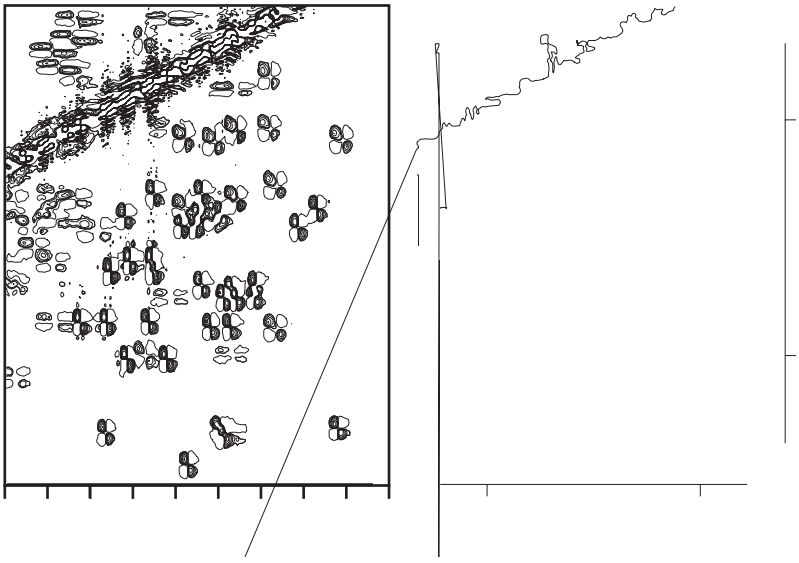

$^1H^{\varepsilon 1}$–$^1H^{\varepsilon 2}$ couplings are resolved) and removal of $^1H^{\alpha}$–$^1H^{\beta}$ cross-peaks of spin systems with degenerate β-methylene protons.

The effect on the methyl fingerprint region is shown in Fig. 6.27. The methyl groups of alanine, threonine, valine, and leucine residues have a single resolved coupling, and formally cannot produce diagonal or cross-peaks in *p*QF-COSY experiments with $p > 2$. This simplification allows ready identification of isoleucine $^1H^{\gamma}$–$^1H^{\delta}$ cross-peaks. Multiexponential relaxation of methyl group coherences results from cross-correlation (Section 5.2.1) and causes violation of the selection rules. Weak *forbidden* cross-peaks and diagonal peaks are sometimes observed from these spin systems in 3QF- and 4QF-COSY experiments (*35*, *36*).

In the $^1H^{\alpha}$–$^1H^{\beta}$ fingerprint region, serine $^1H^{\alpha}$–$^1H^{\beta}$ and proline $^1H^{\gamma}$–$^1H^{\delta}$ cross-peaks are often more readily observed because of the removal of glycine and threonine cross-peaks in this region. In opposition to the general trend in sensitivity for *p*QF-COSY experiments, the double antiphase absorptive fine structure in the 3QF-COSY

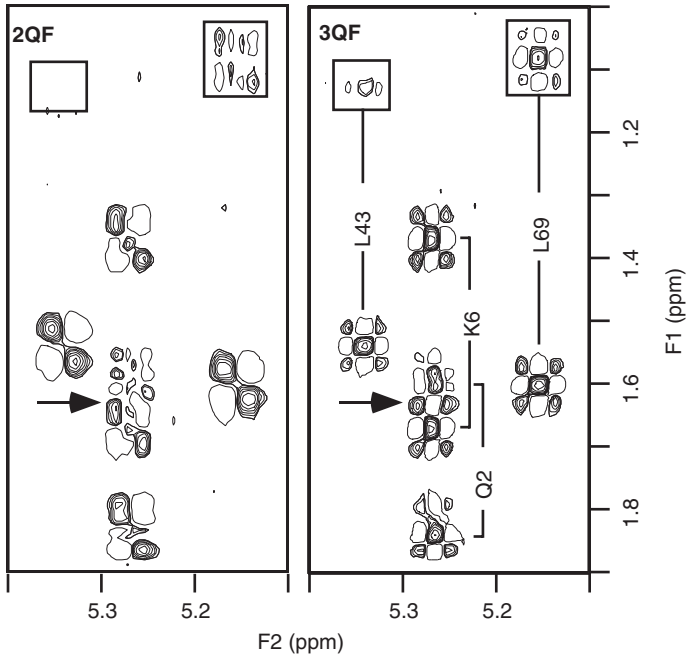

FIGURE 6.28 Comparison of several $^1H^{\alpha}$–$^1H^{\beta}$ cross-peaks in 2QF-COSY and 3QF-COSY spectra. For the upfield $^1H^{\beta}$ of Leu43 and Leu69 (boxed cross-peaks), the active coupling is small and the cancellation of the antiphase components severely attenuates the cross-peaks in the 2QF-COSY. The components of the 3QF-COSY cross-peaks are not separated by the sum of the individual $^3J_{H^{\alpha}H^{\beta}}$, hence the cancellation is not as pronounced. The arrows indicate cancellation (2QF-COSY) and reinforcement (3QF-COSY) of overlapping parts of the downfield Lys6 and the upfield Gln2 $^1H^{\alpha}$–$^1H^{\beta}$ cross-peaks as shown schematically in Fig. 6.30.

leads to less self-cancellation than occurs in the absorptive single antiphase peaks in the 2QF-COSY, and a higher apparent S/N ratio sometimes is observed for particular resonances in 3QF-COSY spectra. (For an example of an ideal absorptive double antiphase Lorentzian line, see Fig. 6.36). An experimental example is illustrated in Fig. 6.28. Although $^1H^{\alpha}$–$^1H^{\beta'}$–$^1H^{\beta''}$ fragments with identical $^1H^{\beta}$ shifts cannot participate in a triple-quantum coherence, even slight deviations from degeneracy can lead to peaks in the 3QF-COSY. In the case of Glu24, other correlation spectra were unable to resolve the slight difference in chemical shift of $^1H^{\beta'}$ and $^1H^{\beta''}$, but a peak was observed in

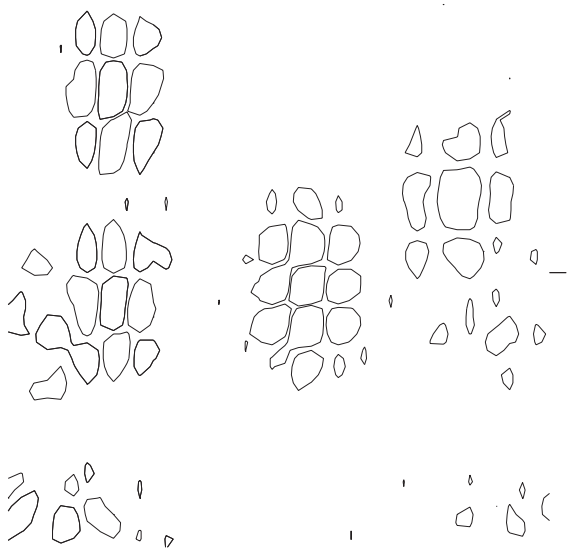

the 3QF-COSY (Fig. 6.29). The fine structure clearly indicates that $^1H^{\beta'}$ and $^1H^{\beta''}$ are separated by approximately 0.02 ppm.

A detailed catalogue of the fine structure observed in cross-peaks in *p*QF-COSY has been presented elsewhere (*27*). In a system of n mutually coupled spins, cross-peaks in a *p*QF-COSY (where $n > p$) will contain contributions from all possible p-quantum states (including combination bands if $n - p = 2, 4, \ldots$). Symmetry properties of the cross-peak multiplets indicate that partially overlapping cross-peaks will be more subject to cancellation in spectra filtered with an even value of p than with an odd value of p (Fig. 6.30) (*37*).

6.3.3 E.COSY

Values of ^3J can provide dihedral angle information that can be used as experimental restraints during protein structure determination480
chemical shifts are slightly diff(ıately 0902

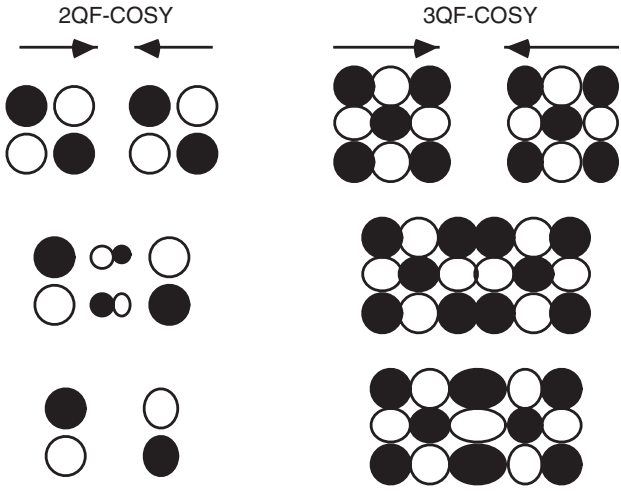

FIGURE 6.30 Schematic view of partially overlapped cross-peaks in 2QF- and 3QF-COSY spectra. Due to the symmetry of the cross-peaks, those in the 2QF-COSY cancel while those in the 3QF-COSY reinforce. A real example of this is observed in Fig. 6.28.

(Section 9.2.1). For spins that possess a single active coupling, the scalar coupling constant can be extracted from the fine structure of a peak in the COSY spectrum (Section 6.2.1.5). If both actively coupled spins have additional passive coupling partners, then the COSY cross-peak fine structure becomes more complicated, and in general the individual multiplet component positions (and hence the scalar coupling constants) are not well resolved for the broad resonance lines observed in protein spectra. A number of methods have been developed that excite only connected transitions (Section 2.6; see Fig. 2.2) — i.e., the passive spins remain unperturbed and the cross-peaks contain only active coupling components. These methods have been given the generic name of *exclusive* COSY or (E.COSY) (*38*). In ^{1}H NMR of proteins, E.COSY spectra provide a useful means to measure $^3J_{H^\alpha H^\beta}$ in side chains containing β-methylene groups; limitations of sensitivity and linewidth have precluded widespread use in measuring other scalar coupling interactions. However, the small linewidths and high concentrations available in peptide studies have allowed the measurement of virtually all ^{1}H–^{1}H couplings in some peptide systems using E.COSY spectra (*39*).

6.3.3.1 Product Operator Analysis The most common approach to obtaining E.COSY data is construction of a linear combination of *p*QF-COSY spectra where the level of filtration includes the orders $p = 0, 1, 2 \ldots, K$ (*38, 40*). The weighting factor given to a particular COSY of multiple-quantum order p in this combination is given by

$$\begin{aligned} W_k &= \tfrac{1}{4}p^2 + W_0 \qquad (p \text{ even}), \\ W_k &= \tfrac{1}{4}(p^2 - 1) + W_1 \qquad (p \text{ odd}), \end{aligned} \qquad [6.25]$$

where the first and second lines of [6.25] are applicable to even and odd k, respectively. Because spectra acquired with $p = 0$ and $p = 1$ contribute only to the diagonal, W_0 and W_1 are customarily set to zero to minimize interference from intense diagonal peaks. Thus, the appropriate weights become $W_2 = 1$, $W_3 = 2$, $W_4 = 4$ etc. For a given cross-peak, *p*QF-COSY is included in the combination if $p - 2$ passive spins are common to the two active spins (*38*). Given the *p*QF-COSY selection rules (Section 6.3.2.3), if a cross-peak appears in the *p*QF-COSY, then the spectrum should be included in the linear combination comprising the E.COSY experiment. For a spin system containing a β-methylene group, a single common passive spin $^1H^{\beta}$ contributes to both $^1H^{\alpha}$–$^1H^{\beta}$ cross-peaks; therefore, the maximum level of multiple-quantum coherence required in the linear combination to remove the passive spin components is 3.

The results of the product operator analyses performed for the 2QF-COSY (Section 6.3.1.1) and 3QF-COSY (Section 6.3.2.1) demonstrate the appearance of cross-peaks in the E.COSY of a three-spin system. From [6.20], the observable term describing the $I_1 \rightarrow I_2$ cross-peak in the 2QF-COSY spectrum of the I_1, I_2, I_3 spin system is proportional to

$$\sigma(2\text{QF})_{12} = -\tfrac{1}{2}\cos(\Omega_1 t_1)\sin(\pi J_{12} t_1)\cos(\pi J_{13} t_1) 2I_{1z}I_{2x}. \qquad [6.26]$$

Similarly from [6.24], the equivalent operator in the 3QF-COSY is

$$\sigma(3\text{QF})_{12} = +\tfrac{1}{4}\sin(\pi\Omega_1 t_1)\sin(\pi J_{12} t_1)\sin(\pi J_{13} t_1) 4I_{1z}I_{2x}I_{3z}. \qquad [6.27]$$

Considering quadrature detection in t_1 and evolution and detection during t_2 gives the following signals for the 2QF-COSY and 3QF-COSY

experiments, respectively:

$$\begin{aligned} s(2\mathrm{QF})_{12} &= -\tfrac{i}{4}\exp(i\Omega_1 t_1)\sin(\pi J_{12} t_1)\cos(\pi J_{13} t_1)\exp(i\Omega_2 t_2) \\ &\quad \times \sin(\pi J_{12} t_2)\cos(\pi J_{23} t_2) \\ &= -\tfrac{i}{16}\exp(i\Omega_1 t_1)\sin(\pi J_{12} t_1)\exp(i\Omega_2 t_2)\sin(\pi J_{12} t_2) \\ &\quad \times \big\{\exp(i\pi J_{13} t_1)\exp(i\pi J_{23} t_2) + \exp(i\pi J_{13} t_1)\exp(-i\pi J_{23} t_2) \\ &\qquad + \exp(-i\pi J_{13} t_1)\exp(i\pi J_{23} t_2) + \exp(-i\pi J_{13} t_1)\exp(-i\pi J_{23} t_2)\big\}, \end{aligned} \quad [6.28]$$

$$\begin{aligned} s(3\mathrm{QF})_{12} &= \tfrac{i}{8}\exp(i\Omega_1 t_1)\sin(\pi J_{12} t_1)\sin(\pi J_{13} t_1)\exp(i\Omega_2 t_2)\sin(\pi J_{12} t_2) \\ &\quad \times \sin(\pi J_{23} t_2) \\ &= -\tfrac{i}{32}\exp(i\Omega_1 t_1)\sin(\pi J_{12} t_1)\exp(i\Omega_2 t_2)\sin(\pi J_{12} t_2) \\ &\quad \times \big\{\exp(i\pi J_{13} t_1)\exp(i\pi J_{23} t_2) - \exp(i\pi J_{13} t_1)\exp(-i\pi J_{23} t_2) \\ &\qquad - \exp(-i\pi J_{13} t_1)\exp(i\pi J_{23} t_2) + \exp(-i\pi J_{13} t_1)\exp(-i\pi J_{23} t_2)\big\}. \end{aligned} \quad [6.29]$$

Combining [6.28] (2QF) and [6.29] (3QF) according to [6.25] yields

$$\begin{aligned} s(2\mathrm{QF})_{12} + 2s(3\mathrm{QF})_{12} &= \tfrac{i}{8}\exp(i\Omega_1 t_1)\ \sin(\pi J_{12} t_1)\ \exp(i\Omega_2 t_2)\ \sin(\pi J_{12} t_2) \\ &\quad \times \big\{\exp(i\pi J_{13} t_1)\ \exp(i\pi J_{23} t_2) + \\ &\qquad \exp(-i\pi J_{13} t_1)\exp(-i\pi J_{23} t_2)\big\}. \end{aligned} \quad [6.30]$$

Thus, two components arising from the passive J_{13} and J_{23} couplings in [6.28] and [6.29] have been removed in [6.30].

The overall effect on the $I_1 \rightarrow I_2$ cross-peak is shown schematically in Fig. 6.31. The E.COSY cross-peak contains a superposition of two two-spin antiphase multiplets, with the displacement being equal to the size of the passive coupling in each dimension. The active coupling can be measured as the antiphase separation (as in Section 6.2.1.5). More importantly, the passive coupling can be measured from the displacements of the two multiplets as a simple peak-to-peak separation, as this distance will not be subject to systematic errors associated with finite

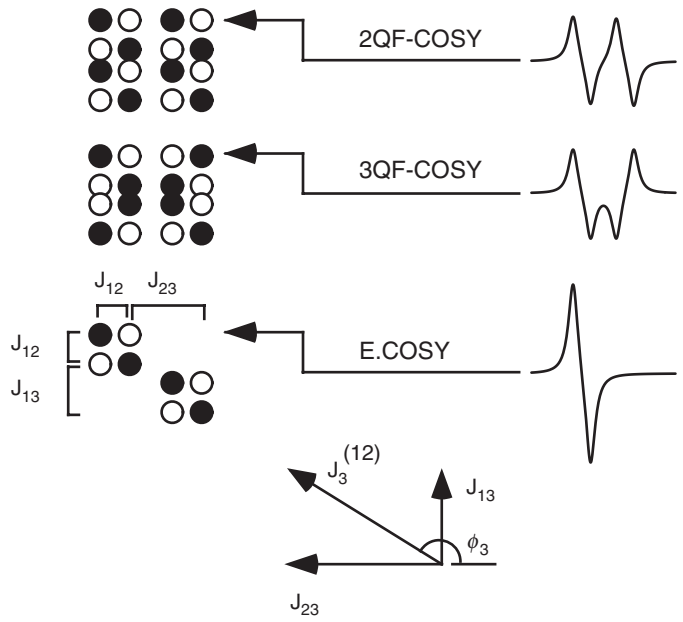

FIGURE 6.31 Schematic view of the I_1–I_2 cross-peak for a three-spin system during 2QF-COSY, 3QF-COSY, and E.COSY experiments. Filled and open circles indicate positive and negative components, respectively. Traces parallel to F_2 through each cross-peak are shown on the right, and were calculated for Lorentzian lines of 4-Hz half-height width, $J_{12} = 6$ Hz, $J_{13} = 10$ Hz, and $J_{23} = -15$ Hz. The vector construction at the bottom is described in the text.

linewidth (Section 6.2.1.5). This feature allows the E.COSY method to determine scalar couplings much smaller than the linewidth, provided the appropriate cross-peaks can be generated.

A displacement vector, $J_3^{(12)}$, connecting peaks of like sign (constructed as shown at the bottom of Fig. 6.31) is associated with a particular passive spin (I_3 in this example). The angle ϕ_3 between the F_2 axis and the displacement vector reflects the sign of the product $J_{13} \times J_{23}$, and can distinguish the relative signs of these two coupling constants (*14*). Provided spectra are processed to have the diagonal running from top right to bottom left, and ϕ_3 is constrained to be between 0° and 180°, positive and negative products of $J_{13} \times J_{23}$ are indicated by $0^\circ < \phi_3 < 90^\circ$ and $90^\circ < \phi_3 < 180^\circ$, respectively.

Although this discussion has been limited to ^{1}H NMR, the E.COSY concept may be extended to include heteronuclear couplings. Small passive couplings (usually ^{1}H–^{1}H) may then be measured in F_2 between two components separated by a large heteronuclear coupling (one bond ^{1}H–X or X–X, where X is ^{15}N or ^{13}C). These applications of the E.COSY principle are discussed in more detail in Section 7.5.

A more thorough analysis extensible to spin systems of greater complexity involves consideration of single-transition basis operators within the energy level diagram of the spin system of interest. Pairs of transitions give rise to each element of fine structure in a cross-peak and are described in the terms discussed in Section 2.6: regressive or progressive, connected or anticonnected. Depending on these qualities, the transition pairs display particular characteristics in the final spectrum, and the appearance of each multiple-quantum filtered (MQF) spectrum, or combination of such spectra, can be deduced (*40*).

6.3.3.2 Experimental Protocol The majority of experimental details for acquisition of 2QF- and 3QF-COSY experiments have been covered in Sections 6.3.1.2 and 6.3.2.2, however, a few aspects are specific to the E.COSY experiment. The weights indicated by [6.25] indicate that the 3QF-COSY data should be scaled by a factor of two compared to the 2QF-COSY if both spectra have been acquired identically (i.e., spectral widths, number of transients, and number of t_1 increments). However, noise introduced by the addition (or subtraction) of the two data sets is minimized if no scaling is performed after acquisition; consequently, the 3QF-COSY spectrum is acquired with twice the number of F_2 transients as for the 2QF-COSY, and the two spectra simply are added. In order to complete the basic phase cycles of both experiments (16 and 24 transients) and acquire twice the number of transients in the 3QF-COSY, 48 and 96 transients must be collected for the 2QF- and 3QF-COSY, respectively. The spectra should be acquired in an interleaved fashion to avoid subtraction artifacts, and combined at the processing stage. In this mode of acquisition, the individual 2QF-COSY and 3QF-COSY experiments also can be analyzed. However, 144 transients must be collected for each t_1 increment in the E.COSY experiment, which requires considerable total acquisition time.

An alternative mode of acquisition uses phase cycling within a single experiment to perform the appropriate data combination between transients (*14*). Many of the steps in the individual phase cycles of the 2QF- and 3QF-COSY experiments are identical, and only need be

TABLE 6.1
Phase Cycles for the E.COSY Experiment[a]

Pulse phase	0°	60°	120°	240°	300°
Receiver phase	0°	180°	0°	0°	180°
Transients	4	3	1	1	3

[a]The relative number of transients acquired for each phase increment in the combined E.COSY experiment. The phase shifts are applied to ϕ_1 and ϕ_2, while keeping the phase of ϕ_3 fixed (0°) in Fig. 6.20.

performed once. Table 6.1 indicates the number of transients that must be collected for each of the six phase increments required for an E.COSY experiment suitable for analysis of three-spin systems. The basic phase cycle contains 12 steps, and can be extended to 48 steps by performing CYCLOPS (Section 4.3.2.3). Although only 48 transients have to be acquired to complete the phase cycle in this method, separate analysis of the 3QF-COSY and 2QF-COSY is not possible.

Finally, the two antiphase multiplets must be resolved in both dimensions to permit accurate measurements of the coupling constants. Normally, the cross-peaks at the F_2 frequency of $^1H^{\alpha}$ are analyzed. These cross-peaks are separated in F_1 by the passive $^1H^{\beta'}$–$^1H^{\beta''}$ coupling, and given the large size of this interaction (15 Hz), sufficient t_1 increments to properly resolve the components are easily acquired. The spectra are acquired from D_2O solution to avoid interference from passive couplings to $^1H^N$, and may be folded in F_1 to improve the digital resolution (Section 6.2.1.2).

The sections of spectra shown in Fig. 6.32 were acquired as separate 2QF- and 3QF-COSY spectra in an interleaved fashion with 48 and 96 transients, respectively. The spectra were folded in F_1, and contained 512 increments of t_1 ($t_{1\max} = 82$ ms). The total acquisition time was 42 hr.

6.3.3.3 Processing Processing parameters for E.COSY data are identical for both methods of acquisition and were generally outlined in Section 6.3.1.3. The $^1H^{\alpha}$–$^1H^{\beta}$ cross-peaks are of primary interest for measuring $^3J_{H^{\alpha}H^{\beta}}$, and are best resolved at the F_2 frequency of $^1H^{\alpha}$. In order to improve the accuracy of the measurement, the spectra should be extensively zero-filled in F_2 (to less than 0.5 Hz per point). The spectrum shown in Fig. 6.32 was processed with moderately

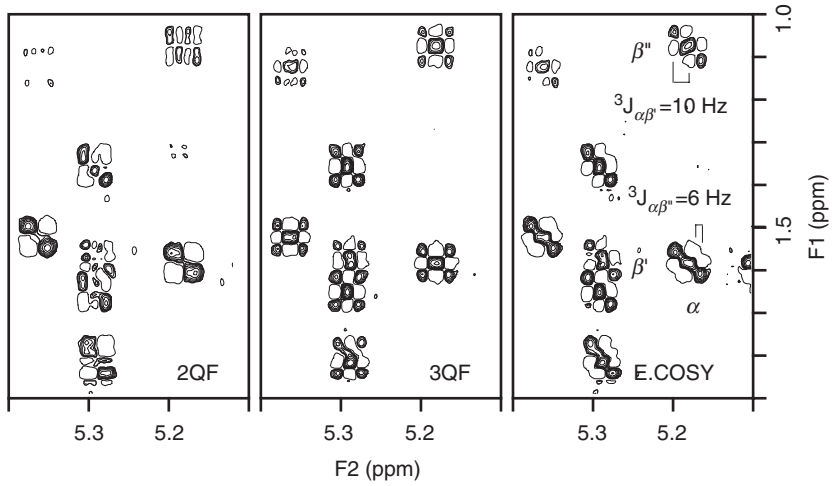

FIGURE 6.32 Section of the E.COSY spectrum of ubiquitin obtained by the co-addition of a 2QF-COSY (48 transients per t_1 increment) and a 3QF-COSY (96 transients per t_1 increment). Measurements of $^3J_{H^\alpha H^\beta}$ from the multiplet patterns are illustrated.

shifted cosine bells and zero-filled from 2048 to 16,384 points to give a final digital resolution of 0.38 Hz/point in F_2. Line-fitting procedures can be used to improve the accuracy of the coupling constant measurement, although coupling constant data are rarely interpreted in such detail that errors of 0.5 Hz are significant (Section 9.2.1).

6.3.3.4 Information Content The principal information provided from the E.COSY is $^3J_{H^\alpha H^\beta}$. The analysis of the product operators has shown that co-addition of 2QF-COSY and 3QF-COSY is sufficient to provide an E.COSY pattern for the cross-peaks of a three-spin system. Longer spin systems have additional scalar coupling interactions with $^1H^\beta$ spins and passive coupling components remain in an E.COSY spectrum constructed from 2QF-COSY and 3QF-COSY; higher orders of *p*QF-COSY must be included to remove these additional passive interactions. However, the passive components are only present in the F_1 ($^1H^\beta$) dimension and $^3J_{H^\alpha H^\beta}$ can still be measured from the displacements in the F_2 ($^1H^\alpha$) dimension.

A section of the E.COSY of ubiquitin is shown in Fig. 6.32. Measurements are most accurate if taken from the displacement by the passive coupling because the artifacts described in Section 6.2.1.5 are

not present. Thus, $^3J_{H^\alpha H^{\beta'}}$ is best measured from the $^1H^\alpha$–$^1H^{\beta''}$ cross-peak and *vice versa*. In order to measure both $^1H^\alpha$–$^1H^\beta$ coupling constants, the $^1H^\alpha$–$^1H^{\beta'}$ and $^1H^\alpha$–$^1H^{\beta''}$ cross-peaks must be resolved, which is not always the case in this crowded region of the spectrum.

6.3.3.5 Experimental Variants Linear combinations of COSY spectra acquired with mixing pulses less than 90° also produce E.COSY-type cross-peak fine structure. In the COSY-β spectrum of an I_1, I_2, I_3 spin system, the following operators give rise to a cross-peak representing coherence transfer $I_1 \rightarrow I_2$ (the t_1 trigonometric factors have been ignored for simplicity):

$$-2I_{1z}I_{2y}\sin^2(\beta) - 4I_{1z}I_{2y}I_{3z}\sin^2(\beta)\cos(\beta). \qquad [6.31]$$

The second term of [6.31] would not be observed in a normal COSY experiment because the term at the end of t_1 from which it originates ($4I_{1y}I_{2z}I_{3z}$) would be converted entirely into unobservable magnetization ($4I_{1z}I_{2y}I_{3y}$) by the 90°_x mixing pulse (for example, see [6.16]). The combination of single and double antiphase lineshapes, represented by the first and second terms in [6.31], respectively, is responsible for generating E.COSY fine structure (Section 6.3.3.1). Thus, combining COSY-β spectra with different rotation angles β suppresses the passive coupling components. Two main disadvantages of this approach are that (1) the cross-peak intensity is low due to the dependence on $\sin^2(\beta)$ and (2) the diagonal is very intense and also contains many dispersive components.

As is evident from [6.31], a single COSY-β experiment does have a degree of E.COSY character. The ratio of connected to unconnected transition intensities is maximal when $\beta \approx 35^\circ$. The undesired passive components are suppressed by more than 10-fold, which is adequate for many applications (*4*). Thus, COSY-35 provides a simple method to obtain $^3J_{H^\alpha H^\beta}$. An example of a COSY-35 spectrum has already been shown in Fig. 6.14 for the H_2O case of glycine $^1H^N$–$^1H^\alpha$ peaks, and Fig. 6.33 compares a section of the $^1H^\alpha$–$^1H^\beta$ region in D_2O with the equivalent region of the E.COSY.

6.4 Multiple-Quantum Spectroscopy

The concept of multiple-quantum (MQ) coherence was introduced in Chapter 2, and multiple-quantum filtration of COSY spectra was

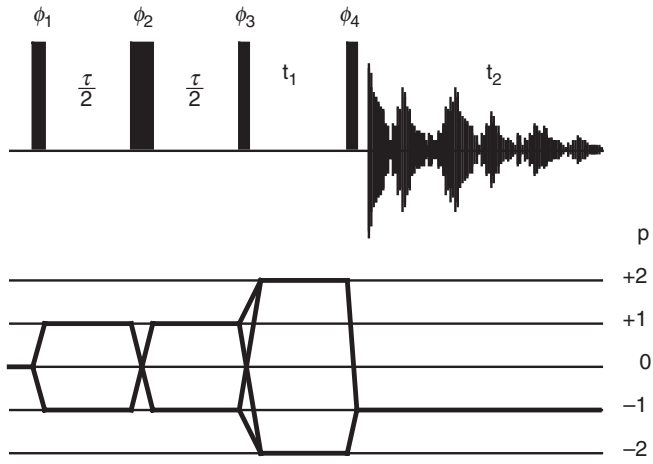

FIGURE 6.34 Pulse sequence for nQ and coherence level diagram for 2Q experiments. The basic 2Q phase cycle is as follows: $\phi_1 = \phi_2 = \phi_3 = x, y, -x, -y$; $\phi_4 = x$; receiver $= 2(x, -x)$. The basic 3Q phase cycle is as follows: $\phi_1 = \phi_2 = 0°$, 60°, 120°, 180°, 240°, 300°; $\phi_3 = 90°$, 150°, 210°, 270°, 330°, 30°; $\phi_4 = 90°$; and receiver $= 3(0°, 180°)$. Axial peak suppression and CYCLOPS phase cycling yields a 32-step phase cycle for 2Q and a 48-step phase cycle for 3Q. Frequency discrimination in F_1 is obtained by shifting the phase of ϕ_1, ϕ_2, ϕ_3, and the receiver according to the TPPI, States, or TPPI–States protocols (Section 4.3.4).

following formula:

$$\begin{array}{lll} \phi_1 \quad \text{and} \quad \phi_2\text{:} & & n\pi/p \\ \phi_3\text{:} & & \phi_1 + \psi \\ \phi_4\text{:} & & \psi \\ \text{receiver:} & & -n\pi + 2\psi \end{array} \qquad [6.32]$$

where ψ is 0 for even p and $\pi/2$ for odd p. In these expressions, n takes integer values from 0 to $2p - 1$, thus the basic phase cycle consists of $2p$ steps. This can be expanded by performing CYCLOPS to yield a total of $8p$ steps (note the close similarity between this experiment and the pQF-COSY experiments (Section 6.3).

6.4.1 2Q SPECTROSCOPY

Although pQ experiments can be adjusted to observe a range of multiple-quantum states, 2Q and 3Q experiments usually are adequate

for studies of proteins. The 2Q experiment, discussed in the present section, is the most commonly performed, and the theoretical analysis of the 2Q experiment presented here illustrates the main differences and advantages compared to COSY and MQF-COSY techniques. The 3Q experiment is described in Section 6.4.2.

6.4.1.1 Product Operator Analysis Initially, evolution of a two-spin system during the 2Q pulse sequence is treated. In this example, the simplest results are obtained if the fates of both I_1 and I_2 initial z-magnetization are calculated. At the end of the 90°_x–$\tau/2$–180°_x–$\tau/2$–90°_x sequence, the following operators are present at the start of the t_1 period:

$$I_{1z} + I_{2z} \xrightarrow{\left(\frac{\pi}{2}\right)_x - \frac{\tau}{2} - \pi_x - \frac{\tau}{2} - \left(\frac{\pi}{2}\right)_x} [I_{1z} + I_{2z}] \cos(\pi J_{12}\tau) + \left[2I_{1x}I_{2y} + 2I_{1y}I_{2x}\right] \sin(\pi J_{12}\tau). \quad [6.33]$$

If the delay $\tau = 1/(2J_{12})$, the longitudinal terms, $I_{1z} + I_{2z}$, will vanish, leaving only the pure DQ_y coherence, $2I_{1x}I_{2y} + 2I_{1y}I_{2x}$. However, in a real sample, a range of values of J_{12} will be encountered, and not all magnetization can be converted into two-quantum coherence; however, the phase cycling suppresses the residual longitudinal magnetization and retains only the two-quantum coherence. In the rest of this analysis the longitudinal components will be ignored. During t_1, the two-quantum coherence evolves at the sum of the I_1 and I_2 chemical shifts, $\Omega_{12} = \Omega_1 + \Omega_2$, but does not evolve under the influence of J_{12} (Section 2.7). The final 90°_x pulse creates the product operators that evolve during t_2:

$$\begin{aligned}\left[2I_{1x}I_{2y} + 2I_{1y}I_{2x}\right] \sin(\pi J_{12}\tau) &\xrightarrow{t_1} \left[2I_{1x}I_{2y} + 2I_{1y}I_{2x}\right] \cos(\Omega_{12}t_1) \sin(\pi J_{12}\tau) \\ &\quad - \left[2I_{1x}I_{2x} + 2I_{1y}I_{2y}\right] \sin(\Omega_{12}t_1) \sin(\pi J_{12}\tau), \\ &\xrightarrow{\left(\frac{\pi}{2}\right)_x} [2I_{1x}I_{2z} + 2I_{1z}I_{2x}] \cos(\Omega_{12}t_1) \sin(\pi J_{12}\tau) \\ &\quad - [2I_{1x}I_{2x} + 2I_{1z}I_{2z}] \sin(\Omega_{12}t_1) \sin(\pi J_{12}\tau). \end{aligned} \quad [6.34]$$

The final line of [6.34] contains a combination of longitudinal two-spin order magnetization and a mixture of zero- and two-quantum

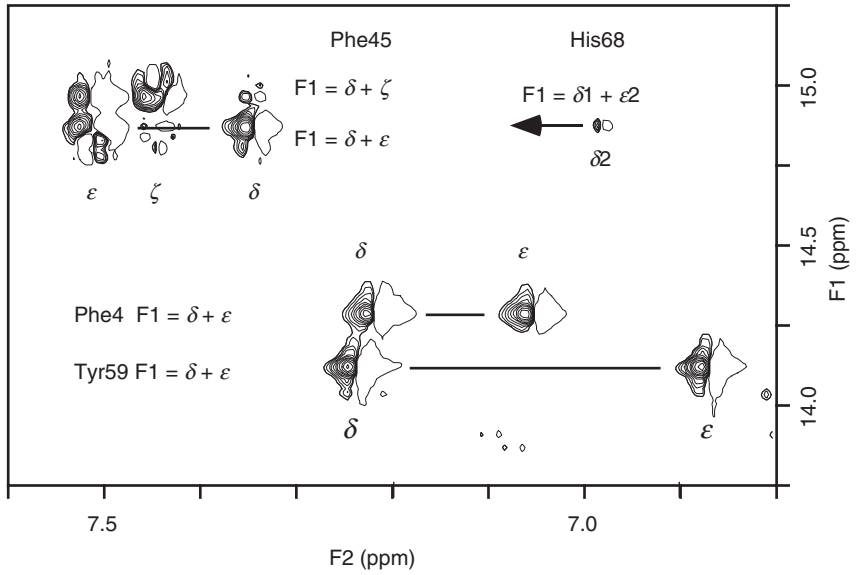

FIGURE 6.35 Example of the appearance of 2Q cross-peaks arising from two-spin systems. The peaks arising from aromatic ring protons of Tyr59 are present at the bottom of the figure, and represent a two-spin system, because $^4J_{H^{\delta 1}H^{\delta 2}}$ and $^4J_{H^{\varepsilon 1}H^{\varepsilon 2}}$ are not resolved. Although not formally two-spin systems, the cross-peaks from the aromatic ring protons of Phe4, and Phe45 are also labeled. The small $^4J_{H^{\delta 2}H^{\varepsilon 1}}$ of His68 also gives rise to a weak cross-peak. The spectrum was acquired from D_2O solution with an excitation delay, $\tau = 22$ ms.

coherence; neither of these operators leads to observable magnetization during t_2 and can be ignored. By analogy with the previous results obtained for the COSY experiment, the $2I_{1x}I_{2z}$ and $2I_{1z}I_{2x}$ terms in the penultimate line represent antiphase magnetization with peaks centered at $\Omega_1 \pm \pi J_{12}$ and $\Omega_2 \pm \pi J_{12}$ in F_2 (again with Ω in units of angular frequency). Both of the product operators are modulated by $\cos[(\Omega_1 + \Omega_2)t_1]$ and give rise to resonances at $\Omega_1 + \Omega_2$ in F_1. The lineshapes have no fine structure in this dimension. The appearance of a two-spin system in the 2Q spectrum is exemplified by the peaks from Tyr59 of ubiquitin Fig. 6.35.

More interesting results are obtained if an equivalent analysis is performed on a system containing the three spins I_1, I_2, and I_3 with coupling constants of J_{12}, J_{13}, and J_{23}. During the initial spin echo period, evolution of all three couplings will take place but chemical shifts

will be refocused. Concentrating on the I_1 magnetization only,

$$\begin{aligned} I_{1z} \xrightarrow{\left(\frac{\pi}{2}\right)_x - \frac{\tau}{2} - \pi_x - \frac{\tau}{2} - \left(\frac{\pi}{2}\right)_x} & I_{1z} \cos(\pi J_{12}\tau) \cos(\pi J_{13}\tau) \\ & + 2I_{1x}I_{2y} \sin(\pi J_{12}\tau) \cos(\pi J_{13}\tau) \\ & + 2I_{1x}I_{3y} \cos(\pi J_{12}\tau) \sin(\pi J_{13}\tau) \\ & - 4I_{1z}I_{2y}I_{3y} \sin(\pi J_{12}\tau) \sin(\pi J_{13}\tau). \end{aligned} \quad [6.35]$$

The resulting longitudinal operator is suppressed by the phase cycle. The remaining three terms are mixtures of double- and zero-quantum coherence (Section 2.7.5) described by [6.17]–[6.19]. Once again, the phase cycling retains only the two-quantum operators. Allowing for evolution as described in Section 2.7.5, the following terms are present at the end of t_1:

$$\begin{aligned} & \mathrm{DQ}_y^{12} \sin(\pi J_{12}\tau) \cos(\pi J_{13}\tau) + \mathrm{DQ}_y^{13} \cos(\pi J_{12}\tau) \sin(\pi J_{13}\tau) \\ & \quad + 2I_{1z}\mathrm{DQ}_x^{23} \sin(\pi J_{12}\tau) \sin(\pi J_{13}\tau) \\ & \quad \xrightarrow{t_1} \left[\mathrm{DQ}_y^{12} \cos(\pi K_{12}t_1) - 2\mathrm{DQ}_x^{12}I_{3z} \sin(\pi K_{12}t_1)\right] \\ & \qquad \times \cos(\Omega_{12}t_1) \sin(\pi J_{12}\tau) \cos(\pi J_{13}\tau) \\ & \qquad - \left[\mathrm{DQ}_x^{12} \cos(\pi K_{12}t_1) + 2\mathrm{DQ}_y^{12}I_{3z} \sin(\pi K_{12}t_1)\right] \\ & \qquad \times \sin(\Omega_{12}t_1) \sin(\pi J_{12}\tau) \cos(\pi J_{13}\tau) \\ & \qquad + \left[\mathrm{DQ}_y^{13} \cos(\pi K_{13}t_1) - 2\mathrm{DQ}_x^{13}I_{2z} \sin(\pi K_{13}t_1)\right] \\ & \qquad \times \cos(\Omega_{13}t_1) \cos(\pi J_{12}\tau) \sin(\pi J_{13}\tau) \\ & \qquad - \left[\mathrm{DQ}_x^{13} \cos(\pi K_{13}t_1) + 2\mathrm{DQ}_y^{13}I_{2z} \sin(\pi K_{13}t_1)\right] \\ & \qquad \times \sin(\Omega_{13}t_1) \cos(\pi J_{12}\tau) \sin(\pi J_{13}\tau) \\ & \qquad + \left[2I_{1z}\mathrm{DQ}_x^{23} \cos(\pi K_{23}t_1) - \mathrm{DQ}_y^{23} \sin(\pi K_{23}t_1)\right] \\ & \qquad \times \cos(\Omega_{23}t_1) \sin(\pi J_{12}\tau) \sin(\pi J_{13}\tau) \\ & \qquad + \left[2I_{1z}\mathrm{DQ}_y^{23} \cos(\pi K_{23}t_1) + \mathrm{DQ}_x^{23} \sin(\pi K_{23}t_1)\right] \\ & \qquad \times \sin(\Omega_{23}t_1) \sin(\pi J_{12}\tau) \sin(\pi J_{13}\tau). \end{aligned} \quad [6.36]$$

In this expression, $K_{ij} = J_{ik} + J_{jk}$ is the double-quantum splitting and is equal to the sum of the coupling constants between the active spins (I_i and I_j) and the mutual passive spin (I_k).

Expansion of the right-hand side of [6.36] into single Cartesian operators indicates that, following the final 90°_x pulse, none of the resulting terms 2, 4, or 6 leads to observable magnetization, and the terms 1, 3, and 5 yield

$$\begin{aligned}
&\tfrac{1}{2}[2I_{1x}I_{2z} + 2I_{1z}I_{2x}] \cos(\Omega_{12}t_1) \cos(\pi K_{12}t_1) \sin(\pi J_{12}\tau) \cos(\pi J_{13}\tau) \\
&+ \tfrac{1}{2}\big[4I_{1x}I_{2x}I_{3y} - 4I_{1z}I_{2z}I_{3y}\big] \cos(\Omega_{12}t_1) \sin(\pi K_{12}t_1) \sin(\pi J_{12}\tau) \cos(\pi J_{13}\tau) \\
&+ \tfrac{1}{2}[2I_{1x}I_{3z} + 2I_{1z}I_{3x}] \cos(\Omega_{13}t_1) \cos(\pi K_{13}t_1) \cos(\pi J_{12}\tau) \sin(\pi J_{13}\tau) \\
&+ \tfrac{1}{2}\big[4I_{1x}I_{2y}I_{3x} - 4I_{1z}I_{2y}I_{3z}\big] \cos(\Omega_{13}t_1) \sin(\pi K_{13}t_1) \cos(\pi J_{12}\tau) \sin(\pi J_{13}\tau) \\
&+ \tfrac{1}{2}\big[-4I_{1y}I_{2x}I_{3x} + 4I_{1y}I_{2z}I_{3z}\big] \cos(\Omega_{23}t_1) \cos(\pi K_{23}t_1) \sin(\pi J_{12}\tau) \sin(\pi J_{13}\tau) \\
&+ \tfrac{1}{2}[2I_{2x}I_{3z} + 2I_{2z}I_{3x}] \cos(\Omega_{23}t_1) \sin(\pi K_{23}t_1) \sin(\pi J_{12}\tau) \sin(\pi J_{13}\tau).
\end{aligned} \qquad [6.37]$$

The terms proportional to $2I_{1x}I_{2z} + 2I_{1z}I_{2x}$ on line 1 of [6.37] are observable during t_2 and generate cross-peaks at frequencies Ω_1 and Ω_2 in F_2 with an antiphase splitting of J_{12}. Both of these peaks have an F_1 shift of $\Omega_1 + \Omega_2$ and are referred to as *direct peaks*. Because

$$\cos(\Omega_{12}t_1) \cos(\pi K_{12}t_1) = \tfrac{1}{2}[\cos(\Omega_{12}t_1 - \pi K_{12}t_1) + \cos(\Omega_{12}t_1 + \pi K_{12}t_1)], \qquad [6.38]$$

the direct peaks have in-phase lineshapes in F_1. The direct peaks are phased to absorption in both dimensions, and the phases of other peaks in the spectrum are described relative to these direct peaks. Direct peaks between spins I_1 and I_3 are represented by line 3 and the direct peaks between spins I_2 and I_3 are on line 6 of [6.37]. In all cases, the F_2 lineshapes are absorptive and antiphase with respect to the active coupling. The F_1 lineshape of the I_1–I_3 peaks is equivalent to that described above for the I_1–I_2 peaks, while the I_2–I_3 peaks are dispersive antiphase in this dimension.

The $2I_{1x}I_{2x}I_{3y}$ operator term on line 2 of [6.37] is a three-spin coherence that is not observable. The $2I_{1z}I_{2z}I_{3y}$ term describes an I_3 coherence that is antiphase with respect to I_1 and I_2 in F_2. Because both J_{12} and J_{13} are resolved, this is an observable term and will have a double antiphase dispersive lineshape in F_2; this lineshape and several others observed in 2Q spectra are displayed in Fig. 6.36. The cross-peak has an F_2 chemical shift of Ω_3 and is modulated at a frequency $\Omega_1 + \Omega_2$ during F_1. This resonance is described as a *remote peak*. Because of the $\cos(\Omega_{12}t_1) \sin(\pi K_{12}t_1)$ modulation, this peak has a dispersive antiphase lineshape in F_1 (Fig. 6.36). The first terms on lines 4 and 5 of [6.37] are not observable, while the second terms describe

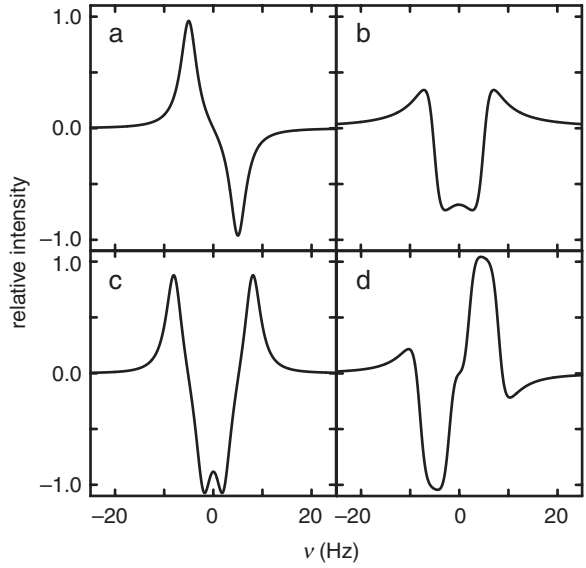

FIGURE 6.36 Lineshapes of single (a, b) and double (c, d) antiphase Lorentzian lines phased to absorption (a, c) and dispersion (b, d). These lineshapes are commonly found in cross-peaks in 2Q spectra. In all panels, the linewidths of the individual Lorentzian lines are 4.0 Hz and a single line has an intensity of 1. The scalar coupling constants correspond to a 10-Hz coupling (top) or a 10- and a 6-Hz coupling (bottom). Note that in real spectra (poor digital resolution, linewidths comparable to the splittings, and the presence of passive couplings), distinguishing between absorptive antiphase and dispersive double antiphase lineshapes or between dispersive antiphase and absorptive double antiphase lineshapes can be difficult.

the character of the I_1–I_3 and I_2–I_3 remote peaks, respectively. The F_2 lineshape of both peaks is double antiphase dispersive, while in F_1 the former is dispersive antiphase and the latter is absorptive in-phase. The positions of all of the peaks described by [6.37] are depicted schematically in Fig. 6.37 and the lineshapes of these peaks are summarized in Table 6.2.

As a result of this analysis, several interesting points emerge for a spin system in which all three coupling constants are resolved: (*i*) the initial I_1 magnetization contributes to all nine cross-peaks in the spectrum, (*ii*) peaks at a given F_1 and F_2 frequency can arise by three different pathways starting initially from I_1, I_2 or I_3 magnetization, (*iii*) the three pathways contributing to a given peak all have the same

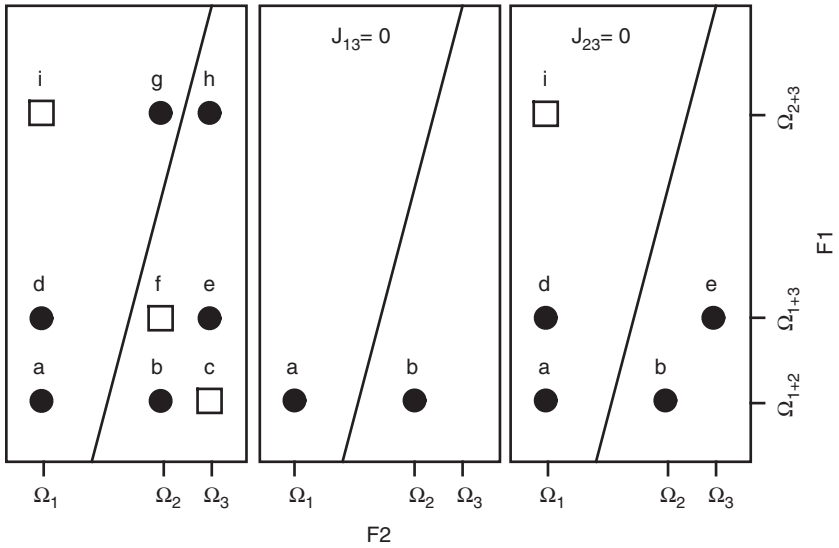

FIGURE 6.37 Contributions of initial I_1 magnetization to the peaks observed in the 2Q spectrum of a three-spin system. The filled circles and open squares represent direct and remote peaks, respectively, while the lines indicate the pseudo-diagonal ($F_1 = 2F_2$). The left panel assumes that J_{12}, J_{13}, and J_{23} are resolved. If J_{13} (center) or J_{23} (right) is not resolved, then I_1 contributes to fewer peaks. The F_1 and F_2 lineshapes of the cross-peaks, labeled a–i, are described in Table 6.2.

F_2 lineshape (absorptive antiphase or dispersive double antiphase for direct or remote peaks, respectively), and (*iv*) one of the pathways leading to a direct peak has dispersive antiphase character in F_1, whereas two of the pathways have this lineshape for the remote peaks. Consequently, all peaks will have dispersive tails in the F_1 dimension.

Generally, 2Q spectra are run with short mixing times [$\tau < (2J_{jk})^{-1}$] to avoid unnecessary loss of magnetization via relaxation, and $\sin(\pi J_{jk}\tau)$ and $\cos(\pi J_{jk}\tau)$ will both be positive. Due to the similarity of a negative dispersive antiphase peak and a positive absorptive in-phase peak (Fig. 6.36), the three contributions to a remote connectivity will add constructively in such experiments. Furthermore, the remote and direct peaks can be differentiated on the basis of the F_2 lineshape: if the spectrum is phased so that the positive lobe of the absorptive antiphase direct peak is downfield of the peak center, then the major positive lobe

TABLE 6.2
Lineshapes in a 2Q Spectrum[a]

		Chemical shift		Lineshape			
Peak	Type	F_1	F_2	F_1		F_2	
a	Direct	$\Omega_1+\Omega_2$	Ω_1	abs	in	abs	anti
b	Direct	$\Omega_1+\Omega_2$	Ω_2	abs	in	abs	anti
c	Remote	$\Omega_1+\Omega_2$	Ω_3	disp	anti	disp	anti × 2
d	Direct	$\Omega_1+\Omega_3$	Ω_1	abs	in	abs	anti
e	Direct	$\Omega_1+\Omega_3$	Ω_3	abs	in	abs	anti
f	Remote	$\Omega_1+\Omega_3$	Ω_2	disp	anti	disp	anti × 2
g	Direct	$\Omega_2+\Omega_3$	Ω_2	disp	anti	abs	anti
h	Direct	$\Omega_2+\Omega_3$	Ω_3	disp	anti	abs	anti
i	Remote	$\Omega_2+\Omega_3$	Ω_1	abs	in	disp	anti × 2

[a]Shown are the lineshapes of the cross-peaks in a 2Q spectrum of a three-spin system that result from initial I_1 magnetization. The peak labels (a–i) refer to the schematic spectrum shown in Fig. 6.37. In the table, Ω_1, Ω_2, and Ω_3 are the resonance frequencies of spins I_1, I_2, and I_3, respectively; "abs" and "disp" indicate absorption and dispersion lineshapes, respectively; "in," "anti," and "anti × 2" refer to in-phase, antiphase, and doubly antiphase multiplet structures, respectively.

of the dispersive double antiphase remote peak will be upfield of the peak center. Due to changes in sign of the trigonometric terms for long τ, these generalizations are not always valid, although the relative signs of the peaks do change in a predictable manner if the coupling constants are known [e.g., see Dalvit et al. (*42*)].

Finally, a linear three-spin system is examined by considering the effect of setting one of the couplings to zero; I_1 may be considered a terminal spin in a linear system if $J_{13}=0$. In this case, $\sin(\pi J_{13}\tau)=0$ and terms such as $4I_{1z}I_{2z}I_{3y}$ are no longer observable because the antiphase state between I_1 and I_3 can never evolve into observable magnetization during t_2. Thus, of the nine terms (peaks a–i) described in Table 6.2, only lines 1 and 2 (peaks a and b) correspond to observable peaks; i.e., initial I_1 magnetization can only contribute to the direct peaks between I_1 and I_2. Alternatively, I_1 may be considered the middle spin of a linear system if $J_{23}=0$. In this case, initial I_1 magnetization contributes to the I_1–I_2 direct peaks (peaks a and b), the I_1–I_3 direct peaks (peaks d and e), and the I_2–I_3 remote peak (peak i). Consideration of these results indicates that a remote peak is only observed when both of the spins contributing to the double-quantum frequency have resolved couplings to the third passive spin

whose frequency is measured in F_2. Results such as these form the basis of the selection rules that are discussed in more detail in Section 6.4.2.3.

6.4.1.2 Experimental Protocol As already described, the spin echo sequence in Fig. 6.34 serves to generate antiphase magnetization. Thus, the choice of delay, τ, will depend upon the magnitudes of the active scalar coupling constants. For 2Q spectra acquired for proteins in H_2O and D_2O solution, $\tau = 30$ ms compromises between coherent evolution and incoherent relaxation. In order to emphasize particular correlations, spectra with τ as low as 20 ms and as large as 80 ms have been reported in the literature (*23*, *42*).

The 180° pulse in the middle of the delay τ can be a source of several types of artifact in the final spectrum, many of which can be alleviated by the use of a composite 180° pulse of the form $90^\circ_{\phi 1} 180^\circ_{\phi 1 + \pi/2} 90^\circ_{\phi 1}$ (Section 3.4.2) (*43*) or by insertion of a pair of gradient pulses flanking the 180° pulse (Section 3.6). In addition, spectra of high quality can usually be obtained without presaturation of the solvent resonance during the 2Q excitation period. This often leads to the observation of more intense correlations involving protons resonating close to the solvent signal (see later).

As discussed in Section 4.3.4.1, quadrature detection in the t_1 dimension of two-dimensional NMR spectra is achieved by shifting the phase of pulses prior to t_1 according to the TPPI, States, or TPPI–States protocols in order to shift the phase of the indirectly detected coherences by 90°. Multiple-quantum coherences are p-fold more sensitive to rf phase shifts than are single-quantum coherences. Thus, in a pQ experiment, the phases ϕ_1, ϕ_2, and ϕ_3 must be incremented by $\pi/(2|p|)$ — that is, by $\pi/4$ for a 2Q experiment.

The choice of spectral width in F_1 of the 2Q experiment is not straightforward because resonance peaks appear at sums of the chemical shifts of coupled resonances, and some prior knowledge of the system is helpful. For work in H_2O solution, the spectrum must extend downfield of the largest sum of two coupled spins; most usually, this will result from the most downfield $^1H^N$ or $^1H^\alpha$ resonance, or from aromatic ring protons. This limit can be calculated if COSY or other correlation spectra have already been acquired, or else estimated from the sum of the most downfield $^1H^N$ and $^1H^\alpha$ resonances observed in a 1D spectrum. The upfield spectral limit can be calculated from the cross-peaks observed in the upfield region of the COSY (usually involving methyl resonances) or else estimated as twice the frequency of the most upfield resonance in the 1D spectrum.

The carrier usually is positioned on resonance with the water signal. The resulting large spectral width suggests that many t_1 points will have to be acquired to achieve the required resolution of resonances in the F_1 dimension. Alternatively, because the focus of ^{1}H NMR spectroscopy in H_2O is primarily the $^1H^N$–$^1H^\alpha$ correlations, the F_1 spectral width can be reduced and the carrier position shifted to span the spectral region expected for the $^1H^N$–$^1H^\alpha$ correlations only. In similar fashion, the digital resolution for 2Q spectra acquired from D_2O solution can be increased by setting the carrier position and spectral width to span resonances arising from the aliphatic resonances only.

The lineshapes of all peaks in the F_1 dimension of the 2Q spectrum are either absorptive in-phase or dispersive antiphase (Table 6.2 and Fig. 6.36); consequently, large values of t_{1max} are not required. Given the preceding discussion of product operators, the acquisition parameters chosen for F_2 are similar to those used for COSY spectra.

The 2Q spectra obtained from H_2O solution discussed in the next section were collected with 32 transients for each of 800 t_1 increments and a mixing period, τ, of 22 or 32 ms. The F_1 spectral width was 5600 Hz and $t_{1max} = 71.4$ ms; this was sufficient to span all of the $^1H^N$–$^1H^\alpha$ correlations, but resulted in folding some of the upfield aliphatic side chain correlations. An equivalent spectrum was recorded in D_2O solution with 600 t_1 increments, $\tau = 30$ ms, an F_1 spectral width of 5000 Hz ($t_{1max} = 60$ ms), and with the transmitter in the center of the aliphatic region; aromatic resonances were folded.

6.4.1.3 Processing As for COSY spectra, unshifted sine-bell window functions are applied in F_2 of 2Q spectra acquired in H_2O solution to attenuate the residual solvent resonance; in D_2O solution, the window function can be phase shifted to increase sensitivity. Applying the sine bell over more points will decrease the S/N ratio but increase the resolution. The 2Q spectrum does not contain dispersive in-phase peaks in F_1; therefore, window functions need not be as strongly resolution enhancing as for COSY. A simple cosine bell to prevent truncation artifacts is usually sufficient. The center of the 2Q spectrum in F_1 is referenced to be double the carrier frequency. Phase parameters are derived in a fashion similar to derivation of those of the COSY experiment.

6.4.1.4 Information Content Like COSY spectra, 2Q spectra contain information about scalar coupling networks; however, 2Q spectra have unique features that circumvent some of the inherent

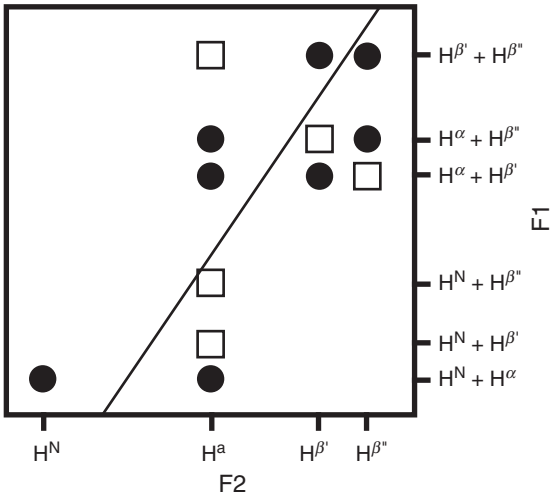

FIGURE 6.38 Schematic representation of the peaks expected in the 2Q spectrum of a $^1H^N$–$^1H^{\alpha}$–$^1H^{\beta 2}$ spin system ($^4J_{H^N H^{\beta}}$ is assumed to be zero). The filled circles and open squares represent direct and remote peaks, respectively, while the line indicates the pseudo-diagonal ($F_1 = 2F_2$).

problems of COSY experiments and provide additional information through both direct and remote correlations. Direct peaks occur at the sum of two chemical shifts of two coupled spins in F_1 and at the chemical shift of each spin in F_2. From the product operator analysis (Section 6.4.1.1), remote peaks also occur in systems of three or more coupled spins. Remote peaks occur at the sum of the frequencies of two actively coupled spins in F_1, and at the frequency of the third passively coupled spin in F_2. The peaks expected in the 2Q spectrum of an $^1H^N - {}^1H^{\alpha} - {}^1H_2^{\beta}$ spin system are presented schematically in Fig. 6.38. The presence of these peaks are formally described by selection rules (*41*) that are discussed more fully in Section 6.4.2.3.

The problems of COSY spectra that can be partially alleviated in the 2Q spectroscopy fall into three categories: diagonal peaks, self-cancellation, and attenuation by solvent presaturation. The dispersive tails of diagonal peaks in COSY spectra can curtail observation of correlations between resonances with similar chemical shifts. The 2Q spectrum does not contain diagonal peaks and observation of cross-peaks is facilitated. In this respect, 2Q spectra are comparable to 2QF-COSY spectra, provided that the latter have been acquired with

sufficient t_1 points to allow resolution of the diagonal and cross-peaks at the same F_2 shift. Self-cancellation of COSY cross-peaks has been described in detail in Section 6.2.1.5. The attenuation that this causes is most severe in F_1, where the linewidth is determined by $t_{1\max}$. In 2Q spectroscopy, the peaks have absorptive in-phase and dispersive antiphase character in F_1, and are not subject to cancellation. Thus, for interactions with small scalar coupling constants or for proteins with large linewidths, 2Q spectra can display correlations that are unobserved in COSY spectra. Finally, presaturation of the solvent peak in the COSY experiment also attenuates correlations involving protons (usually $^1H^{\alpha}$) that resonate close to, or coincident with, the solvent resonance. In a 2Q experiment, even if presaturation is employed prior to the initial 90° pulse (Fig. 6.34), antiphase magnetization between $^1H^N$ and $^1H^{\alpha}$ still develops, from the initial $^1H^N$ magnetization, provided that the solvent resonance is not irradiated during the delay τ (*44*). Thus, 2Q coherence can still be generated for these resonances. In the COSY spectrum of ubiquitin, three $^1H^N$–$^1H^{\alpha}$ cross-peaks were absent because of $^1H^{\alpha}$ presaturation (Fig. 6.9). The equivalent region of the 2Q spectrum clearly reveals these correlations (Fig. 6.39).

Perhaps the biggest advantage of 2Q over COSY experiments is the presence of remote peaks. Usually, remote peaks occur in addition to direct peaks, and for short values of τ are easily recognized by the 180° phase difference in F_2 relative to the direct peaks (see product operator analysis in Section 6.4.1.1). Because the remote F_1 frequency only gives information about the sum of two of the chemical shifts, at least one direct peak must also be observed at the same F_2 shift to determine all three chemical shifts of the spin system. However, the remote peaks are observed even if two of the coupled spins have degenerate chemical shifts. This feature makes 2Q spectroscopy one of the few reliable methods to identify cases of chemical shift degeneracy.

In addition to the important direct peaks with $^1H^{\alpha}$ (Fig. 6.39), amide protons are involved in two sets of remote connectivities involving glycine residues and all residues containing an $^1H^{\beta}$ proton (*45*). Glycine residues are unique in that their amide protons are directly coupled to two α-protons. The coupling within this group gives rise to three peaks at $F_2 = {}^1H^N$: the two direct peaks at $F_1 = {}^1H^N + {}^1H^{\alpha'}$ and $^1H^N + {}^1H^{\alpha''}$ and also a remote peak at $F_1 = {}^1H^{\alpha'} + {}^1H^{\alpha''}$. In COSY spectra, one of the two cross-peaks expected for the glycine $^1H^N$–$^1H^{\alpha}$ residue is often missing, due to either a small active coupling (leading to self-cancellation), an overlap with other $^1H^N$–$^1H^{\alpha}$ correlations, or a degeneracy of the $^1H^{\alpha}$ and $^1H^{\alpha''}$ shifts, hence the observation of the remote peak in the 2Q spectrum

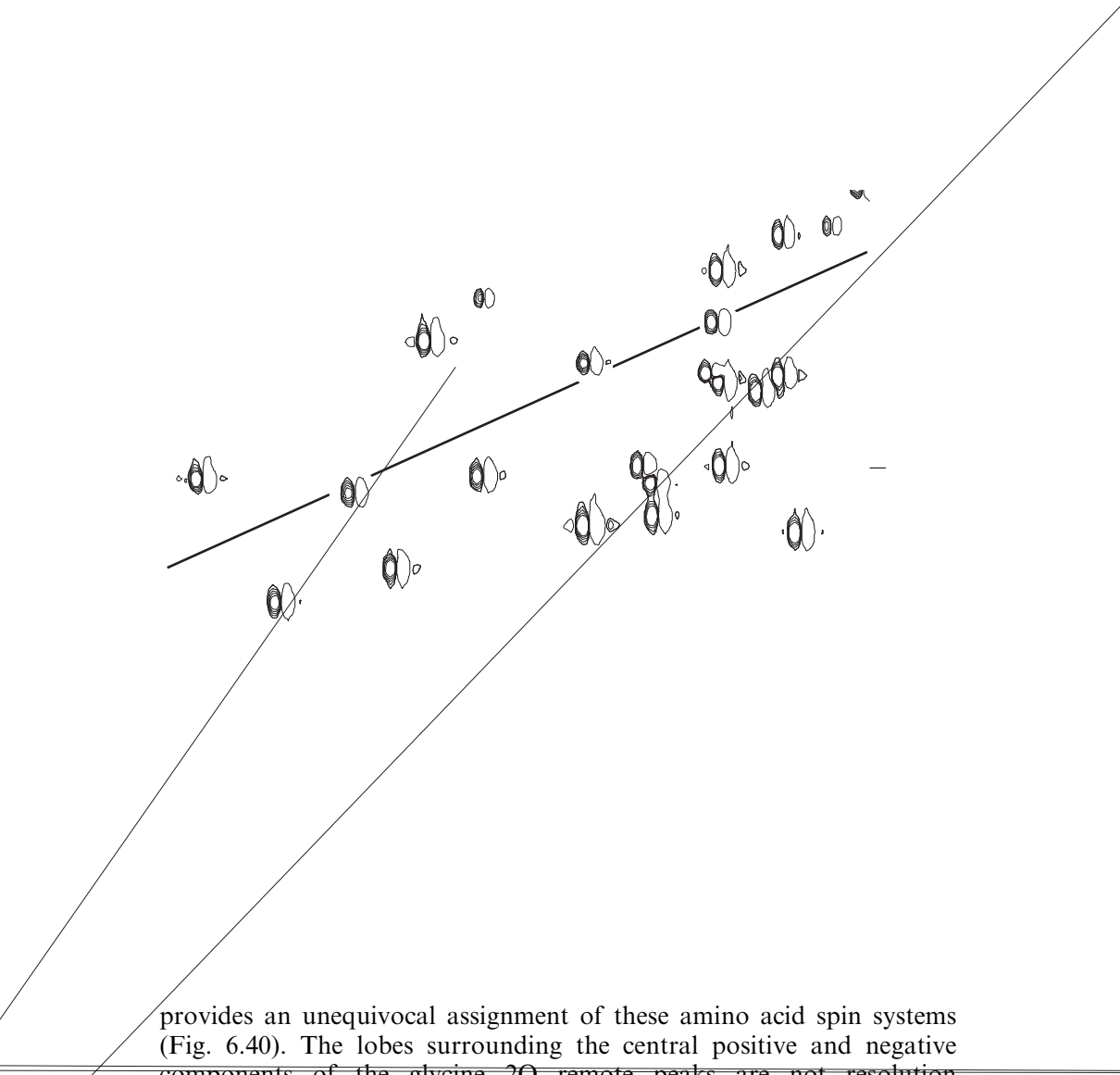

provides an unequivocal assignment of these amino acid spin systems (Fig. 6.40). The lobes surrounding the central positive and negative components of the glycine 2Q remote peaks are not resolution enhancement artifacts, but are actually the result of the natural dispersive double antiphase lineshape in F_2 and dispersive antiphase lineshape in F_1 (see Fig. 6.36).

In all residues except glycine and proline, the $^1H^{\alpha}$ spin is coupled to both $^1H^N$ and at least one $^1H^{\beta}$, hence remote peaks at $F_1 = {}^1H^N + {}^1H^{\beta}$ are expected at $F_2 = {}^1H^{\alpha}$. Such peaks provide a useful means of correlating an $^1H^N$ spin directly with an $^1H^{\beta}$ spin in the same spin system. Unfortunately, the usefulness is compromised by the water stripe present at $F_2 = \delta(H_2O)$, which will obscure many $^1H^{\alpha}$ resonances; as a result, $^1H^N$–$^1H^{\beta}$ correlations are more readily established in TOCSY (Section 6.5) or relayed COSY (Section 6.2.2) spectra.

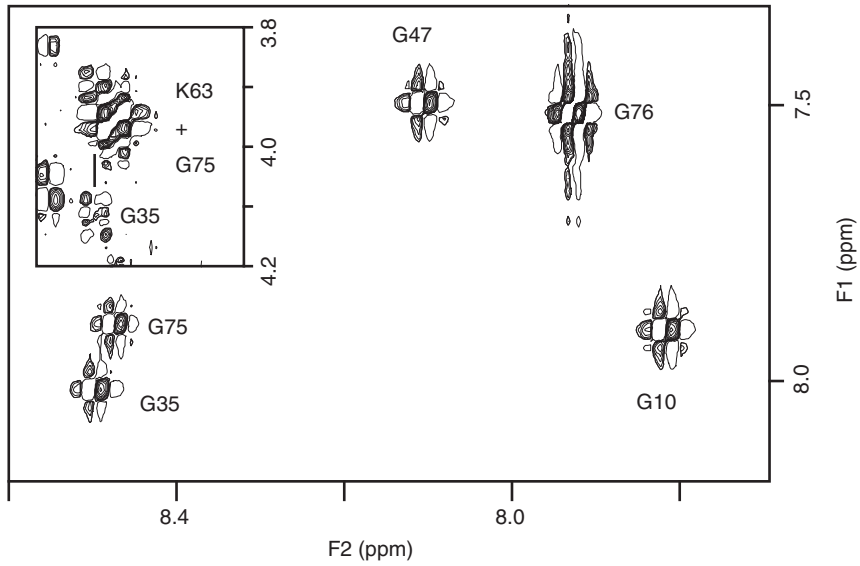

FIGURE 6.40 Section of the H_2O 2Q spectrum of ubiquitin ($\tau = 22$ ms) showing the remote glycine peaks at $F_1 = {}^1H^{\alpha'} + {}^1H^{\alpha''}$. The peaks from five of the six glycine residues are clearly present and labeled. The amide proton of the remaining glycine (Gly53) is unusually broad, and no cross-peaks involving it are observed in any of the correlation spectra. The inset shows the cross-peaks of Gly35 and Gly75 in the COSY spectrum. The degeneracy of $^1H^{\alpha'}$ and $^1H^{\alpha''}$ of Gly75 and the overlap with Lys63 $^1H^N$–$^1H^\alpha$ in the COSY are confirmed by the presence of the 2Q remote peak.

The $^1H^\alpha$–$^1H^\beta$ peaks form the main fingerprint region of interest in the upfield region of the 2Q spectrum and are most easily observed in D_2O solution at the F_2 shift of the $^1H^\alpha$ resonances. This region of the COSY spectrum is normally crowded, making the observation of all $^1H^\alpha$–$^1H^\beta$ cross-peaks problematic. In addition, for β-methylene-containing side chains, one of the $^1H^\alpha$–$^1H^\beta$ coupling constants frequently is small; thus, only one of the two expected peaks may be observed in COSY spectra. Although the direct $^1H^\alpha$–$^1H^\beta$ peaks in the 2Q spectrum are equally crowded and possibly weak, the remote peaks are not; hence, observation of the remote peak and one direct peak allows assignment of all three resonance positions (Fig. 6.41).

Commonly, resonance positions within a side chain will be inferred from correlations relayed to the amide proton in TOCSY experiments

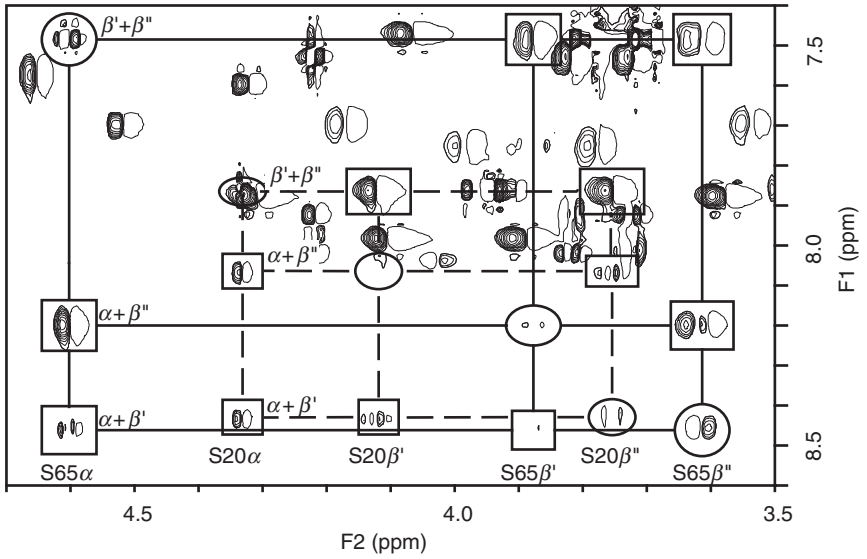

FIGURE 6.41 Example of remote and direct peaks for $C^{\alpha}H$–$C^{\beta}H_2$ fragments in the D_2O 2Q spectrum ($\tau = 30$ ms). Squares and ellipses indicate direct and remote correlations, respectively. The cross-peaks arising from Ser65 and Ser20 are connected by solid and dashed lines, respectively. The F_1 and F_2 frequencies are indicated adjacent to the lines connecting the cross-peaks. For this value of τ, the direct and remote peaks are distinguished by virtue of the opposite phase in F_2 (see text).

acquired in H_2O. Although chemical shift arguments allow assignment of the cross-peaks to a particular side chain resonance, this process is fallible. Discriminating $^1H^{\beta}$ and $^1H^{\gamma}$ resonances within five-spin residues is one case where such a simple analysis commonly leads to incorrect side-chain assignments. Thus, the unambiguous determination of $^1H^{\beta}$ resonance positions in the 2Q spectrum provides a useful complement to other relay-based techniques (e.g., see Fig. 6.42). Indeed, during the analysis of spectra for this book, several $^1H^{\beta}$ resonances that had not been assigned previously were observed in MQ spectra (*46*, *47*).

Loss of signal intensity due to chemical exchange broadening (Section 5.6) frequently causes difficulties when analyzing standard 2D spectra such as COSY or 2QF-COSY. Under appropriate conditions, the 2Q experiment provides valuable assistance in such cases. One example is provided by the following situation (*48*). Double-quantum coherence between two spins, A and B, evolves at the sum,

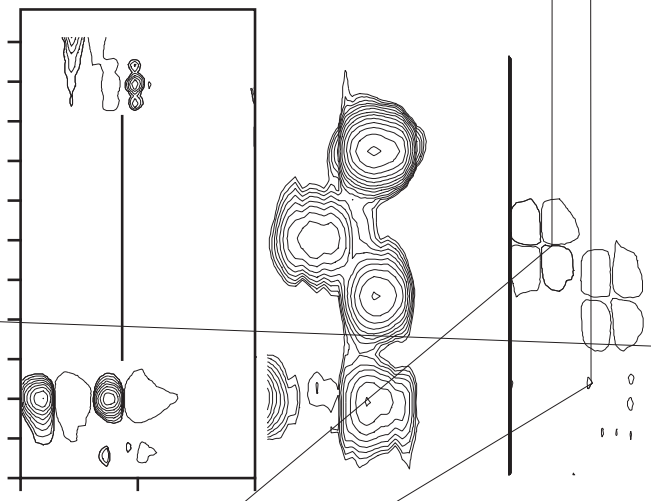

$\Omega_A + \Omega_B$, of their respective single-quantum frequencies. This sum frequency is unaffected by mutual exchange of the A and B spins; therefore, double-quantum coherence is insensitive to the exchange process. The direct peaks involving spins A and B will still be exchange broadened in the observed dimension F_2. However, if the double-quantum coherence is transferred to a third spin C that is coupled to both A and B, and if this third spin is not involved in the exchange process, then a remote peak will be observable at the frequencies $\Omega_A + \Omega_B$ in F_1 and Ω_C in F_2. This scenario occurs for phenylalanine aromatic ring spin systems. The two $^1H^{\varepsilon}$ spins interchange as a result of 180° flips of the ring, but the $^1H^{\zeta}$ proton is unaffected. Consequently, the remote peak at the sum of the two $^1H^{\varepsilon}$ frequencies in F_1 and the $^1H^{\zeta}$ frequency in F_2 is insensitive to the exchange process.

The 2Q experiment has an additional advantage for exchange-broadened resonances because double-quantum peaks mostly have an

in-phase multiplet structure. Thus the double-quantum peaks are less sensitive to self-cancellation as the linewidth increases, compared to cross-peaks with antiphase multiplet structure in COSY or 2QF-COSY experiments. Loss of signal intensity due to the effects of chemical exchange during the preparation period can be reduced by employing multiple refocusing pulses (*49*) or by using a Hartmann–Hahn mixing sequence (*50*).

6.4.2 3Q SPECTROSCOPY

As with 2QF- and 3QF-COSY, the 2Q experiment is just one of many experiments based on observation of multiple-quantum states. Multiple-quantum states higher than 3Q, although attainable theoretically, are rarely applied to protein systems. Thus, the 3Q experiment is the focus of this section. The full phase cycle for the 3Q experiment was described in the caption to Fig. 6.34.

6.4.2.1 Product Operator Analysis Due to the similarity of the initial parts of the 2Q and 3Q pulse sequences, evolution of the product operators is the same up to the end of the $90^\circ_x - \tau/2 - 180^\circ_x - \tau/2$ sequence. At this point, a 90°_y pulse must be applied in order to generate odd orders of multiple-quantum coherence. Thus, the following operators are obtained for a three-spin system (I_1, I_2, and I_3):

$$\begin{aligned} I_{1z} \xrightarrow{\left(\frac{\pi}{2}\right)_x - \frac{\tau}{2} - \pi_x - \frac{\tau}{2} - \left(\frac{\pi}{2}\right)_y} & I_{1y} \cos(\pi J_{12}\tau) \cos(\pi J_{13}\tau) + 2I_{1z}I_{2x} \sin(\pi J_{12}\tau) \\ & \times \cos(\pi J_{13}\tau) + 2I_{1z}I_{3x} \cos(\pi J_{12}\tau) \sin(\pi J_{13}\tau) \\ & - 4I_{1y}I_{2x}I_{3x} \sin(\pi J_{12}\tau) \sin(\pi J_{13}\tau). \end{aligned} \quad [6.39]$$

The 3Q phase cycle suppresses the first three terms of [6.39]. The fourth term is a mixture of $3Q_y$ and three-spin single-quantum coherence; a similar operator was encountered in the analysis of the 3QF-COSY experiment (Section 6.3.2.1). Once again, phase cycling retains only the pure three-quantum term and only its evolution needs to be considered during t_1:

$$\begin{aligned} 3Q_y \sin(\pi J_{12}\tau) \sin(\pi J_{13}\tau) \xrightarrow{t_1} & 3Q_y \cos(\Omega_{123}t_1) \sin(\pi J_{12}\tau) \sin(\pi J_{13}\tau) \\ & - 3Q_x \sin(\Omega_{123}t_1) \sin(\pi J_{12}\tau) \sin(\pi J_{13}\tau), \end{aligned} \quad [6.40]$$

where $\Omega_{123} = \Omega_1 + \Omega_2 + \Omega_3$. Application of the final 90°_y pulse to the Cartesian single operator components of [6.40] produces the following operators prior to t_2:

$$\begin{aligned}&\left[-4I_{1z}I_{2y}I_{3z} - 4I_{1y}I_{2z}I_{3z} - 4I_{1z}I_{2z}I_{3y} + 4I_{1y}I_{2y}I_{3y}\right]\\&\quad\times \cos(\Omega_{123}t_1)\,\sin(\pi J_{12}\tau)\,\sin(\pi J_{13}\tau)\\&\quad+\left[4I_{1z}I_{2z}I_{3z} - 4I_{1y}I_{2y}I_{3z} - 4I_{1z}I_{2y}I_{3y} - 4I_{1y}I_{2z}I_{3y}\right]\\&\quad\times \sin(\Omega_{123}t_1)\,\sin(\pi J_{12}\tau)\,\sin(\pi J_{13}\tau).\end{aligned} \qquad [6.41]$$

The fourth term on line 1 and all four terms on line 3 of [6.41] are unobservable operators. The first three terms on line 1 give rise to observable peaks at the chemical shifts of each of the three spins in F_2 and at the sum of their chemical shifts in F_1. In F_2, each peak is doubly antiphase with respect to the other two spins, whereas in F_1, all three peaks are singlets without fine structure and can be phased to absorption.

The preceding product operator analysis has been extended to include additional passive spins to give results applicable to other spin systems (*51*). Thus, the contribution of spin I_1 to the 3Q coherence $(I_1 + I_2 + I_3)$ is described by

$$A_1 = \sin(\pi J_{12}\tau)\,\sin(\pi J_{13}\tau)\prod_{k=4}^{K}\cos(\pi J_{1k}\tau), \qquad [6.42]$$

in which I_1, I_2, and I_3 are active spins and all spins, I_k, for $k > 3$, are passive spins. If all three active spins are passively coupled to a fourth spin, I_4, then I_4 also contributes to the 3Q coherence $(I_1 + I_2 + I_3)$ in the following manner:

$$A_4 = \sin(\pi J_{14}\tau)\,\sin(\pi J_{24}\tau)\,\sin(\pi J_{34}\tau)\prod_{k=5}^{K}\cos(\pi J_{4k}\tau). \qquad [6.43]$$

These expressions have been used to generate excitation profiles as a function of τ for the spin systems and coupling constants commonly found in amino acids (*51*).

By considering evolution of the density matrix during a multiple-quantum experiment, Braunschweiler et al. (*41*) have described two selection rules for the peaks observed in such spectra: (*i*) multiple-quantum coherence involving a set of q spins can only be transferred to

the single quantum transitions of a spin I when the scalar couplings between I and *all* q spins are resolved (if I belongs to the set of q spins, only the couplings to the remaining $q-1$ spins need be resolved), and (*ii*) multiple-quantum coherence involving two or more equivalent nuclei cannot be transferred to the single-quantum coherence of the equivalent nuclei because couplings between magnetically equivalent nuclei are ineffective in isotropic solution phase. As in the case of multiple-quantum filtered COSY experiments, violations of the second selection rule by methyl groups in proteins are manifestations of multiexponential relaxation (*35*).

6.4.2.2 Experimental Protocol and Processing Carrier positions and spectral widths are chosen in a manner analogous to the methods described in the preceding section for the 2Q experiment. The principal difference is that now F_1 peak positions occur at the sum of three chemical shifts. Considering only the aliphatic resonances (i.e., folding the aromatic signals in F_1), the downfield spectral limit will be at the sum of H^{α}, $H^{\beta'}$, and $H^{\beta''}$ chemical shifts. The largest sum usually arises from serine residues. As 3Q coherences are now evolving during t_1, the phases of all pulses prior to t_1 must be incremented by $\pi/(2|p|)=\pi/6$ in order to achieve quadrature detection (Section 4.3.4.1). Generally, $\tau=30$ to 36 ms; additional detail is given in Section 6.4.2.3. Other details of the experimental protocol are similar to those already described above for the 2Q experiment (Section 6.4.1.2).

The sections of spectra shown in Fig. 6.43 were obtained in about 16 hours on a 2 mM ubiquitin sample in D_2O solution using a preparation period of $\tau=36$ ms; 48 transients were collected for each of 600 t_1 increments using a spectral width of 7000 Hz in F_1 ($t_{1\max}=43$ ms). The carrier was shifted from the water resonance to 2.0 ppm at the start of the pulse sequence and the aromatic resonances were folded in F_1. The experiment was acquired with TPPI quadrature detection in F_1.

Window functions applied in F_2 are chosen in a fashion similar to those chosen for the 2Q experiment (Section 6.4.1.3). Phase parameters are chosen to give a symmetric three-lobed profile for direct peaks in this dimension (formally an absorptive double antiphase lineshape; Fig. 6.36). Given the predominantly absorptive lineshape in F_1, processing in this dimension should be sufficient to prevent truncation, and possibly to provide slight resolution enhancement (e.g., sine bells shifted by 60° to 90°). The center of the spectrum in F_1 is referenced to three times the carrier frequency.

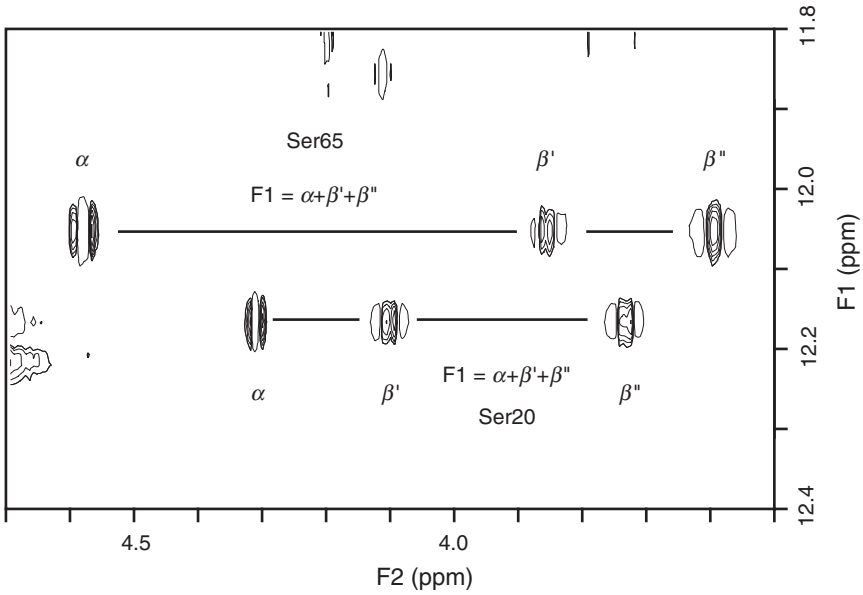

FIGURE 6.43 Demonstration of the spectral simplification achieved for a spin system containing three coupled spins in a 3Q spectrum; only three direct peaks are expected for such systems. Spin systems of Ser20 and Ser65 are shown (for comparison, the 2Q cross-peaks arising from these residues are depicted in Fig. 6.41).

6.4.2.3 Information Content The justifications for using 3Q experiments are twofold. First, moving to a higher quantum state results in spectral simplification because some spin systems cannot attain the requisite level of coherence (much as the 3QF-COSY offers advantages over the 2QF-COSY). Second, the remote peaks present in the 3Q spectrum offer unique assignment information. Even for spin systems that are present in *p*QF-COSY or 2Q spectra, the 3Q experiment may offer considerable simplification. For example, Fig. 6.43 depicts the correlations arising from the spin systems of Ser20 and Ser64; each spin system leads to three direct peaks only. Comparable regions of other spectra contain larger numbers of peaks: the COSY spectra contains six cross-peaks and three diagonal peaks and the 2Q contains six direct and three remote peaks. The simplification makes observation of the spin systems of Ser20 and Ser64 very straightforward (e.g., compare with Fig. 6.41).

The three main uses for the 3Q spectrum are (*i*) verification of $^1H^{\alpha}$ and $^1H^{\beta}$ resonance assignments made in other spectra, (*ii*) identification of resonance positions for phenylalanine and tryptophan ring protons, and (*iii*) identifying cases of resonance degeneracy at the end of longer spin systems (five-spin, lysine, arginine, and proline residues).

Amide protons of glycine residues contribute to a direct 3Q coherence ($F_1 = {}^1H^N + {}^1H^{\alpha'} + {}^1H^{\alpha''}$; $F_2 = {}^1H^N$, $^1H^{\alpha'}$, or $^1H^{\alpha''}$) that allows determination of all three chemical shifts; this information is obtained equally well from the remote peaks in a 2Q spectrum (Section 6.2.3.4). In the case of residues other than glycine or proline, an amide proton contributes to a direct ($F_1 = {}^1H^N + {}^1H^{\alpha} + {}^1H^{\beta}$) peak, and if the amino acid contains a β-methylene group, a remote peak ($F_1 = {}^1H^N + {}^1H^{\beta'} + {}^1H^{\beta''}$). The former correlations have excitation maxima in the range $\tau = 30$–40 ms, while the latter are maximized for $\tau = 40$–50 ms (*51*). From the multiple-quantum selection rules, the 3Q coherence is observable only at $F_2 = {}^1H^{\alpha}$ in both of these cases. Not all of these correlations are observed in spectra acquired from H_2O solution because of interference from the water resonance.

The main peaks of interest in a 3Q spectrum acquired from D_2O solution are (*i*) coherences involving $^1H^{\alpha}$ and $^1H^{\beta}$ protons, (*ii*) coherences arising from the aromatic resonances of tryptophan and phenylalanine residues, and (*iii*) coherences involving the terminal protons of lysine ($^1H^{\delta} + {}^1H^{\varepsilon'} + {}^1H^{\varepsilon''}$ and $^1H^{\delta'} + {}^1H^{\delta''} + {}^1H^{\varepsilon}$), arginine, and proline ($^1H^{\gamma} + {}^1H^{\delta'} + {}^1H^{\delta''}$ and $^1H^{\gamma'} + {}^1H^{\gamma''} + {}^1H^{\delta}$) residues. Using the analytical expressions [6.42] and [6.43], values of τ to provide optimal intensity of these correlations can be deduced (*51*). Regardless of the size of $^3J_{H^{\alpha}H^{\beta}}$ and extensions of the spin system beyond $^1H^{\beta}$, the intensities of the $^1H^{\alpha} + {}^1H^{\beta'} + {}^1H^{\beta''}$ coherences are maximal at $\tau = 30$ ms except for serine residues, for which the smaller geminal $^1H^{\beta'}$–$^1H^{\beta''}$ coupling leads to maximal intensity at $\tau = 40$ ms. The linear and aromatic spin systems have a broad maximum centered at $\tau = 65$ ms. Thus, all types of correlations should be detectable for τ in the 30- to 40-ms range.

The efficiency of excitation for the terminal protons of longer side chains is harder to categorize because of the influence of contributions from passive spins. The various active and passive contributions have very different F_1 lineshapes that can lead to severe cancellation for some values of τ. This complex behavior also is very dependent on the exact linewidths of the resonances involved because the dispersive terms are also prone to self-cancellation. In summary, a value of $\tau = 36$ ms is appropriate for most aliphatic side chain correlations (*23*). Acquisition of experiments with longer or shorter values of τ may be necessary to observe all correlations involving the terminal groups of arginine,

proline, and lysine. The work of Chazin should be consulted when optimizing τ for a particular correlation (*51*). The 3Q correlations among resonances at the termini of longer side chains provide one of the few ways to positively identify resonance degeneracy (*51*). However, the number of possible 3Q frequencies can be large, and the ability to obtain useful assignment information will depend on the particular distributions of chemical shifts.

The aromatic regions of 3Q spectra are usually quite simple, as they only contain peaks from phenylalanine or tryptophan residues. For phenylalanine residues, direct peaks arising from three-bond scalar coupling interactions are observed at (F_1, F_2) frequencies of ($\Omega_\delta + \Omega_\varepsilon + \Omega_\zeta$, Ω_ε) and ($\Omega_\delta + \Omega_\varepsilon + \Omega_\varepsilon$, Ω_ζ). Additional direct and remote peaks are observed if long-range four-bond or five-bond scalar couplings are resolved. Resonances from the aromatic ring of tyrosine are absent unless the long-range $^4J_{H^{\delta 1}H^{\delta 2}}$ or $^4J_{H^{\varepsilon 1}H^{\varepsilon 2}}$ couplings are resolved. This region of the ubiquitin 3Q spectrum is further simplified by the degeneracy of H^ε and H^ζ of one of the two phenylalanine residues (Fig. 6.44).

6.5 TOCSY

Soon after the introduction of the R.COSY and related experiments (Sections 6.2.2 and 6.2.3), a new method of obtaining relayed connectivities was introduced, namely, Total Correlation Spectroscopy (TOCSY) (*52*). This technique is also known by the acronym HOHAHA (homonuclear Hartmann–Hahn) spectroscopy (*53*). Instead of relying on pulse-interrupted free-precession sequences to transfer coherence between antiphase states (Section 4.2.1.1), TOCSY utilizes isotropic mixing to transfer in-phase magnetization between spins via the strong scalar coupling Hamiltonian (Section 4.2.1.2), with the result that magnetization can be transferred through several couplings during the course of the mixing period. In the absence of relaxation, cross-peaks potentially are generated between all resonances within a spin system.

6.5.1 PRODUCT OPERATOR ANALYSIS

The TOCSY experiment can be performed in numerous ways. In the method described here, after frequency labeling during t_1, magnetization is returned to the z-axis for isotropic mixing using the relaxation-compensated DIPSI-2 (DIPSI-2rc) or other mixing sequence, and then returned to the transverse plane for detection (*54*). In addition to several

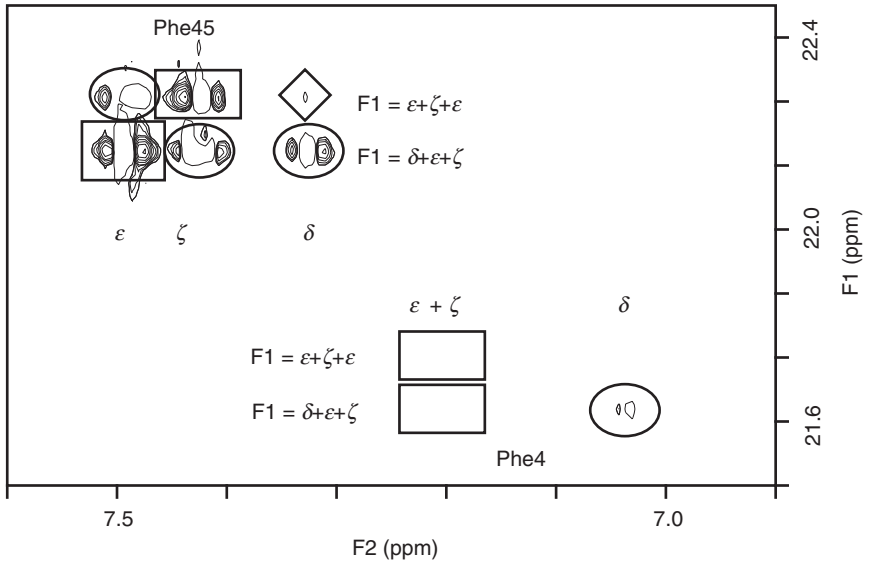

FIGURE 6.44 Section of the 3Q spectrum of ubiquitin in D_2O solution showing the aromatic side chain resonances. Direct peaks arising from three-bond scalar coupling interactions are indicated by rectangles; direct peaks that result from at least one resolved four-bond scalar coupling are indicated by ellipses; a remote peak arising from other long-range scalar couplings is indicated by a diamond. Peaks from Phe45 are readily apparent, whereas the degeneracy of $^1H^{\varepsilon}$ and $^1H^{\zeta}$ for Phe4 prevents the generation of 3Q coherence, hence the direct peaks are not observed. In the absence of resolved four-bond scalar couplings, no correlations are observed for Tyr59.

advantages described here, this method also enables the addition of a Hahn echo at the end of the sequence to provide a flatter baseline (Section 3.6.4.2). The pulse sequence, coherence level diagram, and phase cycle for such an experiment are shown in Fig. 6.45. If a probe equipped with pulsed field gradients is available, then pulsed field gradients can be used for artifact and solvent suppression. The pulse sequence, coherence level diagram, and phase cycle for an experiment that incorporates the excitation sculpting water suppression technique are shown in Fig. 6.46. The phase cycling used in these versions of the TOCSY experiment is identical to that developed for the NOESY experiment, and is discussed in more detail in Section 6.6.

Following the 90°_x–t_1–90°_x sequence, the density operator is described by [6.1]. The I_{1x} and $2I_{1z}I_{2y}$ terms in [6.1] are eliminated by the TOCSY phase cycle or the gradient pulse G1. The DQ component of

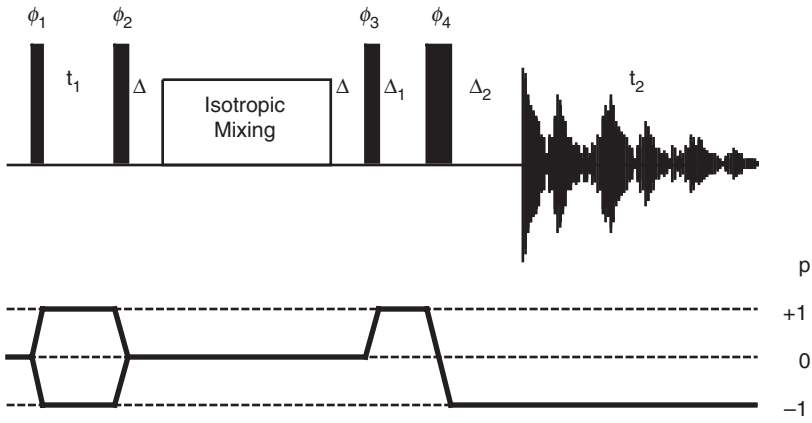

FIGURE 6.45 Pulse sequence and coherence level diagram for the TOCSY experiment. A Hahn echo is included prior to detection. The basic eight steps of the phase cycle are $\phi_1 = 2(x, -x, -x, x)$; $\phi_2 = 2(x, x, -x, -x)$; $\phi_3 = 8(x)$; $\phi_4 = 4(y)$, $4(-y)$; and receiver $= 4(x, -x)$; the full 32-step phase cycle is completed by performing CYCLOPS on all pulses and the receiver. The delay Δ allows the transmitter power to be changed and is short enough ($\approx 20\,\mu$s) to prevent development of NOE cross-peaks. Frequency discrimination in F_1 is obtained by shifting the phase of ϕ_1 and the receiver according to the TPPI, States, or TPPI–States protocols (Section 4.3.4).

the term $2I_{1x}I_{2y}$ is dephased by the rf inhomogeneity present during the isotropic mixing pulse sequence of duration τ_m (Section 3.5.3). During the isotropic mixing sequence, magnetization proportional to I_{1z} is transferred throughout the spin system via the strong coupling Hamiltonian as described in Section 4.2.1.2:

$$-I_{1z}\cos(\Omega_I t_1)\cos(\pi J_{12} t_1) \xrightarrow{\tau_m} -\sum_{k=1}^{K} I_{kz} a_{1k}(\tau_m)\cos(\Omega_I t_1)\cos(\pi J_{12} t_1), \qquad [6.44]$$

in which $a_{1k}(\tau_m)$ are mixing coefficients for transfer of magnetization through the spin system from spin I_1 to spin I_k, and zero-quantum terms (Section 4.2.1.2) have been ignored. Following the final 90°_x pulse and the Hahn echo or excitation sculpting sequence, the density operator prior to t_2 is given by

$$\sum_{k=1}^{K} I_{ky} a_{1k}(\tau_m)\cos(\Omega_I t_1)\cos(\pi J_{12} t_1). \qquad [6.45]$$

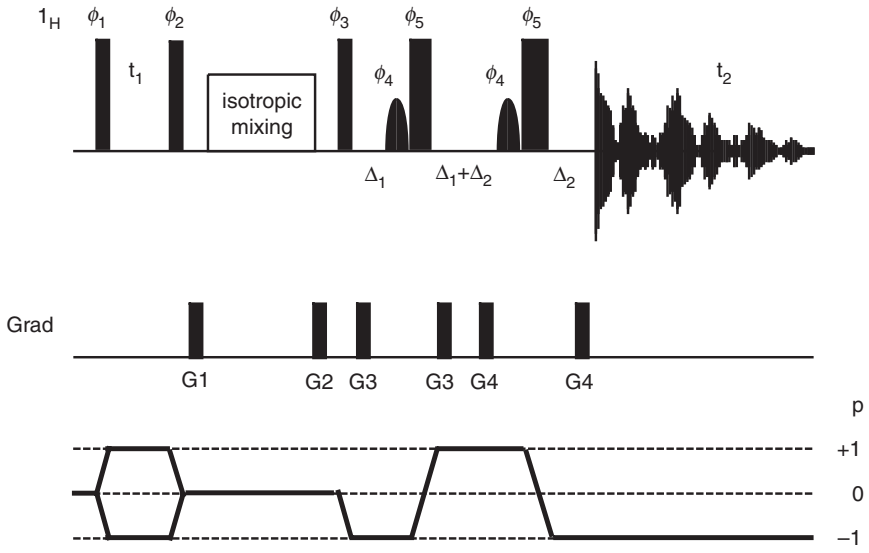

FIGURE 6.46 Pulse sequence and coherence level diagram for a TOCSY experiment using excitation sculpting to avoid presaturation of the solvent resonance. The curved pulse shapes indicate selective 180° pulses at the water frequency. The basic eight steps of the phase cycle are $\phi_1 = 2(x, -x, -x, x)$; $\phi_2 = 2(x, x, -x, -x)$; $\phi_3 = 8(x)$; $\phi_4 = 4(-y), 4(y)$, $\phi_5 = 4(y), 4(-y)$; and receiver $= 4(x, -x)$; the full 32-step phase cycle is completed by performing CYCLOPS on all pulses and the receiver. Delays before and after mixing allow the transmitter power to be changed and are short enough ($\approx 20\,\mu$s) to prevent development of NOE cross-peaks. Frequency discrimination in F_1 is obtained by shifting the phase of ϕ_1 and the receiver according to the TPPI, States, or TPPI–States protocols (Section 4.3.4). A bipolar pair of gradients can be inserted into the t_1 period to prevent radiation damping (*31*).

The term proportional to I_{1y} represents the diagonal peak, and the terms proportional to I_{ky} for $k \neq 1$ represent cross-peaks. The observation of a cross-peak between two spins in the TOCSY experiment does not indicate that the spins are directly coupled; rather, the cross-peak indicates that magnetization can be transferred between the two spins by a series of steps through two- and three-bond scalar couplings between mutually coupled spins.

The magnitudes of the cross-peaks [governed by $a_{ij}(\tau_m)$] depend upon the topology of the spin system, the coupling constants between pairs of spins, the efficiency of the isotropic mixing sequence employed,

and the rate of relaxation during the isotropic mixing pulse. The mixing coefficients usually satisfy $a_{ij}(\tau_m) > 0$, but $a_{ij}(\tau_m) < 0$ can arise for certain scalar coupling topologies (*55*). Numerical calculations based on density matrix theory have been used to calculate the transfer efficiencies for the coupling networks expected in naturally occurring amino acids using scalar coupling constants representative of a variety of conformations present in proteins (*56*). Such data are of much value in choosing an appropriate mixing time, as will be discussed in the next section.

Inspection of [4.16] indicates that the mixing process also leads to the transfer of zero-quantum coherence that gives rise to antiphase components in both the cross-peaks and the diagonal peaks. The 90° phase difference between the in-phase and antiphase components indicates that when the former are phased to absorption, the latter will produce dispersive tails spreading out from peaks in the TOCSY spectrum. Fortunately, the resonance linewidths present in most proteins are sufficiently broad that these antiphase components of the peak are reduced by self-cancellation. One advantage of performing the experiment in the manner indicated in Fig. 6.45 is that the size of the antiphase components may be further reduced by varying the delays on either side of the isotropic mixing period over the course of the experiment. This process is known as "*z*-filtration" (*54*, *57*), and is analogous to techniques for suppression of zero-quantum peaks in NOESY spectra. A more complete discussion is given in Section 6.6.1.

The choice of appropriate isotropic mixing sequence has been the subject of much research (*58*). The first successful mixing sequences were derived from phase-modulated irradiation schemes used for spin decoupling, such as MLEV-17 (*53*) and WALTZ-16 (*59*, *60*) (Section 3.4.3). Recently, many pulse sequences have been developed that are isotropic over wide frequency ranges with minimal power requirements. The most popular of these, at present, are the DIPSI (*61*, *62*) and flip-flop spectroscopy (FLOPSY) (*63*) family of pulse sequences developed by Shaka and co-workers. The DIPSI-2 sequence is given by the pulse sequence element

$$R = 320\ \overline{410}\ 290\ \overline{285}\ 30\ \overline{245}\ 375\ \overline{265}\ 370, \qquad [6.46]$$

in which pulse lengths are given in degrees and overbars indicate 180° phase shifts. As is the case for broadband excitation (Section 3.4.4) and spin decoupling (Section 3.4.5), adiabatic pulses also have been incorporated into isotropic mixing schemes (*64–67*). Adiabatic mixing schemes are less sensitive to mis-setting of the B_1 field than are conventional mixing sequences. Just as in the case for spin decoupling

(Section 3.4.5), the performance of isotropic mixing sequences is improved by combining the basic pulse sequence element into a supercycle $R\bar{R}\bar{R}R$. The performance of mixing sequences is difficult to establish by product operator analysis. Instead, the efficiency of coherence transfer is calculated numerically as a function of resonance offsets using the full density matrix formalism. Panels b–f in Fig. 6.47 illustrate the efficiency of coherence transfer for the MLEV-17, WALTZ-16, DIPSI-2, FLOPSY-16, and WURST-2 adiabatic isotropic mixing sequences. MLEV-17 and WALTZ-16 provide significantly less efficient coherence transfer than do more modern sequences.

The initial orientation of the proton magnetization must be considered when applying a given TOCSY mixing sequence. If the z-filtered version of the TOCSY experiment, Fig. 6.45, is used, then the initial magnetization is aligned along the $+z$ or $-z$ axes, whereas if z-filters are not employed, the initial magnetization normally is oriented in the transverse plane. Some sequences, such as WALTZ-16 or DIPSI-2, can work equally well in these two situations. However, in the second case, the initial magnetization must be aligned orthogonally to the mixing sequence, i.e., along the $\pm y$ axes if the rf pulses of the mixing scheme are applied along the $\pm x$ axes. In contrast, sequences such as FLOPSY and adiababtic mixing require that the initial magnetization is aligned along the $\pm z$ axes, and MLEV-17 requires that the initial magnetization is aligned parallel to, or antiparallel to, the axis along which the 17th pulse is applied. Magnetization should never be spin-locked along a transverse axis, because magnetization then decays subject to (rapid) spin–spin relaxation processes; when properly aligned, the net relaxation behavior of the magnetization is determined by a combination of (rapid) spin–spin and (slow) spin–lattice relaxation processes (*68*).

The most recent isotropic mixing schemes not only have desirable magnetization transfer properties, but also minimize transfer via dipolar coupling during the mixing period (via the rotating-frame Overhauser effect, or ROE; Section 5.4.3) (*69*). Direct ROE peaks and the TOCSY peaks are of opposite sign, and the ROE peaks may attenuate or completely cancel TOCSY cross-peaks between proximal spins within the same spin system. The dipolar effects are particularly problematic during the long mixing times required to see all correlations in extended spin systems and are also more acute for large proteins because dipolar relaxation is more efficient. The ''clean'' isotropic mixing sequences take advantage of the difference in sign of the NOE (laboratory-frame Overhauser effect) and the ROE [5.155]. By placing suitable delays in the pulse train, NOEs develop that offset the ROE contributions. The two

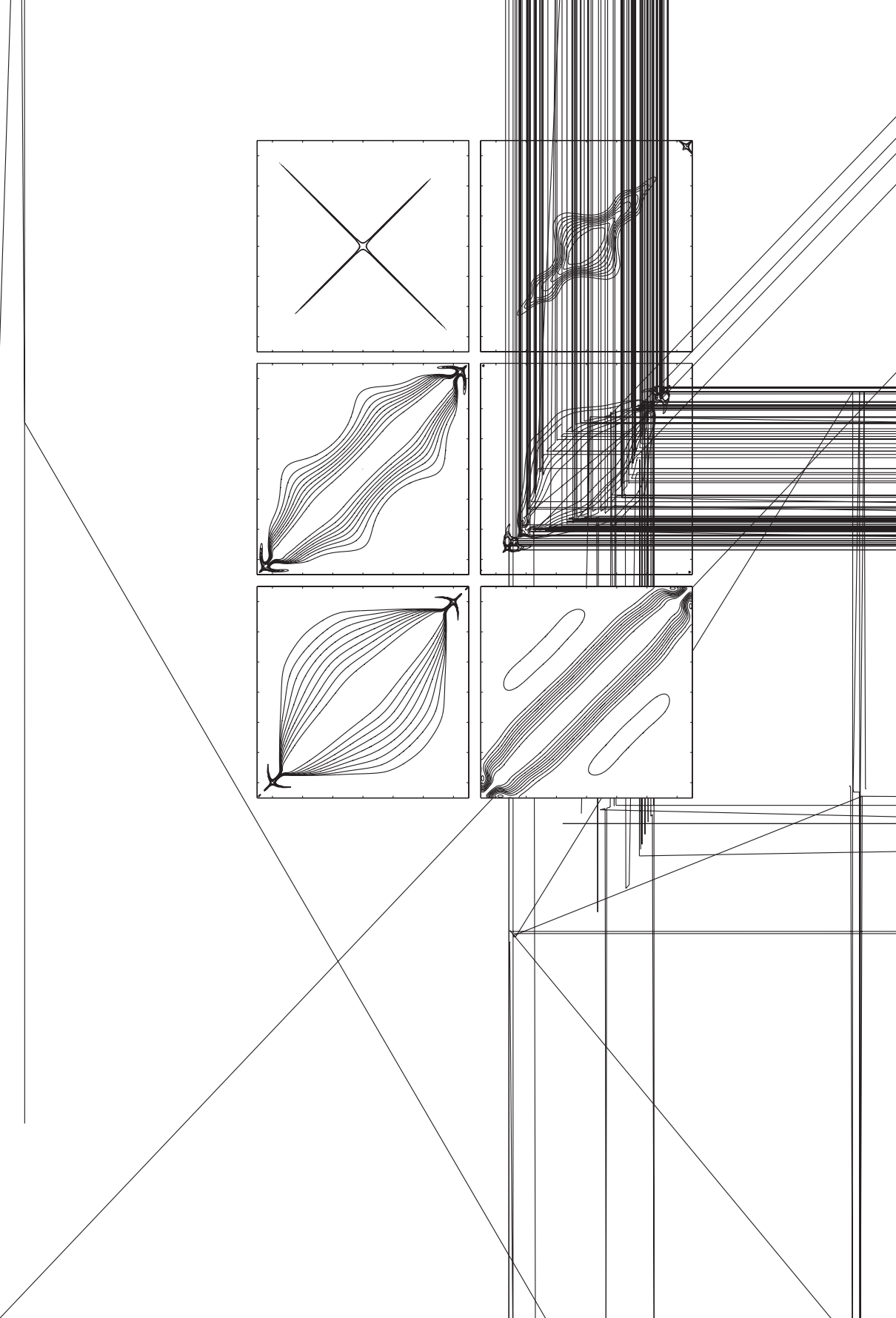

most widely used sequences in this respect are the DIPSI-2rc sequence (*70*) and the clean CITY sequence (*71*). Schemes also have been designed that achieve compensation between ROE and NOE effects without introducing delays during the mixing sequence (*72*). Clean adiabatic mixing sequences based on the WURST-2 pulse have been described (*64*, *67*). The supercycle sequence of the "clean" DIPSI-2rc sequence is $R\bar{R}\bar{R}R$, in which

$$\begin{aligned} R = {} & 180^\circ\text{–}\Delta\text{–}140^\circ\text{–}\overline{320^\circ}\text{–}\Delta\text{–}\overline{90^\circ}\text{–}270^\circ\text{–}\Delta\text{–}20^\circ\text{–}\overline{200^\circ} \\ & \text{–}\Delta\text{–}\overline{85^\circ}\text{–}30^\circ\text{–}\overline{125^\circ}\text{–}\Delta\text{–}\overline{120^\circ}\text{–}300^\circ\text{–}\Delta\text{–}75^\circ\text{–}\overline{255^\circ} \\ & \text{–}\Delta\text{–}\overline{10^\circ}\text{–}190^\circ\text{–}\Delta\text{–}180^\circ\text{–}\Delta, \end{aligned} \qquad [6.47]$$

and should be compared with the original DIPSI-2 sequence [6.46]. The delays Δ occur when (for ideal rotations) magnetization is aligned along the z-axis to permit compensatory NOE cross-relaxation. The delay Δ has a nominal duration equal to the length of a 143.87° pulse. None of these schemes is capable of suppressing transfer via chemical exchange (Section 5.6). The effect of such a process on the peaks observed in a TOCSY spectrum has been described by Feeney and co-workers (*73*). Discrimination of chemical exchange peaks is discussed in more detail in Section 6.6.2.4.

6.5.2 Experimental Protocol

In all of the experiments described so far in this chapter, cross-peaks have had antiphase lineshapes in F_2. This fact, coupled with the severely resolution-enhancing window functions used during processing, means little attention was paid to the quality of the baseline in the resulting spectra. Provided the spectrometer is reasonably well shimmed to minimize the residual water resonance, the baselines will be flat and the cross-peaks will be easily visible. In contrast, after the t_2 Fourier transformation of a 2D TOCSY spectrum, the peaks in each F_2 slice are in-phase and absorptive. Thus, they have many similarities with 1D spectra, including many of the same problems of baseline distortion discussed in Section 3.3. Upon Fourier transformation in t_1, the baseline distortions, which tend to vary between t_1 increments, are manifested as alternating positive and negative ridges running parallel to the F_2 axis. In severe cases, the cross-peaks are obscured. In order to obtain the flattest baseline possible in absorptive homonuclear experiments such as TOCSY, the following points should be considered: (*i*) shim the sample with the specific aim of reducing the residual water signal

remaining after presaturation (Section 3.6.2.2), (*ii*) replace the final 90° pulse with a Hahn echo (Section 3.6.4.2) or pulsed field gradient water-suppression technique (Section 3.7.3), (*iii*) adjust the preacquisition delay to remove the need for frequency-dependent phase corrections in F_2 (Section 3.3.2.3), (*iv*) digitally oversample in t_2 (*74*), and (*v*) set the initial sampling delay in t_1 to obtain either 0° or 180° first-order phase correction in F_1 (Section 3.4.1). More details on these topics can be found elsewhere in this book. Because the diagonal and cross-peaks in the TOCSY spectrum are predominantly in-phase and absorptive, the choice of $t_{1\max}$ is limited by the desired resolution in F_1. Sampling t_1 beyond $1.5/R_2$ to $2/R_2$ is unnecessary, and values of $t_{1\max}$ in the range of 40 to 60 ms are usually adequate.

Generally, isotropic mixing is used during a pulse sequence to achieve one of two goals: (*i*) efficient transfer of magnetization through a single three-bond scalar coupling only and (*ii*) maximum transfer of magnetization between resonances at extreme ends of a spin system. The former aim is required to identify all possible $^1H^N$–$^1H^\alpha$ correlations, or if the isotropic mixing is part of a longer pulse sequence (Sections 6.5.5 and 6.7). The latter objective intends to provide observable cross-peaks between all spins within a spin system and is critical for successful completion of the spin system assignment stage of the sequential assignment process (Section 9.1.1). Both of these aims cannot be achieved simultaneously with a single mixing time because of the oscillatory nature of the magnetization transfer process (*56*): as the mixing time is increased, cross-peaks between directly coupled spins tend to increase in intensity quickly and then decrease before cross-peaks to more distant protons have even started to gain intensity, as illustrated for an isoleucine spin system in Fig. 6.48. During the assignment process, several TOCSY spectra are commonly acquired with different mixing times to avoid the possibility of missing correlations that have a minimum in the transfer function at the mixing time used in a single experiment. During the mixing period, the supercycle comprising the mixing sequence must be executed an integral number of times. Given the rf field strengths commonly used in TOCSY experiments (10–12 kHz), the duration of a supercycle is 2–4 ms (depending on the sequence used). Therefore, the mixing time can only be varied in increments of this amount.

Simulations indicate that for residues with large $^3J_{H^NH^\alpha}$, transfer from $^1H^N$ to $^1H^\alpha$ will be maximal at 30–50 ms, whereas transfer from $^1H^N$ to other side chain protons increases approximately monotonically for mixing times up to 100 ms (*56*). In cases with smaller values of $^3J_{H^NH^\alpha}$, transfer from $^1H^N$ to all other protons is approximately

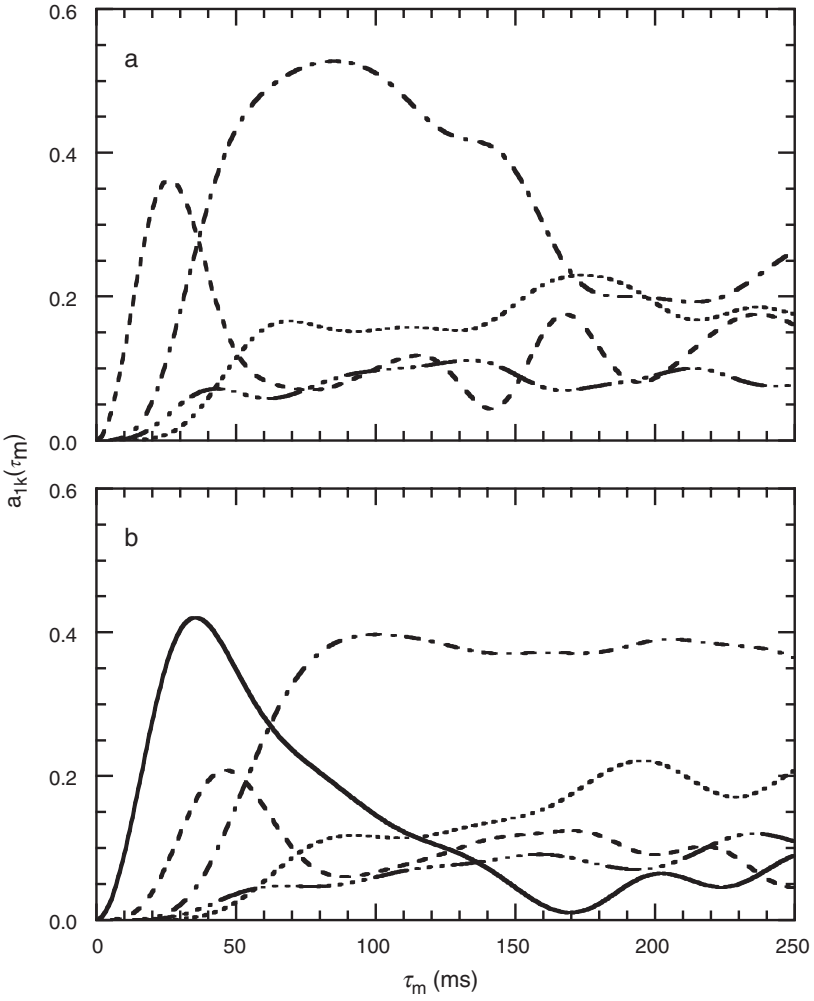

FIGURE 6.48 Variation of cross-peak intensity as a function of isotropic mixing time for an isoleucine spin system. (a) Cross-peak intensity for transfer from the $^1H^{\alpha}$ spin with the $^1H^N$ spin removed and (b) cross-peak intensity for magnetization transfer from the $^1H^N$ spin. The curves for the destination spins are (—) $^1H^{\alpha}$, (– – –) $^1H^{\beta}$, (–· · ·–) $H^{\gamma 1}$, (– · –) $^1H^{\gamma 2}$, and (· · · ·) $^1H^{\delta}$. The transfer functions were calculated using the following coupling constants: $^3J_{H^NH^{\alpha}} = 10.0$ Hz, $^3J_{H^{\alpha}H^{\beta}} = 12$ Hz, vicinal couplings to methyl groups were 6.7 Hz, all geminal couplings were 15 Hz, and all other vicinal couplings were 7 Hz. The effect of relaxation during the mixing was not considered.

monotonic up to 100 ms. Thus, maximizing transfer from $^1H^N$ to $^1H^\alpha$ will most likely be obtained with an isotropic mixing period 35–45 ms in duration. The simulations indicate that in order to maximize transfer to protons distant from $^1H^N$, longer mixing times should be employed. However, relaxation during the mixing sequence, which was not incorporated into the simulations, reduces the intensity of all cross-peaks at longer mixing times. For a protein the size of ubiquitin, the maximal useful length of isotropic mixing is of the order of 100 to 120 ms; for larger proteins, this limit is shorter. A usual course of action would be to acquire one TOCSY with a mixing time of 40–60 ms to obtain a high number of $^1H^N$–$^1H^\alpha$ correlations, and then to acquire a second TOCSY with as long a mixing time as possible (i.e., 75 ms or longer) without severe loss of signal intensity.

Although transfer through a single coupling is as efficient as in the COSY experiment (Sections 4.1.1.1 and 4.2.1.2), the peaks resulting from relay through several couplings are often of very low intensity. Thus, total acquisition times will generally be longer than for COSY. One or two passes through the phase cycle described in Fig. 6.45 or 6.46 (32 or 64 scans, respectively) will give acceptable sensitivity for a protein in the 1–4 mM range. Assuming a t_{1max} of 50 ms and a reasonable F_1 spectral width, TOCSY experiments require total acquisition times of 10–20 hr.

The spectra shown in Fig. 6.49 were acquired using the DIPSI-2rc sequence with a pulse field strength of ~12.5 kHz applied for 48, 83, or 102 ms. Thirty-two transients were collected for each of 576 t_1 increments, yielding a t_{1max} of 50 ms and total acquisition times of about 10.5 hr. Quadrature detection in F_1 was achieved with TPPI. The delays on either side of the isotropic mixing time only facilitated a change in transmitter power; z-filtration (*54*) was not performed.

6.5.3 PROCESSING

Appropriate window functions for TOCSY spectra are far less resolution enhancing than are those used for COSY-type spectra. Sine bells shifted by 60° to 90° in F_1 and F_2 provide some degree of resolution enhancement while reducing truncation effects. The trade-off between sensitivity and resolution can be fine tuned by varying the width of the sine bell from 80 to 300 ms in t_2. Alternatively, matched exponential apodization or weak (i.e., not very resolution enhancing) Lorentzian-to-Gaussian transformations can be performed. The Lorentzian-to-Gaussian transformations are beneficial when observing cross-peaks close to the diagonal; the intensity of the diagonal is such that the

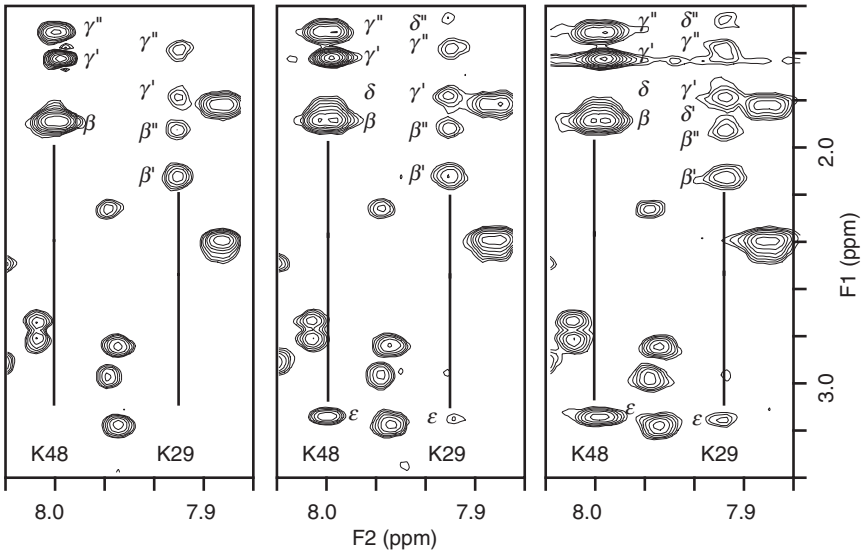

FIGURE 6.49 Sections of H_2O TOCSY spectra acquired with mixing times of 48 (left), 83 (center), and 102 ms (right). The cross-peaks observed to the amide protons of Lys29 and Lys48 are assigned at the different mixing times. Cross-peaks to the spin-system termini are observed only at the longer mixing times.

Lorentzian tails are very obtrusive. Commonly, spectra are processed with at least two different window functions to maximize sensitivity (for analyzing most of the spectrum) and enhance resolution (for analyzing heavily overlapped regions of the spectrum).

In addition to the precautions taken while setting up the experiment, other processing "tricks" (some of which are discussed in Chapter 3) can be beneficial in 2D spectra with absorptive lineshapes. In brief, these include (*i*) deconvolution to remove the residual water resonance in each FID (*75*), (*ii*) linear prediction of the first (or first few) points of the FID, and (*iii*) applying a baseline correction of a functional form sufficient to remove dc offsets or correct tilting, bowing, or rolling of the baseline. In most cases, if all other acquisition and processing precautions are taken, baseline corrections will not be needed.

The H_2O TOCSY spectra presented in this section were processed with weak Lorentzian-to-Gaussian transformations in t_1 and t_2. A cosine bell was also applied in t_1 to eliminate truncation artifacts. The solvent resonance was removed by deconvoluting the FID with a sine lineshape

averaged over 32 points. Any dc offset was removed by considering the intensity of the final 5% of each FID. The first point of each FID was linear predicted using the first 128 points (using the HSVD algorithm) and then scaled by 0.5 prior to Fourier transformation.

6.5.4 INFORMATION CONTENT

COSY-type experiments are very good at identifying sections of spin systems within the so-called fingerprint regions (Section 6.2.1.4). Connecting fragments from the different fingerprint regions is difficult in such spectra because of overlap and self-cancellation (due to complex fine structure) of the intervening methylene signals. TOCSY, and other relayed experiments discussed later, circumvent these problems by producing cross-peaks between the fingerprint resonances at opposite ends of extended spin systems. Because of the large chemical shift dispersion of the amide resonances, relayed connectivities involving these protons play a vital role in identification and assignment of spin system type (Section 9.1.1). Thus, in cases where two spin systems have identical $^1H^{\alpha}$ chemical shifts, the complete spin systems can be assigned by observing correlations to the associated $^1H^N$ spin.

In TOCSY spectra acquired from H_2O solution, the most useful cross-peaks include correlations from $^1H^N$ to the methyl resonances of alanine, threonine, valine, leucine, or isoleucine; the $^1H^{\delta}$ or $^1H^{\varepsilon}$ resonances of arginine or lysine residues, respectively; and the $^1H^{\beta}$ of three-spin side chains, or $^1H^{\beta}$ and $^1H^{\gamma}$ of five-spin side chains. Because of the length of leucine, isoleucine, arginine, and lysine side chains, the interesting end-to-end cross-peaks are only observed for longer mixing times. Some examples of the correlations observed in these long side-chains as the mixing time is increased are shown in Fig. 6.49. Commonly, not all of these correlations will be observed because small values of $^3J_{H^NH^{\alpha}}$ or small values for $^3J_{H^{\alpha}H^{\beta'}}$ and $^3J_{H^{\alpha}H^{\beta''}}$ will limit transfer from $^1H^N$ or $^1H^{\alpha}$. Provided some $^1H^{\alpha}$ resonances are resolved, TOCSY spectra acquired from D_2O solution permit observation of cross-peaks between $^1H^{\alpha}$ and the spin system termini.

Analysis of TOCSY spectra is prone to two possible pitfalls. First, even if all side chain resonances are observed, definitive assignment of a resonance to a particular position within the side chain may not be possible. This is particularly true for the methylene groups of five-spin side chains, arginine, and lysine. Estimates of the assignment from chemical shift arguments, or by following TOCSY cross-peak intensity as a function of mixing time, are not infallible. Other correlation techniques that transfer coherence over a specific number of couplings

are required to eliminate ambiguity (for example, see Fig. 6.42). Second, the variation of cross-peak intensity with mixing time, including initial growth and then decay, may prevent observation of cross-peaks at certain mixing times.

In the 48-ms mixing-time TOCSY experiment of ubiquitin, correlations between $^1H^N$ and the terminal protons of many shorter side chains are observed (i.e., transfer as far as $^1H^{\gamma}$). However, very few correlations are observed from $^1H^N$ to $^1H^{\varepsilon}$ of lysine or $^1H^{\delta}$ of leucine (zero out of seven lysine residues and four out of nine leucine residues); many more such correlations are observed at 84 ms (five out of seven lysine residues and all nine leucine residues). Extending the mixing period to 102 ms leads to the observation of weak $^1H^N$–$^1H^{\varepsilon}$ correlations for the two other lysine residues. For the seven isoleucine residues, cross-peaks from $^1H^N$ to both terminal methyl groups are readily apparent after 48 or 84 ms of isotropic mixing. In two cases, the correlations from $^1H^N$ to the intervening $H^{\gamma 1}$ are only observed at 102 ms, and in a third case one of the $^1H^N$–$^1H^{\gamma 1}$ cross-peaks was not observed at all.

6.5.5 Experimental Variants

The use of isotropic mixing has become a mainstay of ^1H NMR analysis of proteins. Four less common applications involving isotropic mixing are discussed in this section: pre-TOCSY experiments, TOCSY with very short acquisition times, sensitivity-enhanced TOCSY, and TOCSY with short mixing times.

The concept of using isotropic mixing prior to a pulse sequence has already been encountered in the pre-TOCSY COSY experiment (Section 6.2.1.6). The idea behind this and all pre-TOCSY experiments is to use a short TOCSY mixing period to transfer magnetization to protons that have been attenuated by the solvent presaturation pulse (*17*). Thus, cross-peaks can be observed at the F_1 frequency of the water resonance. The process is potentially applicable to all homonuclear 2D experiments utilizing solvent presaturation, but is most commonly used in the COSY experiment. The introduction of the isotropic mixing period alters all cross-peak intensities in the final spectrum. This is particularly pertinent for NOESY spectra because cross-peak intensities are interpreted in a quantitative fashion to generate distance restraints for protein structure calculations. In scalar correlation spectra, peak positions, and not intensities, are generally of interest, and perturbations from the pre-TOCSY sequence are unimportant.

Investigations of amide proton exchange with solvent play an important role in understanding protein structure and internal dynamics

(*76*). Exchange rates can be obtained by rapidly transferring protein from H_2O to D_2O and repeatedly acquiring NMR spectra to follow the decay of amide ^{1}H signal as protons exchange with solvent deuterons. One-dimensional NMR spectra permit high temporal resolution (of the order of a few minutes); however, overlap of the $^1H^N$ resonances precludes detailed, site-specific analyses of the exchange rates. Two-dimensional spectra permit the cross-peaks from individual amide protons to be resolved; however, each spectrum must be acquired quickly (on the order of 30 min or less) and have a high sensitivity for amide protons. TOCSY spectra provide a useful compromise between these two factors [HSQC spectra (Section 7.1.1.1) of ^{15}N-labeled proteins are even more useful]. A short t_{1max} (and short total acquisition time) can be used because cross-peaks in TOCSY spectra have in-phase absorptive lineshapes. The mixing time is kept short (no more than 40 ms) to maximize the intensity of $^1H^N$–$^1H^\alpha$ correlations, and the F_1 resolution is maximized by reducing the spectral width in F_1 to cover the $^1H^N$–$^1H^\alpha$ fingerprint region only (care should be taken to avoid folding or aliasing diagonal peaks into the region of interest). Finally, total acquisition times are kept short by only performing 4 or 8 transients per increment. Bax and colleagues have discussed some of the experimental aspects of short 2D experiments (*77*). Figure 6.50 shows a section of a TOCSY spectrum acquired from a 2 m*M* H_2O sample of ubiquitin in 15 min. The data consisted of four transients co-added for each of 160 t_1 experiments. The pulse sequence used was the gradient-enhanced TOCSY experiment of Fig. 6.46. The optimum four-step phase cycle (see legend, Fig. 6.50) was deduced empirically to determine which artifacts were dominant (and therefore required attenuation by the limited phase cycle) on the NMR spectrometer utilized. Although the acquisition time was short, most of the $^1H^N$–$^1H^\alpha$ correlations are visible.

In the version of the TOCSY experiment just described, after the initial 90°_x–t_1–90°_x period, a mixture of frequency-labeled I_{1z} and I_{1x} magnetization is created [6.1]. If an isotropic mixing sequence is applied orthogonally (i.e., all pulses in the sequence have phases y or $-y$), then magnetization transfer occurs independently by the pathways $I_{1z} \rightarrow I_{kz}$ [4.16] and $I_{1x} \rightarrow I_{kx}$ [4.22]. Thus, the TOCSY experiment is unusual in that equivalent coherence transfer is obtained simultaneously along two orthogonal axes. In the conventional experiment, phase cycling (*54*, *57*) or rf inhomogeneity effects (*52*, *53*) are used to remove one or other of the components and obtain amplitude-modulated phase-sensitive data. In Fig. 6.45, inversion of the phases ϕ_1 and ϕ_2 every second transient suppresses the signal from the $I_{1x} \rightarrow I_{kx}$ pathway. Cavanagh and Rance

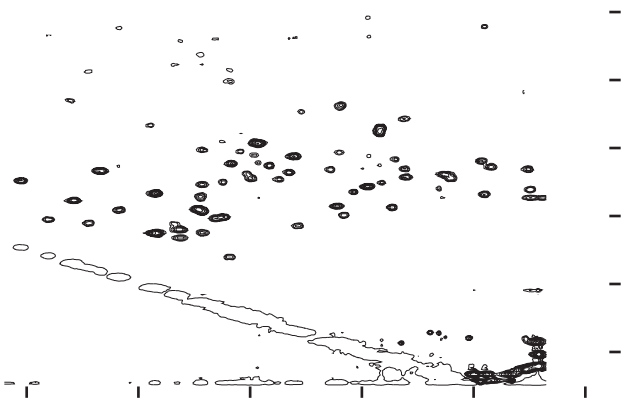

have shown that an improvement in signal-to-noise ratio of $\sqrt{2}$ is obtained by altering the phase cycle to retain both components entering the isotropic mixing period (*78*). Absorptive lineshapes are achieved by recording two independent data sets in which the phase of the 90° pulse prior to the mixing period differs by 180°. For example, in Fig. 6.45, the first two steps of the phase cycle ($\phi_1 = x, -x$; $\phi_2 = x, x$) are stored as one data set and the second two steps of the phase cycle ($\phi_1 = x, -x$; $\phi_2 = -x, -x$) are stored as a second data set. Addition of the two spectra retains the resonances arising from longitudinal magnetization at the start of the mixing period (an effect identical to that obtained by the phase cycling for the conventional experiment). Subtraction of the two spectra retains the resonances arising from transverse magnetization at the beginning of the mixing period. After processing, the resonance peaks in the two spectra are identical, but the noise is uncorrelated; therefore, addition produces a spectrum with a $\sqrt{2}$ gain in sensitivity

over a conventional spectrum acquired with the same total acquisition time (*78*). Similar principles have been used in several heteronuclear pulse schemes to improve sensitivity (Section 7.1.3.2).

Because the rate of buildup of a TOCSY peak depends on the size of the scalar coupling constant, quantitative analysis of cross-peak intensities can be used to estimate coupling constants (*79*). The size of a TOCSY cross-peak depends on all of the couplings within a spin system; therefore, extraction of single coupling constants must be performed with a degree of caution. Short mixing times (5–20 ms) must be used to ensure that magnetization transfers primarily through a single scalar coupling interaction; however, zero-quantum artifacts (see Section 6.6.1.1) can distort cross-peaks in such spectra. The rather crude estimates of scalar coupling constants obtained by this approach can be used to aid in the stereospecific assignments of β-methylene protons (*80*).

6.6 Cross-Relaxation NMR Experiments

All of the experiments described so far in this chapter have relied upon magnetization or coherence transfer via scalar couplings and only provide correlations between protons within the same amino acid residue. The sequential assignment process in an unlabeled protein sample is completed using the dipole–dipole cross-relaxation to correlate ^{1}H spins that are close in space. Additionally, distance restraints for structure determination of proteins are derived primarily from ^{1}H–^{1}H dipole–dipole cross-relaxation. The two experimental approaches in existence are based on longitudinal cross-relaxation (the NOE) and transverse cross-relaxation (the ROE). Theoretical origins of these cross-relaxation mechanisms are described in Section 5.5.

6.6.1 NOESY

The pulse sequence for the NOESY (Nuclear Overhauser Effect Spectroscopy) experiment is shown in Fig. 6.51. Initially, a 90°–t_1–90° element is used to frequency label the spins and return the magnetization to the z-axis. Magnetization transfer occurs via dipolar coupling for a period τ_m before observable transverse magnetization is created by the final 90° pulse. The final pulse can be replaced by a Hahn echo sequence with a concomitant improvement in the flatness of the baseline (Sections 3.6.4.2 and 6.5). A coherence level diagram for this pulse sequence is presented in Fig. 6.51. If a probe equipped with

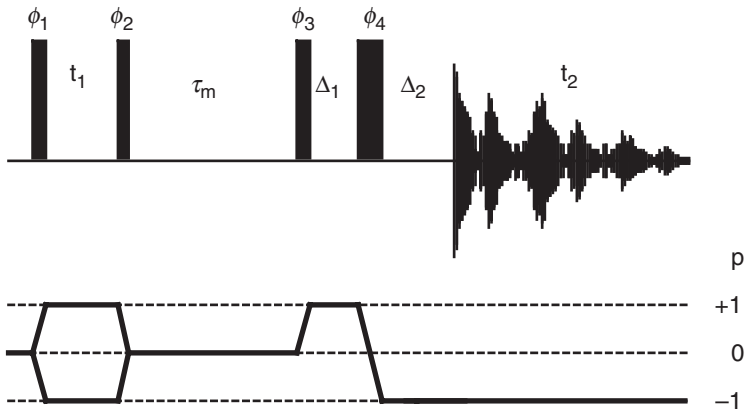

FIGURE 6.51 Pulse sequence and coherence level diagram for the NOESY experiment. A Hahn echo sequence is included prior to detection. Appropriate values for the delays are discussed in the text. The same 32-step phase cycle as for the TOCSY is employed (Fig. 6.45).

pulsed field gradients is available, then pulsed field gradients can be used for artifact and solvent suppression. The pulse sequence, coherence level diagram, and phase cycle for an experiment that incorporates the excitation-sculpting water-suppression technique is shown in Fig. 6.52.

6.6.1.1 Product Operator Analysis The theory of magnetization transfer by dipolar coupling (the NOE) has been discussed in Sections 4.2.2 and 5.5. For a spin system containing two scalar-coupled spins, evolution through the 90°_x–t_1–90°_x sequence is described by [6.1]. Evolution of the I_{1z} term in [6.1] during τ_m is governed by the Solomon equations, in which the initial condition is $-I_{1z}\cos(\Omega_1 t_1)\cos(\pi J_{12} t_1)$ and the equilibrium magnetization, I^0_{1z}, is rejected by phase cycling for axial peak suppression. If $K-1$ spins (I_k for $k=2,\ldots,K$) are close in space to spin I_1 (this notation allows for the possibility that the scalar-coupled spin, I_2, is dipolar coupled to I_1 as well), then the resulting evolution during τ_m is

$$-I_{1z}\cos(\Omega_I t_1)\cos(\pi J t_1) \xrightarrow{\tau_m} -\sum_{k=1}^{K} I_{kz} a_{1k}(\tau_m)\cos(\Omega_1 t_1)\cos(\pi J_{12} t_1), \qquad [6.48]$$

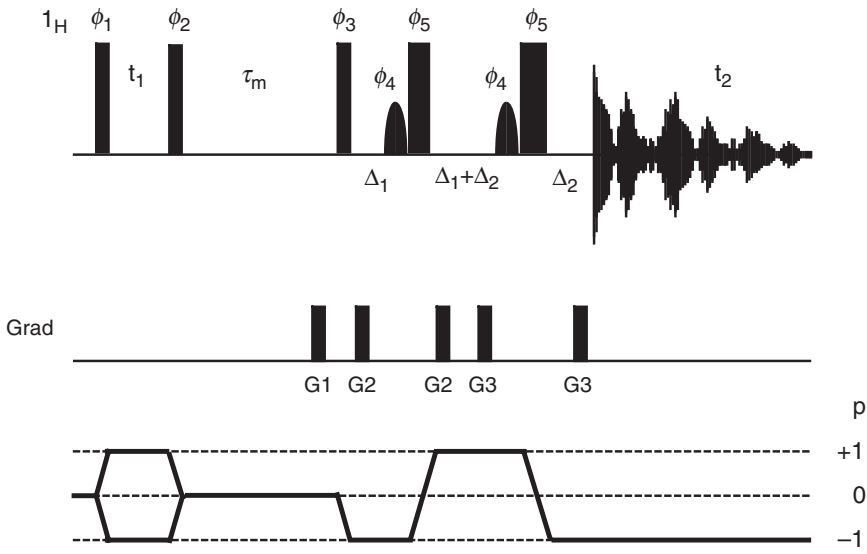

FIGURE 6.52 Pulse sequence and coherence level diagram for the NOESY experiment using excitation sculpting to avoid presaturation of the solvent resonance. The curved pulse shapes indicate selective 180° pulses at the water frequency. Appropriate values for the delays are discussed in the text. The same 32-step phase cycle as for the TOCSY is employed (Fig. 6.46). Frequency discrimination in F_1 is obtained by shifting the phase of ϕ_1 and the receiver according to the TPPI, States, or TPPI–States protocols (Section 4.3.4). A bipolar pair of gradients can be inserted into the t_1 and τ_m periods to prevent radiation damping (*31*).

in which $a_{1k}(\tau_m) = [\exp(-\mathbf{R}\tau_m)]_{1k}$ is the (1, k)th element of the matrix exponential and $\mathbf{R}$ is the matrix of rate constants ρ_i and σ_{ij} (Section 5.1.2). After the final 90° pulse and Hahn echo, the density operator terms that result from the longitudinal magnetization are given by

$$\sum_{k=1}^{K} I_{ky} a_{1k}(\tau_m) \cos(\Omega_1 t_1) \cos(\pi J_{12} t_1). \qquad [6.49]$$

The final spectrum contains diagonal peaks (the $k = 1$ term in [6.49]) and $I_1 \rightarrow I_k$, for $k > 1$, NOE cross-peaks. All of the peaks are in-phase with respect to homonuclear scalar coupling in F_1 and F_2, and also can be phased to absorption in both dimensions.

The magnetization that will give rise to the NOE cross-peaks stems from longitudinal magnetization (coherence level $p = 0$) during τ_m, and the phase cycling rejects other coherence levels during this period, including the single-spin terms I_{1x} and $2I_{1x}I_{2z}$ in [6.1]. The second term of [6.1] is a mixture of ZQ_y^{12} ($p = 0$) and DQ_y^{12} ($p = 2$) coherences (Section 2.7.5); while the double-quantum operator is suppressed by the phase cycling, the zero-quantum term survives. During τ_m the zero-quantum term will precess according to the difference in chemical shift of I_1 and I_2. The following terms will be generated by the final 90° pulse:

$$\begin{aligned} -ZQ_y^{12} \cos(\Omega_1 t_1) \sin(\pi J_{12} t_1) \\ \xrightarrow{\tau_m - \left(\frac{\pi}{2}\right)_x} +\tfrac{1}{2}[2I_{1x}I_{2x} + 2I_{1z}I_{2z}] \cos(\Omega_1 t_1) \sin(\pi J_{12} t_1) \sin[(\Omega_1 - \Omega_2)\tau_m] \\ -\tfrac{1}{2}[2I_{1z}I_{2x} - 2I_{1x}I_{2z}] \cos(\Omega_1 t_1) \sin(\pi J_{12} t_1) \cos[(\Omega_1 - \Omega_2)\tau_m]. \end{aligned} \quad [6.50]$$

The last line of [6.50] contains observable terms and therefore must be considered in an analysis of the NOESY spectrum. Such artifacts arise via a zero-quantum pathway and are referred to as *zero-quantum* peaks. These peaks are in antiphase in both dimensions, and are also in dispersion when the normal NOE peaks ([6.49]) are phased to absorption.

During analysis of a NOESY spectrum, the integrated intensity of a given cross-peak is interpreted in terms of the distance between the two protons giving rise to the peak (Sections 6.2.5.4 and 10.2.1). Clearly, from [6.50] the real NOE and zero-quantum peaks between two coupled spins appear at identical chemical shifts in F_1 and F_2. Although the net integrated intensity of the dispersive zero-quantum component is zero, accurately integrating the contributions from the dispersive tails of this component may not be possible, and errors in the measurement of the NOE cross-peak volume result; in addition, the antiphase dispersive tails can interfere with the integration of other cross-peaks in crowded regions of the spectrum. The magnitude of the zero-quantum component varies as $\cos[(\Omega_1 - \Omega_2)\tau_m]$, which depends on the chemical shifts of the spins involved and the mixing time. In addition, because the zero-quantum terms have transverse components during τ_m, relaxation is faster than for longitudinal magnetization, and the zero-quantum component is reduced in intensity relative to the true NOE peak when a long mixing time is

employed. The use of a *z*-filter to suppress the zero-quantum terms is discussed in Section 6.6.1.2.

6.6.1.2 Experimental Protocol The peaks of interest in the NOESY spectrum are absorptive and in-phase in both dimensions ([6.49]). Thus, all of the precautions adopted in Section 6.5.2 to ensure flat baselines in TOCSY spectra should also be employed in the NOESY experiment. Obtaining a flat baseline is even more imperative in the NOESY spectrum; at the least, the size of the cross-peaks will be interpreted in a semiquantitative fashion, hence any offset in the baseline will lead to systematic errors in the NOE cross-peak volume. The number of observable NOEs will have a direct bearing on the quality of structures produced from the data, hence obtaining a high S/N ratio is also important. Acquisition times of 24 to 48 hr are not uncommon, even with relatively concentrated samples.

Accurate quantitative analysis also requires minimization of any other effect that may systematically alter the intensity of peaks, especially when a detailed quantitative analysis is to be performed (e.g., see Sections 6.6.1.4 and 10.2). The recycle delay should be $3/R_1$, in which R_1 is the smallest longitudinal relaxation rate in the protein, to avoid steady-state effects that perturb the intensity of cross-peaks. Also, solvent presaturation should be avoided as a means of solvent suppression in these applications because the intensity of cross-peaks involving protons that resonate close to the water, or labile protons that are exchanging with the solvent, will be reduced. Methods that attempt to combat these effects are discussed in Section 6.6.1.5.

The theoretical time dependence of the NOE cross-peaks in the NOESY experiment (Section 5.1.2) suggests that the mixing time should be on the order of $1/R_1$ to maximize the intensities of NOE cross-peaks. A long mixing time also has the advantage that zero-quantum artifacts will be of low intensity. However, long mixing times will also allow multiple magnetization transfers, or *spin diffusion*, to contribute substantially to the cross-peak intensity. The origins and consequences of spin diffusion are illustrated for a three-spin system with the following relaxation rate matrix:

$$\mathbf{R} = \begin{bmatrix} \rho_1 & \sigma_{12} & 0 \\ \sigma_{12} & \rho_2 & \sigma_{23} \\ 0 & \sigma_{23} & \rho_3 \end{bmatrix}. \qquad [6.51]$$

By construction, spins I_1 and I_3 are too far apart to have an appreciable dipolar coupling ($\sigma_{13} = 0$), thus direct magnetization transfer between I_1

and I_3 is not possible. The time dependence of the I_1 magnetization is given to third-order in time by

$$\begin{aligned}\langle I_{1z}\rangle(\tau_m) &= \sum_{k=1}^{3}[\exp(-\mathbf{R}\tau_m)]_{1k}\langle I_{kz}\rangle(0)\\ &\approx \sum_{k=1}^{3}\left[E_{1k} - R_{1k}\tau_m + \tfrac{1}{2}R_{1k}^2\tau_m^2 - \tfrac{1}{6}R_{1k}^3\tau_m^3\right]\langle I_{kz}\rangle(0)\\ &= \langle I_{1z}\rangle(0)\left\{1 - \rho_1\tau_m + \tfrac{1}{2}\left(\rho_1^2 + \sigma_{12}^2\right)\tau_m^2 - \tfrac{1}{6}\left(\rho_1^3 + 2\rho_1\sigma_{12}^2 + \rho_2\sigma_{12}^2\right)\tau_m^3\right\}\\ &\quad + \langle I_{2z}\rangle(0)\left\{-\sigma_{12}\tau_m + \tfrac{1}{2}(\rho_1 + \rho_2)\sigma_{12}\tau_m^2\right.\\ &\quad \left.-\tfrac{1}{6}\left[\left(\rho_1^2 + \sigma_{12}^2\right)\sigma_{12} + (\rho_1 + \rho_2)\rho_2\sigma_{12} + \sigma_{12}\sigma_{23}^2\right]\tau_m^3\right\}\\ &\quad + \langle I_{3z}\rangle(0)\left\{\tfrac{1}{2}\sigma_{12}\sigma_{23}\tau_m^2 - \tfrac{1}{6}(\rho_1 + \rho_2 + \rho_3)\sigma_{12}\sigma_{23}\tau_m^3\right\}.\end{aligned} \quad [6.52]$$

Each of the terms in [6.52] can be assigned a physical interpretation; however, only three terms will be discussed in detail. The first-order term $-\sigma_{12}\tau_m\langle I_{2z}\rangle(0)$ represents direct transfer of magnetization from spin I_2 to spin I_1 and gives rise to a cross-peak in the NOESY spectrum. In the initial rate regime, only this term contributes to the cross-peak intensity, and the cross-peak intensity is proportional to the cross-relaxation rate constant, σ_{12}. The second-order term $(1/2)\sigma_{12}\sigma_{23}\tau_m^2\langle I_{3z}\rangle(0)$ exemplifies spin diffusion. This term gives rise to a cross-peak between spins I_1 and I_3 by an indirect two-step transfer from $I_3 \rightarrow I_2 \rightarrow I_1$. In the quadratic time regime, the intensity of the spin diffusion cross-peak depends on the product of the individual cross-relaxation rate constants. Finally, the third-order term $\rho_2\sigma_{12}^2\tau_m^3\langle I_{1z}\rangle(0)$ represents a back transfer pathway $I_1 \rightarrow I_2 \rightarrow I_1$. The back transfer has the effect of reducing the intensity of the cross-peak that would otherwise result from cross-relaxation between I_1 and I_2. Therefore, even for a two-spin system, outside of the initial rate regime, NOE cross-peak intensities are not proportional to the cross-relaxation rate constants. The assumed linearity between the NOE cross-peak intensities and cross-relaxation rate constants sometimes is called "the isolated two-spin approximation"; as the present discussion shows, this phrase is a misnomer.

As a consequence of spin diffusion, cross-peaks between pairs of protons that are far apart will gain intensity from magnetization that has been transferred via intervening spins, while cross-peak between pairs of protons that are close together will be decreased by the loss of magnetization to other nearby protons. Failure to adequately account for spin diffusion results in the derivation of inaccurate distance

constraints between pairs of protons; overly tight constraints derived from NOE cross-peaks dominated by spin diffusion lead to overly constrained and incorrect protein structures (Sections 6.6.1.4 and 10.2.1). Spin diffusion effects can be minimized by using a short mixing time, but in these experiments all cross-peak intensities will be low, and zero-quantum artifacts will be emphasized. A compromise is usually struck, with mixing times of 50–150 ms providing reasonable cross-peak intensities that are not overly influenced by spin diffusion or zero-quantum contributions. Dipolar relaxation is more efficient in systems with long rotational correlation times, hence a shorter mixing time is required to limit spin diffusion in large proteins.

The dispersive antiphase components observed in NOE cross-peaks between scalar-coupled protons can be suppressed by several methods. Early strategies involved randomly changing the phase of the zero-quantum coherence by randomly varying the mixing time or by applying a 180° pulse at random positions within a fixed mixing time from one t_1 increment to the next (*81*). A disadvantage of these methods is that they effectively transfer the problem of zero-quantum coherence into additional t_1 noise in the NOESY spectra. More effective procedures have been proposed for the elimination of zero-quantum coherences. For example, the mixing time can be kept fixed, and a 180° pulse applied at a selected position within the mixing period; this pulse causes a partial refocusing of the zero-quantum coherence. By co-adding several data sets with the 180° pulse varied in its position, suppression of zero-quantum coherence can be achieved (*82*, *83*). More recently, a new method has been developed that involves the simultaneous application of a swept-frequency 180° pulse and a magnetic field gradient (*84*, *85*). In this scheme, the presence of the magnetic field gradient causes the ^{1}H spins at different positions in the sample to be inverted at different time points; this leads to a position-dependent variation in refocusing of the zero-quantum coherence. Integrated over the sample volume, the variable refocusing will lead to destructive interference of the zero-quantum coherences and will therefore provide an effective level of suppression. An alternative scheme for dealing with zero-quantum coherences has also been proposed that separates such zero-quantum peaks from the NOESY peaks, rather than attempting to suppress the zero-quantum resonances. In this procedure, a 2D NOESY experiment is run instead as a 3D experiment in which the second evolution period is created by incrementing the position of a 180° pulse in the NOE mixing period (*86*). In this case, the NOE peaks will appear in the zero frequency plane in the second dimension, whereas the zero-quantum peaks will appear in planes at the appropriate zero-quantum frequencies. In all of

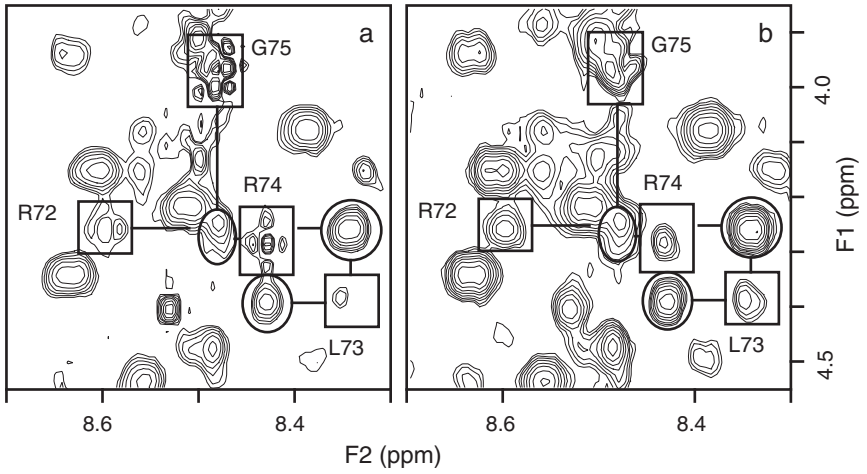

FIGURE 6.53 Comparison of sections of the (a) $\tau_m = 40$ and (b) $\tau_m = 100$ ms NOESY spectra of ubiquitin in H_2O solution. Several intraresidue and sequential $^1H^N$–$^1H^\alpha$ cross-peaks are denoted by the rectangles and ellipses, respectively, and allow sequential assignment of several residues near the C-terminus. Due to the presence of zero-quantum artifacts, several of the intraresidue peaks contain dispersive antiphase components in the 40-ms mixing time experiment.

these suppression schemes, elimination of zero-quantum coherence arising from spins closely spaced in resonance frequency is difficult.

The phase cycling used in the NOESY experiment must incorporate axial peak-suppression phase cycling (of the first 90° pulse) and selection of $\Delta p = -1$ and $\Delta p = +1$ by phase cycling of the second 90° pulse. The basic phase cycle is four steps ($\phi_1 = x, -x, -x, x$; $\phi_2 = x, x, -x, -x$; and receiver $= x, -x, x, -x$). Alternatively, both pulses can be phase cycled in synchrony to select $\Delta p = 0$ (Section 4.3.2.2). EXORCYCLE phase cycling is used for the Hahn echo and CYCLOPS is applied to all pulses. Bodenhausen and co-workers have discussed phase cycles for NOESY experiments (*87*).

The NOESY spectra depicted in Fig. 6.53 were acquired from H_2O solution using the Hahn echo sequence of Fig. 6.51 with the sample delay set to avoid phase correction-associated baseline distortions in F_1 (Section 3.3.2.3). The solvent was saturated during the recycle delay and during the mixing time. Thirty-two transients were collected for each of 576 increments of t_1 ($t_{1max} = 50$ ms), a mixing time of 40 or 100 ms was

used, and total acquisition time was 10.0 or 10.5 hr. No attempt was made to suppress zero-quantum contributions.

6.6.1.3 Processing The similarity of TOCSY and NOESY lineshapes dictates that processing of these two spectra is similar. All of the details discussed in Section 6.2.4.3 are relevant to the present discussion. Accurate determination of cross-peak volumes is important for quantitative analysis of NOESY spectra. A variety of methods have been proposed to improve the quality of cross-peak volume extraction from NOESY spectra (*88–91*).

The ubiquitin spectra shown in Fig. 6.53 were processed in a fashion identical to that for the TOCSY spectra of Section 6.5.3.3, except that deconvolution of the residual water resonance was not necessary.

6.6.1.4 Information Content NOESY spectra provide a powerful means of elucidating conformational details of molecules in solution. The requirement that two protons be separated by less than 5 Å (or so) in order to give rise to an NOE immediately allows a loose restraint to be placed on their separation. Furthermore, the size of the NOE depends inversely on the distance, hence the restraint can be tighter than 5 Å if the NOE is intense. In order to calculate the structure of a protein, many such restraints must be identified in an unambiguous fashion (Section 9.2.1). In most applications, NOE cross-peaks simply are placed into one of several size categories associated with an upper bound for the proton separation. More accurate calibration is difficult because of the complex relationship between NOE buildup, local correlation time, and the distribution of neighboring protons. Analysis of NOESY spectra with different mixing times (called a buildup or τ_m series) allows the initial slope of the NOE buildup to be estimated and facilitates calibration. Methods for interpreting NOESY spectra are discussed in more detail in Section 10.2.1.

Figure 6.53 shows regions of the 40- and 100-ms NOESY spectra of ubiquitin in H_2O solution, and demonstrates that sequential $^1H^{\alpha}$–$^1H^N$ NOEs can be used to obtain sequence-specific assignments of the residues near the C-terminus. As expected for a protein of this size, the cross-peaks are all more intense at the longer mixing time. The residues at the C-terminus are conformationally mobile, have narrower linewidths, and therefore have very prominent dispersive contributions in the shorter mixing-time spectrum (Section 6.6.1.1); self-cancellation reduces the impact of these components for other, broader resonances. Increasing the mixing time also leads to a decrease in the relative intensity of zero-quantum effects.

Besides cross-relaxation, chemical exchange can also lead to cross-peaks in NOESY spectra. In cases of slow exchange between two species (Section 5.6), a cross-peak is observed at the frequencies of a particular nucleus in the two different sites if the exchange rate between the species is comparable to $1/\tau_m$. For proteins, the chemical exchange peaks will be of the same sign as NOE cross-peaks (the same sign as the diagonal peaks, formally negative), hence discrimination of the two can be difficult. Very complicated spectra can result due to peaks arising from combinations of exchange and cross-relaxation; in effect, these are spin diffusion-type peaks, as they involve two transfer steps. Identification of exchange effects is discussed in more detail in Section 6.6.2.4.

6.6.1.5 Experimental Variants Suppressing the solvent resonance by presaturation unavoidably results in transfer of saturation to labile protons undergoing exchange with solvent, and attenuation of cross-peaks involving protons that resonate close to the solvent resonance (Section 3.5.1). Several alternatives to presaturation in 1D ^{1}H NMR have already been discussed (Section 3.5) and these methods are valuable for NOESY experiments. The final pulse of the NOESY experiment rotates longitudinal magnetization into the transverse plane much the same as in a 1D experiment; hence, this *read pulse* can be replaced with a sequence used for 1D selective excitation.

The simplest method of acquiring NOESY spectra in H_2O solution without presaturation employs a jump-and-return observe sequence in place of the final 90° pulse (Section 3.5.2) (*92*). This experiment is usually referred to as a jump–return NOESY (JR.NOESY), and a pulse sequence is depicted in Fig. 6.54. Note that a Hahn echo cannot be incorporated into this experiment. Experimental protocol for the JR.NOESY is similar to a NOESY experiment acquired with presaturation. A variety of more complicated schemes can also be incorporated into the NOESY experiment with some advantages over the jump–return version (*93*, *94*).

The F_1 phase discrimination in the experiment depicted in Fig. 6.54 will result in longitudinal water magnetization during τ_m for some FIDs and in transverse water magnetization during τ_m for other FIDs, depending on the relative phase of ϕ_1 and ϕ_2 (this is true for both the TPPI and hypercomplex methods; Section 4.3.4). As a consequence, the water resonance will be suppressed to different degrees for the different FIDs, unless τ_m is sufficiently long to allow radiation damping of the water resonance back to the z-axis (relaxation is far too slow to be useful in this regard). The difference between the state of the water magnetization for different FIDs can be reduced somewhat by shifting

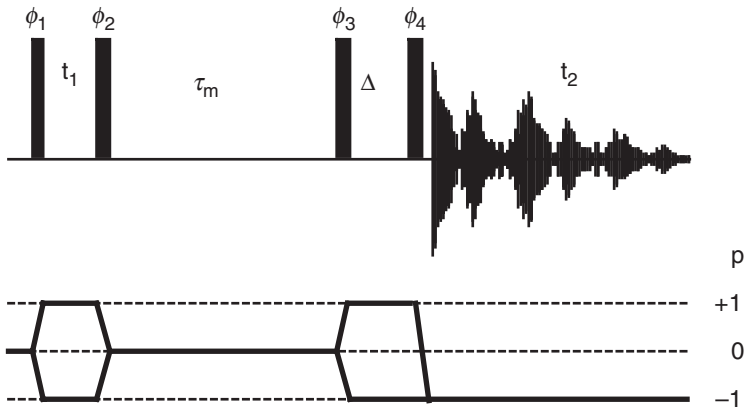

FIGURE 6.54 Pulse sequence and coherence level diagram for the NOESY experiment with a jump–return observe pulse (JR.NOESY). The basic eight-step phase cycle is as follows: $\phi_1 = x, -x, y, -y, -x, x, -y, y$; $\phi_2 = x, x, y, y, -x, -x, -y, -y$; $\phi_3 = 8(x)$; $\phi_4 = 8(-x)$; and receiver $= 4(x, -x)$. Cyclops is performed on all pulses and the receiver to yield a 32-step cycle. Adjusting the rotation angle and phase of pulse ϕ_4 a few degrees can improve the degree of solvent suppression. Frequency discrimination in F_1 is obtained by shifting the phase of ϕ_1 and the receiver according to the TPPI, States, or TPPI–States protocols (Section 4.3.4).

the phase ϕ_1 by 45°. If large values of τ_m are used to allow efficient radiation damping, then JR.NOESY spectra may include contributions from spin diffusion.

The JR.NOESY spectrum depicted in Fig. 6.55 was acquired from H_2O solution, with 32 transients for each of 576 t_1 increments ($t_{1max} = 50$ ms). A mixing time of 150 ms was used, and the total acquisition time was 11 hr. Sections of the JR.NOESY and NOESY with presaturation are depicted in Fig. 6.55. Many cross-peaks close to the water resonance are observed only in the JR.NOESY spectrum and other peaks up to 0.2 ppm. from the water line are noticeably more intense in the jump–return experiment (even allowing for the longer mixing time of this experiment). In Fig. 6.55 (and elsewhere in this spectrum), a large number of peaks occur at the exact F_1 frequency of the water resonance. These peaks can arise from a variety of mechanisms other than cross-relaxation with nonlabile protein protons coincident with the solvent resonance, including chemical exchange between water and labile $^1H^N$ or ^1HO groups, NOEs from bound water to protein

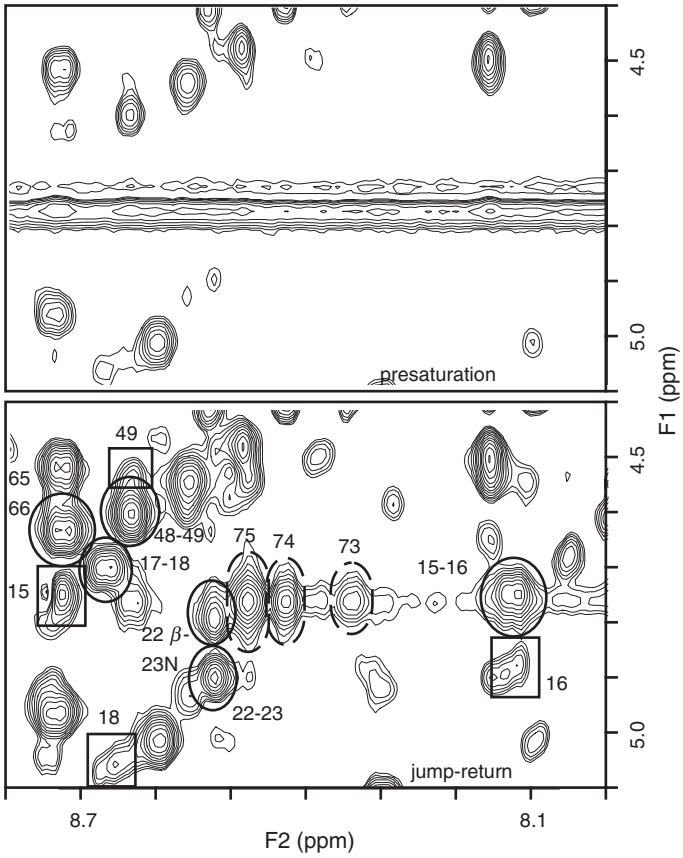

Figure 6.55 Comparison of NOESY spectra acquired from H_2O solution in which solvent was suppressed by presaturation (top) or selective excitation with a jump–return sequence (bottom). The spectra were collected under identical conditions except for the mixing times, which were 100 and 150 ms in presaturation and jump–return spectra, respectively. Intraresidue and sequential NOEs are denoted by rectangles and ellipses, respectively, with the peaks arising between $^1H^N$ and $^1H^\alpha$ unless otherwise noted. The three peaks outlined by broken ellipses probably arise from exchange of amide protons with the solvent, as residues 73 to 75 are close to the C-terminus and are flexible.

protons, or NOEs from protein hydroxyl protons on resonance with the water resonance.

Modified NOESY sequences using pulsed field gradients to help suppress the water have been described (*95*). As for the TOCSY

experiment, presaturation of the solvent resonance is avoided if the Hahn echo sequence element in Fig. 6.51 is replaced by a gradient water-suppression technique, such as the excitation-sculpting sequence element shown in Fig. 6.52. In contrast to the jump–return pulse sequence of Fig. 6.54, which returns the water magnetization to the $+z$-axis prior to detection, the excitation-sculpting approach dephases the water magnetization prior to detection. Thus, depending on the recycle delay and sample pH, some saturation transfer from water ^{1}H spins to the amide $^1H^N$ spins can occur, although at a reduced level compared to the NOESY experiment using presaturation (Fig. 6.51). As for the JR.NOESY, the difference between the state of the water magnetization during τ_m for different FIDs can be reduced by shifting the phase ϕ_1 by 45°. Gradient pairs applied during the t_1 period and during τ_m minimize radiation damping and reduce perturbations of signals close to resonance with the water signal (Section 6.3) (*31*). A section of the NOESY spectrum acquired using the pulse sequence of Fig. 6.52 is shown in Fig. 6.56. The region shown is identical to that shown in Fig. 6.55 and shows similar improvements as obtained using the jump–return experiment relative to the spectrum acquired using presaturation.

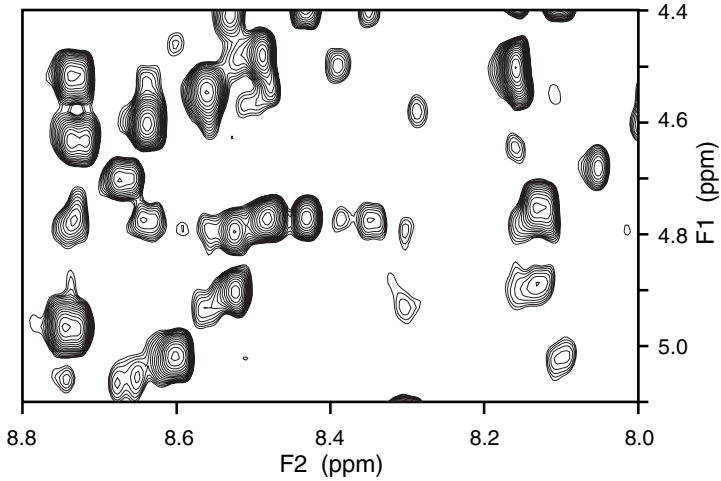

FIGURE 6.56 NOESY spectra acquired from H_2O solution in which solvent was suppressed by the excitation-sculpting approach of Fig. 6.52. The spectra were collected under the same conditions as for Fig. 6.55 (bottom) and the same region of the spectrum is shown.

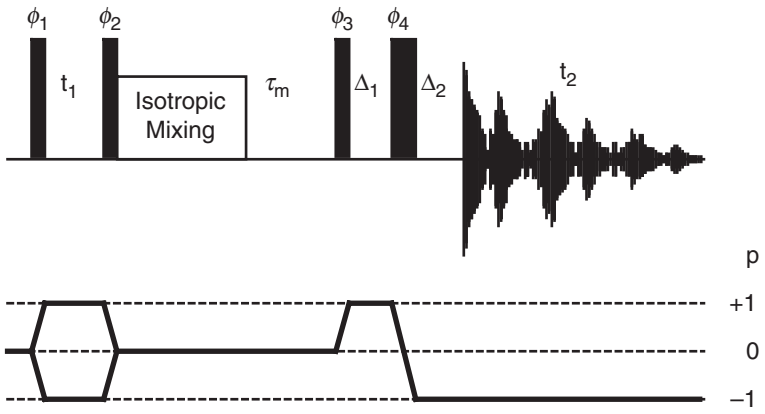

FIGURE 6.57 Pulse sequence and coherence level diagram for the relayed NOESY experiment. The phase cycle is identical to that used in Figs. 6.51 and 6.45.

In another variant of the basic NOESY experiment, the mixing period includes both isotropic mixing and cross-relaxation periods (Fig. 6.57), and is known as a relayed NOESY. Experimental setup is identical to that for a normal NOESY experiment. The aim is to use the isotropic mixing to transfer magnetization via a single scalar coupling, usually between $^1H^N$ and $^1H^\alpha$, prior to NOESY cross-relaxation. The isotropic mixing period normally is 20–30 ms in duration (Section 6.5.2). The choice of NOESY mixing time is based on a trade-off between cross-peak intensity and contributions from spin diffusion (Section 6.6.1.2). The experiment discussed in the following analysis was acquired with 32 transients for each of 576 t_1 increments (total acquisition time 10.5 hr); 27 ms of DIPSI-2rc isotropic mixing (*70*) was used prior to 100 ms of cross-relaxation.

Analysis of a relayed NOESY experiment may help in the sequential assignment process in cases in which the $^1H^\alpha$ protons of adjacent residues are degenerate. The sequential assignment process relies on the observation of NOEs from $^1H^N$ of residue i to $^1H^N$, $^1H^\alpha$, *and* $^1H^\beta$ of residue $i-1$. For peptide sections in an extended conformation, the sequential $^1H^N$–$^1H^N$ and $^1H^N$–$^1H^\beta$ NOEs are of zero or low intensity; degeneracy of the $^1H^\alpha$ resonances of adjacent residues will stymie the assignment procedure (the important sequential NOE will be overlapped with the intraresidue $^1H^N$–$^1H^\alpha$ NOE of residue $i-1$). In the relayed NOESY experiment, $^1H^N$ and $^1H^\beta$ resonance positions of residue $i-1$ are recorded in t_1, then this magnetization is passed on to $^1H^\alpha$ of

residue $i-1$ during the isotropic mixing and then to $^1H^N$ of residue i during the NOE mixing period. Intense sequential $^1H^{\beta}$–$^1H^N$ and $^1H^N$–$^1H^N$ NOE cross-peaks result from this process, allowing the sequential assignment process to continue. In the relayed NOESY spectrum, cross-peaks no longer have a direct dependence on the distance between the protons at the F_2 and F_1 frequencies of the cross-peak, and such data should be used for assignment purposes only. An example is shown in Fig. 6.58, where many sequential $^1H^N$–$^1H^N$ NOEs

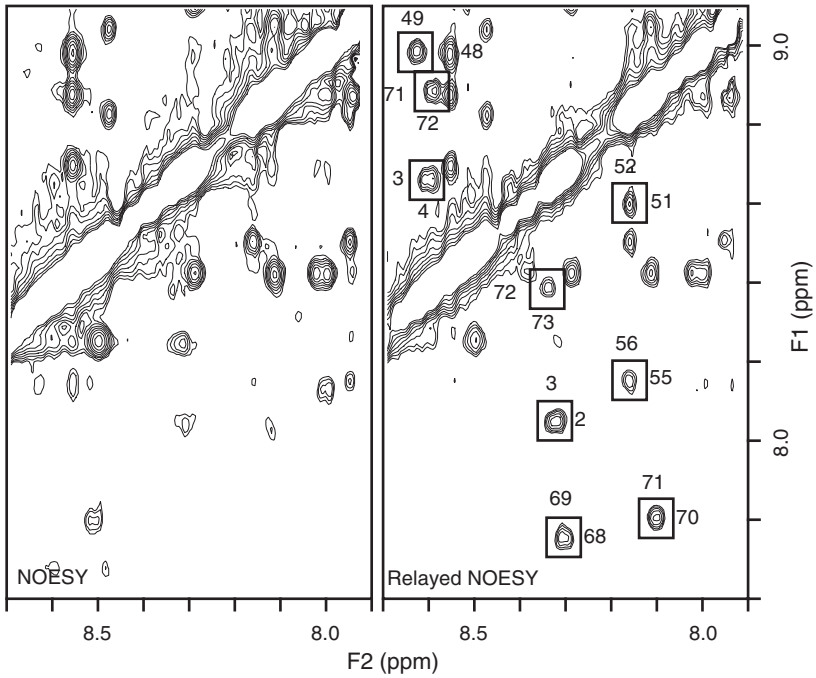

FIGURE 6.58 Comparison of sections of NOESY (left) and relayed NOESY (right) spectra. Both experiments were performed under identical conditions except for the mixing period, which included 27 ms of DIPSI-2rc isotropic mixing in the relayed NOESY. Weak coherent irradiation was used to suppress the solvent before the experiment and during the 100-ms NOE mixing period. Relayed NOESY peaks outlined by boxes indicate sequential $^1H^N$–$^1H^N$ NOEs between residues in the β-sheet of ubiquitin that are weak or not observed in the conventional NOESY experiment. The greater intensity allows sequential assignments to be made even if sequential $^1H^{\alpha}$ resonances are degenerate (as is the case for His68 and Leu69). The labels denote residue numbers of the amide protons contributing to each cross-peak.

readily are observable in the relayed NOESY experiment but are of negligible intensity in the normal NOESY experiment.

6.6.2 ROESY

Rotating-frame Overhauser Effect Spectroscopy (ROESY) was first developed by Bothner-By and co-workers and was initially known by the acronym CAMELSPIN (cross-relaxation appropriate for mini-molecules emulated by locked spins) (*96*). As both names suggest, the experiment monitors cross-relaxation between spins that are spin-locked by the application of rf pulses (*96*, *97*). ROESY has the advantage that the rotating-frame Overhauser effect (ROE) cross-relaxation rate constant is positive for *all* rotational correlation times: the maximum size of the ROE varies from 0.38 for $\omega_0\tau_c \ll 1$ to 0.68 for $\omega_0\tau_c \gg 1$. Therefore, ROESY cross-peaks are observable even if $\omega_0\tau_c \approx 1$; in contrast, cross-peaks vanish in laboratory-frame NOESY experiments if $\omega_0\tau_c \approx 1$. ROESY is very useful in studies of peptides in which laboratory frame NOEs are weak, but the experiment also has merits appropriate for the study of proteins. ROESY, NOESY (Section 6.6.1), and TOCSY (Section 6.5) are experimentally very similar; consequently, comparisons to NOESY and TOCSY will be made throughout this discussion. A more detailed discussion of relaxation in the rotating frame is given in Section 5.4.3.

6.6.2.1 Product Operator Analysis The original version of the ROESY experiment simply consisted of a 90°–t_1–τ_m–t_2, sequence in which the spin-locking field during τ_m was provided by continuous low-power irradiation (2–4 kHz), as illustrated in Fig. 6.59a. For a scalar-coupled two-spin system, the evolution up to the mixing period is given by

$$\begin{aligned} I_{1z} \xrightarrow{\left(\frac{\pi}{2}\right)_x - t_1} & - I_{1y} \cos(\Omega_1 t_1) \cos(\pi J_{12} t_1) + 2I_{1x}I_{2z} \cos(\Omega_1 t_1) \sin(\pi J_{12} t_1) \\ & + I_{1x} \sin(\Omega_1 t_1) \cos(\pi J_{12} t_1) + 2I_{1y}I_{2z} \sin(\Omega_1 t_1) \sin(\pi J_{12} t_1). \end{aligned} \quad [6.53]$$

During the subsequent spin-locking period (with a y-phase rf field), any operators orthogonal to the rf field in a tilted rotating frame are dephased by rf inhomogeneity (Section 3.4.3). The x-axes of the rotating and tilted reference frames are coincident; thus, all terms containing x-operators are dephased. The transformation of z- and y-operators into

the tilted frame is performed using [5.89]:

$$\begin{aligned} I_{1y} &\Rightarrow I'_{1z}\ \sin\theta_1 + I'_{1y}\ \cos\theta_1, \\ 2I_{1y}I_{2z} &\Rightarrow 2\Big(I'_{1z}\ \sin\theta_1 + I'_{1y}\ \cos\theta_1\Big)\Big(I'_{2z}\ \cos\theta_2 - I'_{2y}\ \sin\theta_2\Big) \\ &= 2I'_{1z}I'_{2z}\ \sin\theta_1\ \cos\theta_2 - 2I'_{1z}I'_{2y}\ \sin\theta_1\ \sin\theta_2 \\ &\quad + 2I'_{1y}I'_{2z}\ \cos\theta_1\ \cos\theta_2 - 2I'_{1y}I'_{2y}\ \cos\theta_1\ \sin\theta_2, \end{aligned} \qquad [6.54]$$

in which θ_1 and θ_2 are the tilt angles for spins I_1 and I_2. The only terms that commute with the spin lock Hamiltonian are proportional to I'_{1z} and $2I'_{1z}I'_{2z}$. If $K-1$ spins (I_k for $k=2,\ldots,K$) are close in space to spin I_1, the resulting evolution of the longitudinal magnetization is

$$\begin{aligned} &-I'_{1z}\ \sin\theta_1\ \cos(\Omega_1 t_1)\ \cos(\pi J_{12} t_1) \\ &\quad \xrightarrow{\tau_m} -\sum_{k=1}^{K} I'_{kz} a_{1k}(\tau_m)\ \sin\theta_1\ \cos(\Omega_1 t_1)\ \cos(\pi J_{12} t_1), \end{aligned} \qquad [6.55]$$

in which $a_{1k}(\tau_m) = [\exp(-\mathbf{R}\tau_m)]_{1k}$ is the (1, k)th element of the matrix exponential and $\mathbf{R}$ is the matrix of rotating-frame relaxation rate constants $R_{kk}(\theta_i)$ and $\sigma_{jk}(\theta_i, \theta_j)$ (Section 5.4.3). Transforming back from the tilted frame to the rotating frame yields the observable operators:

$$\sum_{k=1}^{K} I_{ky} a_{1k}(\tau_m)\ \sin\theta_1\ \sin\theta_k\ \cos(\Omega_1 t_1)\ \cos(\pi J_{12} t_1). \qquad [6.56]$$

The first term represents a diagonal peak and the remaining $K-1$ terms represent cross-peaks. Diagonal peaks and cross-peaks have in-phase absorptive lineshapes in F_1 and F_2. In the usual methods of acquisition, the cross-peaks are of phase opposite to the diagonal because ρ_j and σ_{jk} are both positive (*96*).

The two-spin term $2I'_{1z}I'_{2z}$ does not cross-relax with other I_1 or I_2 spin operators during τ_m; however the amplitude of the operator is reduced by relaxation (with relaxation rate constant designated R_{zz}). Transformation back into the rotating frame yields the observable operators:

$$\begin{aligned} &\big(2I_{1y}I_{2z}\ \sin\theta_1\ \cos\theta_2 + 2I_{1z}I_{2y}\ \cos\theta_1\ \sin\theta_2\big) \\ &\quad \times \sin\theta_1\ \cos\theta_2\ \sin(\Omega_1 t_1)\ \sin(\pi J_{12} t_1)\ \exp(-R_{zz}\tau_m). \end{aligned} \qquad [6.57]$$

The limitations of the simple ROESY experiment are now evident: (*i*) amplitude of cross-peaks are reduced by a factor of $\sin\theta_1 \sin\theta_2$ and

(*ii*) two-spin order generates cross-peaks with antiphase lineshapes in both dimensions that distort the in-phase multiplet patterns expected for ROESY cross-peaks.

Griesinger and Ernst developed a simple and clever modification to the ROESY pulse sequence that overcomes these limitations. In this sequence (Fig. 6.59b), evolution through the 90°_x–t_1–90°_x block proceeds as described in [6.1].

$$\begin{aligned} I_{1z} \xrightarrow{\left(\frac{\pi}{2}\right)_x - t_1 - \left(\frac{\pi}{2}\right)_x} & -I_{1z}\cos(\Omega_1 t_1)\cos(\pi J_{12} t_1) - 2I_{1x}I_{2y}\cos(\Omega_1 t_1)\sin(\pi J_{12} t_1) \\ & +I_{1x}\sin(\Omega_1 t_1)\cos(\pi J_{12} t_1) - 2I_{1z}I_{2y}\sin(\Omega_1 t_1)\sin(\pi J_{12} t_1). \end{aligned} \quad [6.58]$$

Again, y-operators are dephased by the spin lock rf field. Transformation of the z- and x-operators into the tilted frame yields

$$\begin{aligned} & -I_{1z}\cos(\Omega_1 t_1)\cos(\pi J_{12} t_1) + I_{1x}\sin(\Omega_1 t_1)\cos(\pi J_{12} t_1) \\ & \quad \Rightarrow -\left(-I'_{1x}\sin\theta_1 + I'_{1z}\cos\theta_1\right)\cos(\Omega_1 t_1)\cos(\pi J_{12} t_1) \\ & \qquad + \left(I'_{1x}\cos\theta_1 + I'_{1z}\sin\theta_1\right)\sin(\Omega_1 t_1)\cos(\pi J_{12} t_1). \end{aligned} \quad [6.59]$$

The only term that commutes with the spin lock Hamiltonian is

$$\begin{aligned} & -I'_{1z}(\cos\theta_1\cos(\Omega_1 t_1) - \sin\theta_1\sin(\Omega_1 t_1))\cos(\pi J_{12} t_1) \\ & \quad = -I'_{1z}\cos(\Omega_1 t_1 + \theta_1)\cos(\pi J_{12} t_1). \end{aligned} \quad [6.60]$$

Cross-relaxation during τ_m yields

$$\begin{aligned} & -I'_{1z}\cos(\Omega_1 t_1 + \theta_1)\cos(\pi J_{12} t_1) \\ & \quad \xrightarrow{\tau_m} -\sum_{k=1}^{K} I'_{kz} a_{1k}(\tau_m)\cos(\Omega_1 t_1 + \theta_1)\cos(\pi J_{12} t_1). \end{aligned} \quad [6.61]$$

Transforming back from the tilted frame to the rotating frame and applying the last 90° pulse yields the observable operators:

$$\sum_{k=1}^{K}\left(I_{ky}\cos\theta_k - I_{kx}\sin\theta_k\right)a_{1k}(\tau_m)\cos(\Omega_1 t_1 + \theta_1)\cos(\pi J_{12} t_1). \quad [6.62]$$

The offset dependence of the ROESY cross-peaks appears in [6.62] as a phase error of θ_1 in t_1 and θ_k in t_2. Because θ_k is approximately linear for $0 \le \Omega_k \le \gamma B_1$ (Section 3.4.1), the resonance offset effects are compensated by phase correction during processing. No two-spin operators that commute with the spin lock Hamiltonian are created; therefore,

the cross-peak multiplet structure is undistorted (minor contributions from evolution of zero-quantum coherences in the tilted frame have been ignored).

Although the Griesinger and Ernst approach eliminates the offset dependence that arises from the projection of the spin operators between tilted and untilted frames, the magnitudes of cross-relaxation rate constants in a ROESY experiment also depend upon resonance offset as shown by [5.140]. As a result, relaxation for off-resonance spins will contain a laboratory-frame component (i.e., an NOE) as well as a rotating-frame component. Interestingly (and somewhat counterintuitively) for large biomolecules, the apparent offset-dependent cross-relaxation rate between two spins is actually most efficient for cross-peaks along the antidiagonal and least efficient for cross-peaks close to the diagonal away from the center of the spectrum (*98*). Any quantitative analysis of ROESY cross-peak intensities must consider the offset dependence of the rate constants.

A practical problem encountered in the ROESY experiment is that the spin lock pulse is capable of inducing coherence transfer (*52*). The TOCSY (or *J*) cross-peaks are of the same sign as the diagonal (Section 6.5); consequently, TOCSY transfer within a scalar-coupled system tends to cancel the cross-relaxation components and render quantitation of the ROE (and hence the interproton separation) difficult. More insidiously, cross-peaks that arise through consecutive TOCSY and ROE magnetization transfers have the same sign as do the actual ROE peaks (*99*) and can be misinterpreted. Fortunately, a long, weak pulse is not efficient at achieving a Hartmann–Hahn match between two protons unless they are close in chemical shift or symmetrically disposed about the carrier position (Fig. 6.47a). Unambiguous ROE cross-peaks can be identified by recording two ROESY spectra with very different rf carrier offsets (*99*). Development of pulse sequences that eliminate TOCSY transfer and generate pure ROE cross-peaks is an area of active research (*100*, *101*).

6.6.2.2 Experimental Protocol and Processing In order to achieve baselines flat enough to allow accurate quantitation of cross-peak intensities, the points discussed for the TOCSY and NOESY spectra (Sections 6.5.2 and 6.6.1.2) are also pertinent in the ROESY experiment. In addition, parameters must be chosen for the spin lock mixing period. Sample heating and minimization of *J* transfer are jointly accommodated by using weak spin lock field strengths (2–5 kHz), although the offset dependence of the ROE may be nontrivial in such cases. The ROE builds up at a rate twice that of the laboratory-frame NOE (Section

5.4.3); therefore, shorter mixing times are required to obtain ROE peaks comparable in size to their NOESY counterparts. For proteins, mixing times are usually kept short (40–200 ms). The absorptive in-phase lineshape expected for diagonal and cross-peaks in the ROESY spectrum indicates that processing will be very similar to the procedures already described for TOCSY and NOESY (Sections 6.5.3 and 6.6.1.3).

ROESY spectra were recorded with the pulse sequences shown in a and b of Fig. 6.59. Thirty-two transients were collected for each of 512 t_1 increments ($t_{1\max} = 44$ ms). The spins were locked by a continuous

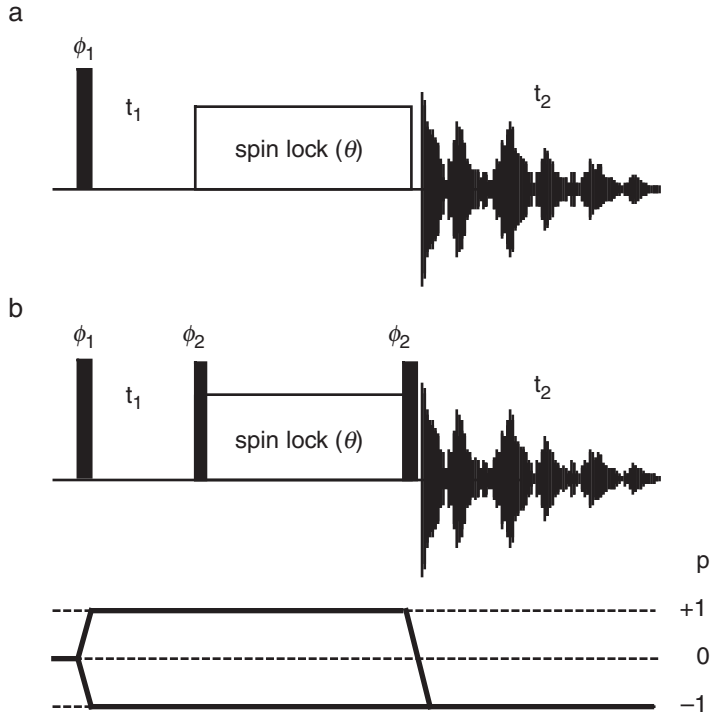

Figure 6.59 Pulse sequences and coherence level diagram for the ROESY experiments. (a) The basic phase cycle is $\phi_1 = x, -x$ and receiver $= x, -x$. The spin lock phase $\theta = y$. (b) The basic phase cycle is $\phi_1 = x, -x$; $\phi_2 = x, x$; and receiver $= x, -x$. The spin lock phase $\theta = x$. The full phase cycle is completed by performing CYCLOPS on all pulses and the receiver. Frequency discrimination in F_1 is obtained by shifting the phase of ϕ_1 and the receiver according to the TPPI, States, or TPPI–States protocols (Section 4.3.4).

low-power pulse (2.5 kHz field strength) of 40-ms duration. Sections of the spectra are shown in a and b of Fig. 6.60. The increased cross-peak amplitude obtained with the pulse sequence of Fig. 6.59b is illustrated in Fig. 6.60c.

6.6.2.3 Information Content Although resonance offset effects hinder quantitation of ROESY spectra, the ROESY experiment has several redeeming qualities for studies of proteins. Foremost, as discussed previously, the ROE is always positive and cross-peaks can be observed in ROESY spectra even if the peaks cannot be observed in NOESY spectra because $\omega_0\tau_c \approx 1$ (Section 5.4.3).

A further advantage of ROESY over NOESY is that spin diffusion (or three-spin effects) produces contributions to cross-peaks that are of sign opposite to the sign of direct ROE peaks. Conceptually, the rotating-frame cross-relaxation rate constant is positive, and magnetization transfer between two spins occurs with inversion of sign. Thus, a diagonal peak and a cross-peak arising by a direct ROE between two spins have opposite signs. Transfer of the cross-peak magnetization to a third spin involves another change of sign. As a result, cross-peaks dominated by spin diffusion will be of the same sign as the diagonal has. If a small three-spin interaction contributes to a ROESY cross-peak, the measured intensity is reduced and may be interpreted as a longer interproton separation. Consequently, the upper bound restraint applied in structure calculations will not be overly restrictive.

The influence of spin diffusion in NOESY spectra is particularly pronounced for NOEs involving geminal methylene groups. Efficient spin diffusion between the $^1H^{\beta''}$ and $^1H^{\beta'}$ tends to equalize the intensity of NOEs to other protons even if the distances to $^1H^{\beta''}$ and $^1H^{\beta'}$ are not equal. Stereospecific assignment of β-methylene protons plays an important role in defining side chain conformation and depends heavily on estimating the relative sizes of intraresidue and sequential distances to $^1H^{\beta''}$ and $^1H^{\beta'}$ (*102, 103*). The use of ROESY spectra for this process significantly reduces the chance of incorrectly making such assignments.

Another important facet of the ROESY experiment is that chemical exchange peaks are of the same sign as the diagonal, i.e., opposite in sign to peaks arising from direct cross-relaxation. Thus, rotating-frame experiments are invaluable in the study of dynamic processes involving slow exchange between two or more states. Protein–protein or peptide–protein interactions are one area where discrimination of cross-relaxation and chemical exchange is not possible from NOESY, but is apparent from ROESY data. As with chemical exchange in TOCSY

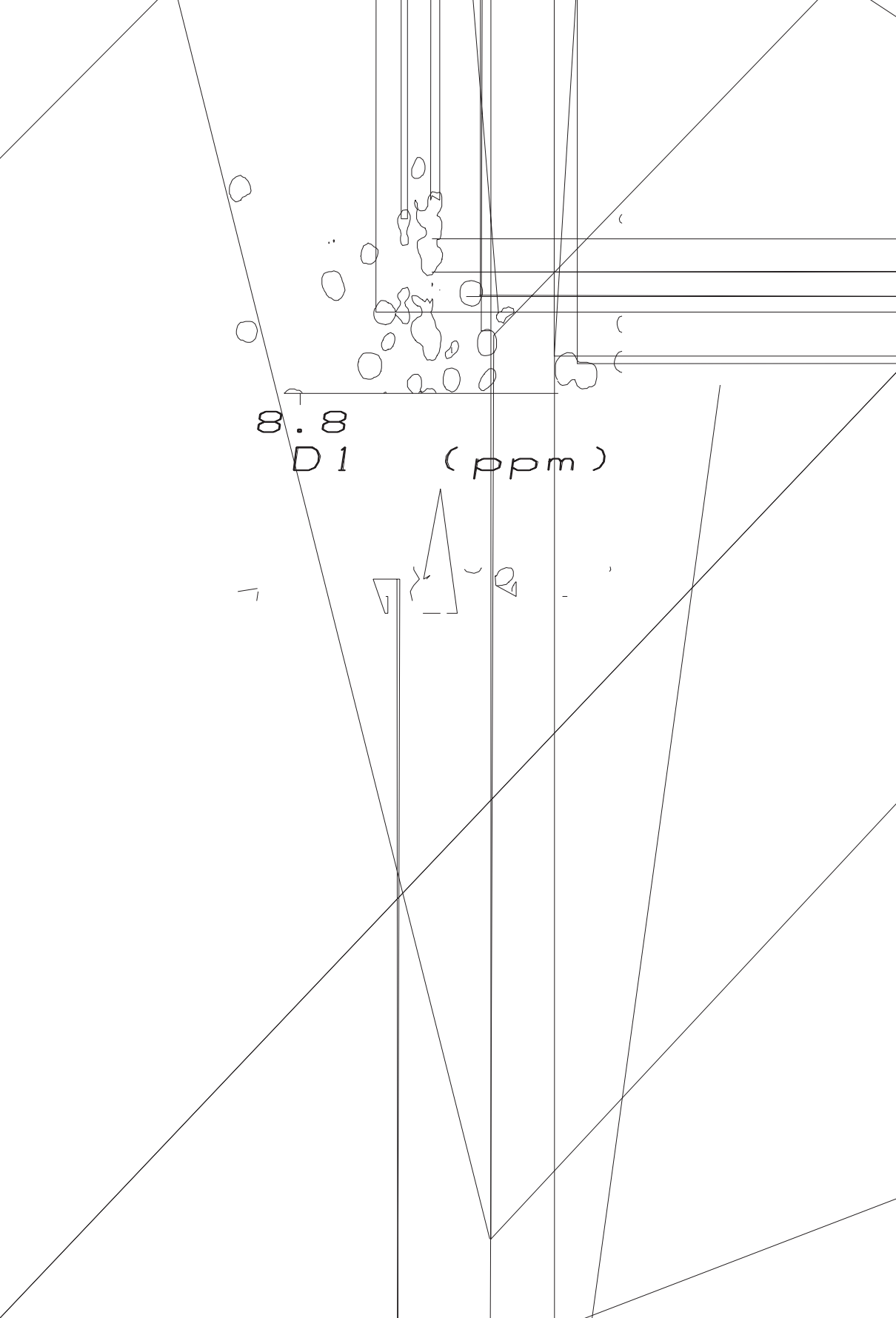
8.8
D1 (ppm)

spectra (*73*), complex situations can arise where peaks result from both cross-relaxation and exchange.

6.6.2.4 Experimental Variants Just as in the JR.NOESY, ROESY experiments frequently are acquired without presaturation of the solvent resonance. A variety of suppression techniques have been devised that accomplish this (the jump–return sequence cannot be used effectively following the spin lock pulse) (*93*), some of which have been discussed in Section 3.5.3. One possible pulse sequence is shown in Fig. 6.61. This sequence is derived from that shown in Fig. 6.59b by adding the excitation-sculpting segment for water suppression.

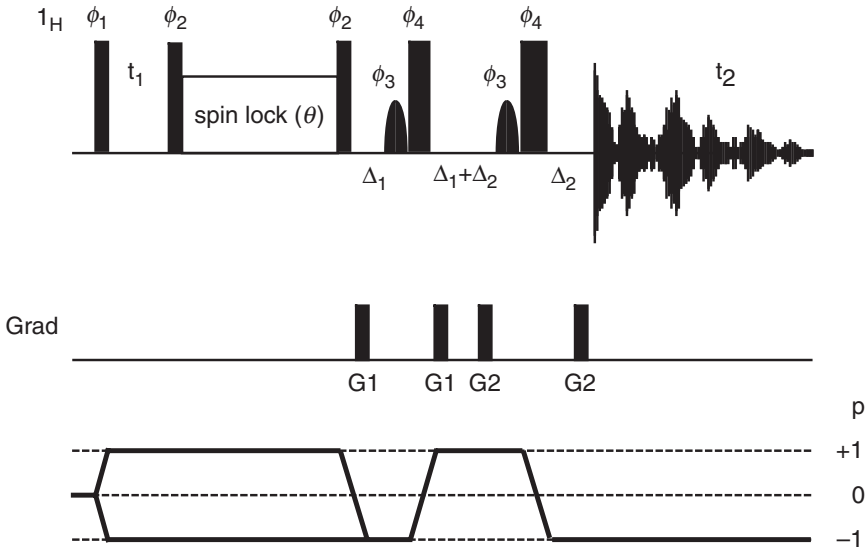

FIGURE 6.61 Pulse sequence and coherence level diagram for a ROESY experiment acquired from H_2O solution using excitation sculpting to avoid presaturation of the water resonance. The curved pulse shapes indicate selective 180° pulses at the water frequency. The basic phase cycle is $\phi_1 = 2(x, -x)$; $\phi_2 = 4(x)$; $\phi_3 = -y, -y, y, y$; $\phi_4 = y, y, -y, -y$; and receiver $= 2(x, -x)$. The spin lock phase $\theta = x$. The full phase cycle is completed by performing CYCLOPS on all pulses and the receiver. Frequency discrimination in F_1 is obtained by shifting the phase of ϕ_1 and the receiver according to the TPPI, States, or TPPI–States protocols (Section 4.3.4). A bipolar pair of gradients can be inserted into the t_1 period to prevent radiation damping (*31*).

6.7 ^{1}H 3D Experiments

Given the vast improvement in effective resolution between 1D and 2D NMR spectra, 3D NMR spectroscopy is a logical approach to increasing the effective resolution still further. The increase in dimensionality from 2D to 3D is achieved by inserting a second incrementable delay and mixing period immediately before the acquisition period of a normal 2D experiment, as was discussed in Section 4.5 and shown schematically in Fig. 4.17. The first example of a 3D NMR experiment useful in the study of proteins was reported in 1988 (*104*), and combined NOESY and TOCSY mixing with the measurement of proton frequencies in all three dimensions.

The acquisition of 3D homonuclear NMR spectra introduces many technical challenges. The digital resolution in the indirect dimensions needs to be reasonably high because of the large number of protons and their relatively poor chemical shift dispersion. Simultaneously, the total acquisition time must be minimized because two evolution delays have to be incremented independently. As a consequence, such spectra are acquired with minimal digital resolution in t_1 and t_2 (usually less than 128 complex data points are collected) and with relatively few transients (never more than 16). The phase cycle must be chosen with great care so as to achieve the maximum amount of artifact suppression in the fewest steps. Even with optimization of conditions, homonuclear 3D experiments commonly require four to eight days to acquire. Improvements in digital resolution (or a reduction in the total acquisition time) may be obtained by the use of selective pulses to limit the frequencies observed in one or both of the indirectly detected dimensions (*105–107*).

Aside from the technical issues, homonuclear 3D spectra are much more complicated than 2D spectra. For a protein the size of ubiquitin, 2000 to 3000 individual cross-peaks are observable in the 2D NOESY spectrum; in the corresponding homonuclear 3D NOESY–TOCSY spectrum, approximately five times as many cross-peaks might be observed because the magnetization transferred between spins by a particular NOE interaction (generating one cross-peak in the 2D spectrum) is transferred to all of the spins in the same spin system by the isotropic mixing. In contrast, heteronuclear 3D and 4D spectra have similar numbers of cross-peaks as 2D experiments (Chapter 7). Thus, although homonuclear 3D experiments were developed first, heteronuclear multidimensional spectroscopy experiments, because of the greater simplicity and superior resolving power, are preferable.

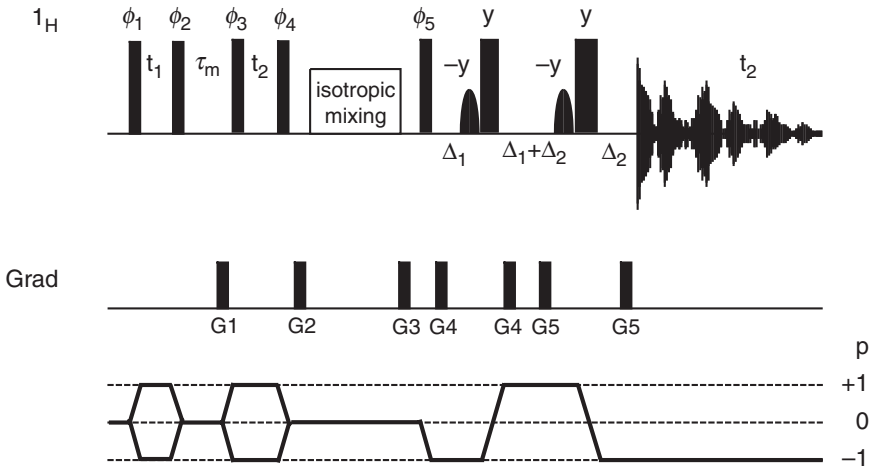

FIGURE 6.62 Pulse program and coherence level diagram for a homonuclear 3D NOESY–TOCSY experiment. An excitation-sculpting segment is included prior to detection to avoid presaturation of the water resonance. The DIPSI mixing pulses are of y phase, and the phases of the pulses are cycled as follows: $\phi_1 = 2(x, -x, y, -y)$; $\phi_2 = 2(-x, -x, -y, -y)$; $\phi_3 = -x, -x, -y, -y, x, x, y, y$; $\phi_4 = 2(x, x, y, y)$; $\phi_5 = 2(x, x, y, y)$; $\phi_6 = 8(y)$; $\phi_7 = 8(-y)$; and receiver $= x, -x, y, -y, -x, x, -y, y$. Frequency discrimination in F_1 (F_2) is obtained by shifting the phase of ϕ_1 (ϕ_3) and the receiver according to the TPPI, States, or TPPI–States protocols (Section 4.3.4).

Nevertheless, homonuclear 3D spectra can offer additional information in cases where isotopic labeling is not possible.

The main implementation of homonuclear 3D spectroscopy in the study of proteins combines NOESY and TOCSY mixing because both mechanisms transfer in-phase magnetization and produce lineshapes that do not suffer from self-cancellation under conditions of limiting digital resolution. The pulse sequence for a 3D NOESY–TOCSY experiment is shown in Fig. 6.62.

6.7.1 EXPERIMENTAL PROTOCOL

The precautions already described to obtain flat baselines in 2D TOCSY (Section 6.5.2) and NOESY (Section 6.6.1.2) spectra are also relevant for 3D spectroscopy, with the additional limitation that the phase cycle must be kept to a bare minimum. The eight-step phase cycle described in Fig. 6.62 should be considered a starting point for

optimization of this experiment on a given spectrometer; the dominant artifacts will vary from one spectrometer to another and some optimization may be necessary. Assuming that the artifact level is acceptable from eight transients, then 256 increments can be collected for both t_1 and t_2 in just over a week of spectrometer time.

6.7.2 Processing

Not only is the acquisition of a homonuclear 3D experiment time consuming, but processing also provides challenges. In general, processing strategies discussed for TOCSY (Section 6.5.3) and NOESY (Section 6.6.1.3) experiments are applied to 3D spectra as well. However, even modest zero-filling can lead to excessively large data matrices, and using linear prediction or maximum entropy reconstruction to improve the resolution in F_1 and F_2 is a considerable computational burden. During the initial stages of resonance assignment, the peaks of most interest involve amide protons in F_3; therefore, processing can be simplified by saving only this region after the t_3 Fourier transformation.

6.7.3 Information Content

Homonuclear 3D spectra are analyzed with the aim of obtaining resonance assignments or to obtain interproton distance restraints from the unambiguous assignment of NOE peaks. However, the spectra contain a vast number of redundant cross-peaks, and complete analysis (as might be performed for a 2D spectrum) is not an attractive proposition unless the process is assisted by computer automation. Alternatively, certain regions of the 3D spectrum may be analyzed in detail to resolve specific ambiguities arising from the 2D spectra.

The most intense peaks lie along the body-diagonal at $F_1 = F_2 = F_3$ and arise from magnetization that has not been transferred during either mixing period. The next most intense peaks arise from transfer by either NOE *or* TOCSY, but not both. The former occur in the $F_2 = F_3$, or NOE, plane, while the latter occur in the $F_1 = F_2$, or TOCSY, plane. The weakest cross-peaks arise from NOE *and* TOCSY transfer and are sometimes referred to as *real* or *true* 3D cross-peaks because they have no equivalent in 2D spectra. Further, the 3D cross-peaks in the $F_1 = F_3$ plane are referred to as *back-transfer* peaks, as they arise from transfer from one proton to a second during the NOE mixing, and then *back* to the first proton during the isotropic mixing. Analysis of the 3D spectrum is most readily accomplished from 2D plots corresponding to F_1–F_2 or F_1–F_3 planes; the intersection of these planes with the NOE,

TOCSY, and back-transfer planes gives rise to the NOE, TOCSY, and back-transfer lines, respectively, which play an important role in analysis of the spectrum (*108*, *109*).

Information additional to that present in 2D spectra is contained in the peaks with $F_1 \neq F_2 \neq F_3$. Note that the intensity of the peaks will depend on the efficiency of transfer via both dipolar relaxation *and* isotropic mixing. Because cross-peak intensity is not related directly to the NOE between the spins, calibration of interproton distances cannot be performed in a precise manner. The dependence of cross-peak intensity on the rate of TOCSY transfer can be especially problematic for the amide protons of helical residues; the small value of $^3J_{H^NH^\alpha}$ will reduce the size of all correlations, even if the interproton separation is relatively short.

Finally, although the 3D spectra may be able to resolve correlations that are overlapped in 2D spectra, correlations between two protons with identical chemical shifts still cannot be observed. Either four proton dimensions or a single proton and two heteronuclear dimensions (e.g., the HMQC–NOESY–HMQC; Section 7.2.4) are required to observe such cross-peaks.

6.7.4 EXPERIMENTAL VARIANTS

Several variants of homonuclear 3D experiments have been described that differ from the example described here in the choice of mixing schemes. Thus, the 3D TOCSY–NOESY has been proposed as a complementary method of performing the 3D NOESY–TOCSY experiment. Because both experiments have one TOCSY and one NOESY mixing period, the information content is identical, although cross-peaks containing equivalent information will be present in different regions of the spectra. Thus, if a particular cross-peak is obscured by some artifact in one type of spectrum, equivalent information may be present in an artifact-free region of the other experiment. In addition, a jump–return read pulse (Section 3.5.2) can be incorporated into the TOCSY–NOESY experiment, improving solvent suppression and allowing the observation of peaks close to the water resonance (*110*, *111*).

Homonuclear 3D spectra have also been used to study spin diffusion pathways by utilizing NOESY transfer during both mixing periods in the 3D NOESY–NOESY experiment (*112*). In such a spectrum, the intensity of a true 3D cross-peak between spins I_1, I_2, and I_3 at $F_1 = \Omega_1$, $F_2 = \Omega_2$ and $F_3 = \Omega_3$ depends upon the product of the cross-relaxation rates, σ_{12} and σ_{23}, and thus has intensity comparable to the spin diffusion

contribution to a peak between I_1 and I_3 in a 2D NOESY spectrum [6.52]. This is one of the few direct experimental methods to investigate spin diffusion pathways. The 3D NOESY–NOESY spectra have been used for complete resonance assignments and identification of the secondary structure present in a protein (*113, 114*). Finally, 3D TOCSY–TOCSY spectra have been used as an aid to automated resonance assignment routines (*115*). This experiment has the advantage that spectra of high quality can be obtained with very little phase cycling, and total acquisition times can be kept short.

References

1. D. S. Wishart, F. M. Richards, *FEBS Lett*. **293**, 72–80 (1991).
2. D. S. Wishart, B. D. Sykes, F. M. Richards, *J. Mol. Biol*. **222**, 311–333 (1991).
3. J. Jeener, Ampère Summer School, Basko Polje, Yugoslavia, 1971.
4. W. P. Aue, E. Bartholdi, R. R. Ernst, *J. Chem. Phys*. **64**, 2229–2246 (1976).
5. D. Marion, K. Wüthrich, *Biochem. Biophys. Res. Commun*. **113**, 967–974 (1983).
6. D. Neuhaus, G. Wagner, M. Vasak, J. H. R. Kägi, K. Wüthrich, *Eur. J. Biochem*. **151**, 257–273 (1985).
7. H. Widmer, K. Wüthrich, *J. Magn. Reson*. **74**, 316–336 (1987).
8. Y. Kim, J. H. Prestegard, *J. Magn. Reson*. **84**, 9–13 (1990).
9. L. J. Smith, M. J. Sutcliffe, C. Redfield, C. M. Dobson, *Biochemistry* **30**, 986–996 (1991).
10. S. Ludvigsen, K. V. Andersen, F. M. Poulsen, *J. Mol. Biol*. **217**, 731–736 (1991).
11. J. J. Titman, J. Keeler, *J. Magn. Reson*. **89**, 640–646 (1990).
12. L. McIntyre, R. Freeman, *J. Magn. Reson*. **96**, 425–431 (1992).
13. T. Szperski, P. Güntert, G. Otting, K. Wüthrich, *J. Magn. Reson*. **99**, 552–560 (1992).
14. C. Griesinger, O. W. Sørensen, R. R. Ernst, *J. Magn. Reson*. **75**, 747–492 (1987).
15. D. Marion, B. Bax, *J. Magn. Reson*. **80**, 528–533 (1988).
16. L. Mueller, *J. Magn. Reson*. **72**, 191–196 (1987).
17. G. Otting, K. Wüthrich, *J. Magn. Reson*. **75**, 546–549 (1987).
18. S. C. Brown, P. L. Weber, L. Mueller, *J. Magn. Reson*. **77**, 166–169 (1988).
19. G. Eich, G. Bodenhausen, R. R. Ernst, *J. Am. Chem. Soc*. **104**, 3731–3732 (1982).
20. A. Bax, G. Drobny, *J. Magn. Reson*. **61**, 306–320 (1985).
21. W. J. Chazin, K. Wüthrich, *J. Magn. Reson*. **72**, 358–363 (1987).
22. G. Wagner, *J. Magn. Reson*. **55**, 151–156 (1983).
23. W. J. Chazin, M. Rance, P. E. Wright, *J. Mol. Biol*. **202**, 603–622 (1988).
24. M. Rance, O. W. Sørensen, G. Bodenhausen, G. Wagner, R. R. Ernst, K. Wüthrich, *Biochem. Biophys. Res. Commun*. **117**, 479–485 (1983).
25. U. Piantini, O. W. Sørensen, R. R. Ernst, *J. Am. Chem. Soc*. **104**, 6800–6801 (1982).
26. A. J. Shaka, R. Freeman, *J. Magn. Reson*. **51**, 169–173 (1983).
27. N. Müller, R. R. Ernst, K. Wüthrich, *J. Am. Chem. Soc*. **108**, 6482–6492 (1986).
28. P. C. M. van Zijl, M. O'Neil Johnson, S. Mori, R. E. Hurd, *J. Magn. Reson., Ser A* **113**, 265–270 (1995).
29. A. L. Davis, E. D. Laue, J. Keeler, D. Moskau, J. J. Lohman, *J. Magn. Reson*. **94**, 637–644 (1991).

30. D. L. Mattiello, W. S. Warren, L. Mueller, B. T. Farmer, *J. Am. Chem. Soc.* **118**, 3253–3261 (1996).
31. V. Sklenář, *J. Magn. Reson., Ser A* **114**, 132–135 (1995).
32. A. E. Derome, M. P. Williamson, *J. Magn. Reson.* **88**, 177–185 (1990).
33. C. J. Turner, *J. Magn. Reson.* **96**, 551–562 (1992).
34. M. Rance, C. Dalvit, P. E. Wright, *Biochem. Biophys. Res. Commun.* **131**, 1094–1102 (1985).
35. N. Müller, G. Bodenhausen, K. Wüthrich, R. R. Ernst, *J. Magn. Reson.* **65**, 531–534 (1985).
36. M. Rance, P. E. Wright, *Chem. Phys. Lett.* **124**, 572–575 (1986).
37. M. Rance, W. J. Chazin, C. Dalvit, P. E. Wright, *Meth. Enzymol.* **176**, 114–134 (1989).
38. C. Griesinger, O. W. Sørensen, R. R. Ernst, *J. Magn. Reson.* **75**, 474–492 (1987).
39. Z. L. Madi, C. Griesinger, R. R. Ernst, *J. Am. Chem. Soc.* **112**, 2908–2914 (1990).
40. C. Griesinger, O. W. Sørensen, R. R. Ernst, *J. Chem. Phys.* **85**, 6837–6852 (1986).
41. L. Braunschweiler, G. Bodenhausen, R. R. Ernst, *Mol. Phys.* **48**, 535–560 (1983).
42. C. Dalvit, M. Rance, P. E. Wright, *J. Magn. Reson.* **69**, 356–361 (1986).
43. M. Levitt, R. Freeman, *J. Magn. Reson.* **33**, 473–476 (1979).
44. G. Otting, K. Wüthrich, *J. Magn. Reson.* **66**, 359–363 (1986).
45. G. Wagner, E. R. P. Zuiderweg, *Biochem. Biophys. Res. Commun.* **113**, 854–860 (1983).
46. D. L. Di Stefano, A. J. Wand, *Biochemistry* **26**, 7272–7281 (1987).
47. P. L. Weber, S. C. Brown, L. Mueller, *Biochemistry* **26**, 7282–7290 (1987).
48. M. Rance, *J. Am. Chem. Soc.* **110**, 1973–1974 (1988).
49. L. Mueller, P. Legault, A. Pardi, *J. Am. Chem. Soc.* **117**, 11043–11048 (1995).
50. V. V. Krishnan and M. Rance, *J. Magn. Reson., Ser A* **116**, 97–106 (1995).
51. W. J. Chazin, *J. Magn. Reson.* **91**, 517–526 (1991).
52. L. Braunschweiler, R. R. Ernst, *J. Magn. Reson.* **53**, 521–528 (1983).
53. A. Bax, D. G. Davis, *J. Magn. Reson.* **65**, 355–360 (1985).
54. M. Rance, *J. Magn. Reson.* **74**, 557–564 (1987).
55. M. Rance, *Chem. Phys. Lett.* **154**, 242–247 (1989).
56. J. Cavanagh, W. J. Chazin, M. Rance, *J. Magn. Reson.* **87**, 110–131 (1990).
57. R. Bazzo, I. D. Campbell, *J. Magn. Reson.* **76**, 358–361 (1988).
58. S. J. Glaser, G. P. Drobny, *Adv. Magn. Reson.* **14**, 35–58 (1990).
59. A. J. Shaka, J. Keeler, T. Frenkiel, R. Freeman, *J. Magn. Reson.* **52**, 335–338 (1983).
60. A. J. Shaka, J. Keeler, R. Freeman, *J. Magn. Reson.* **53**, 313–340 (1983).
61. A. J. Shaka, C. J. Lee, A. Pines, *J. Magn. Reson.* **77**, 274–293 (1988).
62. S. P. Rucker, A. J. Shaka, *Mol. Phys.* **68**, 509–517 (1989).
63. M. Kadkhodael, O. Rivas, M. Tan, A. Mohebbi, A. J. Shaka, *J. Magn. Reson.* **91**, 437–443 (1991).
64. Ē. Kupče, P. Schmidt, M. Rance, G. Wagner, *J. Magn. Reson.* **135**, 361–367 (1998).
65. A. E. Bennett, J. D. Gross, G. Wagner, *J. Magn. Reson.* **165**, 59–79 (2003).
66. W. Peti, C. Griesinger, W. Bermel, *J. Biomol. NMR* **18**, 195–205 (2000).
67. Ē. Kupče, W. Hiller, *Magn. Reson. Chem.* **39**, 231–235 (2001).
68. C. Griesinger, R. R. Ernst, *Chem. Phys. Lett.* **152**, 239–247 (1988).
69. C. Griesinger, G. Otting, K. Wüthrich, R. R. Ernst, *J. Am. Chem. Soc.* **110**, 7870–7872 (1988).
70. J. Cavanagh, M. Rance, *J. Magn. Reson.* **96**, 670–678 (1992).
71. J. Briand, R. R. Ernst, *Chem. Phys. Lett.* **185**, 276–285 (1991).
72. M. Kadkhodael, T.-L. Hwang, J. Tang, A. J. Shaka, *J. Magn. Reson., Ser. A* **105**, 104–107 (1993).

73. J. Feeney, C. J. Bauer, T. A. Frenkiel, B. Birdsall, M. D. Carr, G. C. K. Roberts, J. R. P. Arnold, *J. Magn. Reson.* **91**, 607–613 (1991).
74. M. A. Delsuc, J. Y. Lallemand, *J. Magn. Reson.* **69**, 504–507 (1986).
75. D. Marion, M. Ikura, A. Bax, *J. Magn. Reson.* **84**, 425–430 (1989).
76. G. Wagner, *Quart. Rev. Biophys.* **16**, 1–57 (1983).
77. D. Marion, M. Ikura, R. Tschudin, A. Bax, *J. Magn. Reson.* **85**, 393–399 (1989).
78. J. Cavanagh, M. Rance, *J. Magn. Reson.* **88**, 72–85 (1990).
79. F. Fogolari, G. Esposito, P. Viglino, *J. Magn. Reson., Ser. A* **102**, 49–57 (1993).
80. G. M. Clore, A. Bax, A. M. Gronenborn, *J. Biomol. NMR* **1**, 13–22 (1991).
81. S. Macura, Y. Huang, D. Suter, R. R. Ernst, *J. Magn. Reson* **43**, 259–281 (1981).
82. G. Otting, *J. Magn. Reson.* **86**, 496–508 (1990).
83. M. Rance, G. Bodenhausen, G. Wagner, K. Wüthrich, R. R. Ernst, *J. Magn. Reson.* **62**, 497–510 (1985).
84. K. E. Cano, M. J. Thrippleton, J. Keeler, A. J. Shaka, *J. Magn. Reson.* **167**, 291–297 (2004).
85. M. J. Thrippleton, J. Keeler, *Angew. Chem. Int. Ed.* **42**, 3938–3941 (2003).
86. H. Wang, G. D. Glick, E. R. P. Zuiderweg, *J. Magn. Reson., Ser. A* **102**, 116–121 (1993).
87. G. Bodenhausen, H. Kogler, R. R. Ernst, *J. Magn. Reson.* **58**, 370–388 (1984).
88. W. Denk, R. Baumann, G. Wagner, *J. Magn. Reson.* **67**, 386–390 (1986).
89. G. H. Weiss, J. E. Kiefer, J. A. Ferretti, *J. Magn. Reson.* **97**, 227–234 (1992).
90. V. Stoven, A. Mikou, D. Piveteau, E. Guittet, J.-Y. Lallemand, *J. Magn. Reson.* **82**, 163–168 (1989).
91. J. Fejzo, Z. Zolnai, S. Macura, J. L. Markley, *J. Magn. Reson.* **88**, 93–110 (1990).
92. P. Plateau, M. Guéron, *J. Am. Chem. Soc.* **104**, 7310–7311 (1982).
93. G. Otting, K. Wüthrich, *J. Am. Chem. Soc.* **111**, 1871–1875 (1989).
94. V. Sklenář, A. Bax, *J. Mag. Reson.* **75**, 378–383 (1987).
95. J. Stonehouse, G. L. Shaw, J. Keeler, *J. Biomol. NMR* **4**, 799–805 (1994).
96. A. A. Bothner-By, R. L. Stephens, J.-M. Lee, C. D. Warren, R. W. Jeanloz, *J. Am. Chem. Soc.* **106**, 811–813 (1984).
97. A. Bax, D. G. Davis, *J. Magn. Reson.* **63**, 207–213 (1985).
98. C. Griesinger, R. R. Ernst, *J. Magn. Reson.* **75**, 261–271 (1987).
99. D. Neuhaus, J. Keeler, *J. Magn. Reson.* **68**, 568–574 (1986).
100. T.-L. Hwang, A. J. Shaka, *J. Magn. Reson.* **135**, 280–287 (1998).
101. J. Schleucher, J. Quant, S. J. Glaser, C. Griesinger, in "Encyclopedia of Nuclear Magnetic Resonance" (D. M. Grant, R. K. Harris, eds.), vol. 8, pp. 4789–4804. John Wiley & Sons, Ltd., Chichester, 1996.
102. G. Wagner, W. Braun, T. F. Havel, T. Schaumann, N. Go, K. Wüthrich, *J. Mol. Biol.* **196**, 611–639 (1987).
103. P. Güntert, W. Braun, M. Billeter, K. Wüthrich, *J. Am. Chem. Soc.* **111**, 3997–4004 (1989).
104. H. Oschkinat, C. Grieinger, P. J. Kraulis, O. W. Sørensen, R. R. Ernst, A. M. Gronenborn, G. M. Clore, *Nature* **332**, 374–376 (1988).
105. C. Griesinger, O. W. Sørensen, R. R. Ernst, *J. Magn. Reson.* **73**, 574–579 (1987).
106. C. Griesinger, O. W. Sørensen, R. R. Ernst, *J. Am. Chem. Soc.* **109**, 7227–7228 (1987).
107. H. Oschkinat, C. Ciesler, T. A. Holak, G. M. Clore, A. M. Gronenborn, *J. Magn. Reson.* **83**, 450–472 (1989).
108. G. W. Vuister, R. Boelens, R. Kaptein, *J. Magn. Reson.* **80**, 176–185 (1988).
109. G. W. Vuister, R. Boelens, A. Padilla, G. J. Kleywegt, R. Kaptein, *Biochemistry* **29**, 1829–1839 (1990).

110. H. Oschkinat, C. Cieslar, A. M. Gronenborn, G. M. Clore, *J. Magn. Reson.* **81**, 212–216 (1989).
111. J. P. Simorre, D. Marion, *J. Magn. Reson.* **94**, 426–432 (1991).
112. R. Boelens, G. W. Vuister, T. M. G. Koning, R. Kaptein, *J. Am. Chem. Soc.* **111**, 8525–8526 (1989).
113. G. W. Vuister, R. Boelens, A. Padilla, R. Kaptein, *J. Biomol. NMR* **1**, 421–438 (1991).
114. R. Bernstein, A. Ross, C. Cieslar, T. A. Holak, *J. Magn. Reson., Ser. B* **101**, 185–188 (1993).
115. C. Cieslar, T. A. Holak, H. Oschkinat, *J. Magn. Reson.* **89**, 184–190 (1990).